NON-LINEAR DRYING DIFFUSION AND VISCOELASTIC DRYING SHRINKAGE MODELING IN HARDENED CEMENT PASTES

A Thesis

by

CHIN KONG LEUNG

Submitted to the Office of Graduate Studies of
Texas A&M University
in partial fulfillment of the requirements for the degree of

MASTER OF SCIENCE

May 2009

Major Subject: Civil Engineering

NON-LINEAR DRYING DIFFUSION AND VISCOELASTIC DRYING SHRINKAGE MODELING IN HARDENED CEMENT PASTES

A Thesis

by

CHIN KONG LEUNG

Submitted to the Office of Graduate Studies of
Texas A&M University
in partial fulfillment of the requirements for the degree of

MASTER OF SCIENCE

Approved by:

Chair of Committee,	Zachary Grasley
Committee Members,	Anastasia Muliana
	Eyad Masad
Head of Department,	David Rosowsky

May 2009

Major Subject: Civil Engineering

ABSTRACT

Non-Linear Drying Diffusion and Viscoelastic Drying Shrinkage Modeling in Hardened Cement Pastes. (May 2009)

Chin Kong Leung, B.S., California State University, Chico

Chair of Advisory Committee: Dr. Zachary Grasley

The present research seeks to study the decrease in diffusivity rate as relative humidity (RH) decreases and modeling drying shrinkage of hardened cement paste as a poroviscoelastic respose. Thin cement paste strips of 0.4 and 0.5 w/c at age 3 and 7 days were measured for mass loss and shrinkage at small RH steps in an environmental chamber at constant temperature. Non-linear drying diffusion rate of hardened cement was modeled with the use of Fick's second law of diffusion by assuming linearity of diffusion rate over short drops of ambient relative humidity. Techniques to determine drying isotherms prior to full equilibration of mass loss, as well as converting mass loss into concentration of water vapor were developed. Using the measured water vapor diffusivity, drying shrinkage strain was modeled by the theory of poroviscoelasticity. This approach was validated by determining viscoelastic properties from uniaxial creep tests considering the effect of aging by the solidification theory.

A change in drying diffusion rate at different RH was observed in the 0.4 and 0.5 w/c pastes at different ages. Drying diffusion rate decreases as RH drops. This can be attributed to a change in diffusion mechanisms in the porous media at smaller pore

radius. Shrinkage modeling with an average diffusion coefficient and with determined viscoelastic parameters from creep tests agreed well compared to the shrinkage data from experiments, indicating that drying shrinkage of cement paste may be considered as a poroviscoelastic reponse.

To my parents

ACKNOWLEDGEMENTS

I would like to thank my committee chair, Dr. Grasley, for his guidance, advice and support throughout this research, as well as Lee Gustavus, Rick Canetella, and Jeff Perry of McNew Laboratory with specimen preparation and testing. I would also like to thank Mercedes Cardenes, an undergraduate student worker, for providing assistance conducting the experimental program. My gratitude also goes to my office mates, who have provided valuable insights and suggestions for this research, and friends and relatives for their moral support and encouragement throughout my time spent at Texas A&M University.

TABLE OF CONTENTS

Page

ABSTRACT iii

ACKNOWLEDGEMENTS vi

TABLE OF CONTENTS vii

LIST OF FIGURES ix

LIST OF TABLES xiv

1. INTRODUCTION 1

1.1. Motivation 1
1.2. Objectives 1

2. PREVIOUS WORK 3

2.1. Non-linear Drying Diffusion 3
2.2. Shrinkage Mechanisms 5
2.3. Shrinkage Prediction 7
2.4. Limitations in Current Modeling and Measurements 10

3. EXPERIMENTAL 11

3.1. Mass Loss and Shrinkage Tests 11
3.1.1. Mass Loss Rate Measurements 12
3.1.2. Shrinkage Measurements 13
3.1.3. Specimens 15
3.1.4. Porosity 15
3.1.5. Data Acquisition 16
3.2. Elastic and Creep Test 16
3.2.1. Testing Environment and Apparatus 16
3.2.2. Specimens 18
3.2.3. Data Acquisition 19

4. MODELING TECHNIQUES 20

4.1. Drying Diffusion 20
4.1.1. Non-Linear Diffusion Modeling by Small Change in RH 22

Page

4.1.2. Sensitivity of Summation Terms 27
4.1.3. Determining Parameters Needed for Diffusion Modeling 28
4.2. Drying Shrinkage 30
4.2.1. Constant Diffusion Coefficient Approximation 32
4.2.2. Pore Stress Approximation 33
4.2.3. Saturation Factor Approximation 35
4.2.4. Viscoelastic Strain from RH History 37
4.2.5. Validation of Shrinkage Model 38
4.2.6. Viscoelastic Compliance from Experimental Data 38
4.2.7. Obtaining Elastic Moduli and Viscoelastic Parameters 39

5. RESULTS AND DISCUSSION 41

5.1. Porosity 41
5.2. RH(S) Approximation 41
5.3. Desorption Isotherm in Different Cement Pastes 44
5.4. Diffusion Rates in HCP 45
5.5. Shrinkage Modeling 49
5.5.1. Testing Results from Creep Tests 49
5.5.2. Obtaining Estimated Aging Function from Elastic Moduli 50
5.5.3. Viscoelastic Parameters 52
5.6. Modeling of Thin Cement Paste Strip 54

6. SUMMARY AND CONCLUSIONS 61

6.1. Conclusion 61
6.2. Future Work 62

REFERENCES 63

APPENDIX A 67

APPENDIX B 99

VITA 101

LIST OF FIGURES

FIGURE		Page
1	Mass loss measurement setup illustration	13
2	LVDT measurement setup	14
3	Creep frame apparatus	17
4	Cement paste cylinder	18
5	Diffusion solution flowchart	21
6	Solution sensitivity to number of terms in the summation of Eq. (28)	27
7	Changes in concentration (boundary condition) as a function of time	33
8	Pore stress approximation plot	35
9	Saturation factor approximation, 0.5 w/c 7 day	36
10	Sigmodial curve fit for *RH(S)*, 0.4 w/c 3 day	42
11	Sigmodial curve fit for *RH(S)*, 0.4 w/c 7 day	42
12	Sigmodial curve fit for *RH(S)*, 0.5 w/c 3 day	43
13	Sigmodial curve fit for *RH(S)*, 0.5 w/c 7day	43
14	Desorption isotherms of different w/c and age	44
15	Illustration on the effect of non-linearity of the isotherm on predicted concentration	46
16	Diffusion coefficient of different w/c and age	47
17	RH of cement paste strip as a function of time and spatial coordinate x	48
18	Viscoelastic compliance curve as a function of w/c and age	50
19	Elastic moduli as a function of age	51

FIGURE Page

20 Aging function v(t) plotted vs. time 52

21 Fitting of total viscoelastic creep compliance curves..... 54

22 Shrinkage model vs. measured data, 0.4 w/c, age: 3 day specimen 1..... 55

23 Shrinkage model vs. measured data, 0.4 w/c, age: 3 day specimen 2..... 56

24 Shrinkage model vs. measured, 0.5 w/c, age: 3 day, specimen 1..... 56

25 Shrinkage model vs. measured, 0.5 w/c, age: 3 day, specimen 2..... 57

26 Shrinkage model vs. measured, 0.5 w/c, age: 7 day, specimen 1..... 57

27 Shrinkage model vs. measured, 0.5 w/c, age: 7 day, specimen 2..... 58

28 Illustration of shifting shrinkage curve due to stress approximation error ... 59

29 Fitting for diffusion coefficient, 35-25% RH 0.4 w/c 3 day specimen 1 67

30 Fitting for diffusion coefficient, 45-35% RH 0.4 w/c 3 day specimen 1 68

31 Fitting for diffusion coefficient, 55-45% RH 0.4 w/c 3 day specimen 1 68

32 Fitting for diffusion coefficient, 65-55% RH 0.4 w/c 3 day specimen 1 69

33 Fitting for diffusion coefficient, 75-65% RH 0.4 w/c 3 day specimen 1 69

34 Fitting for diffusion coefficient, 85-75% RH 0.4 w/c 3 day specimen 1 70

35 Fitting for diffusion coefficient, 95-85% RH 0.4 w/c 3 day specimen 1 70

36 Fitting for diffusion coefficient, 35-25% RH 0.4 w/c 3 day specimen 2 71

37 Fitting for diffusion coefficient, 45-35% RH 0.4 w/c 3 day specimen 2 71

38 Fitting for diffusion coefficient, 55-45% RH 0.4 w/c 3 day specimen 2 72

39 Fitting for diffusion coefficient, 65-55% RH 0.4 w/c 3 day specimen 2 72

40 Fitting for diffusion coefficient, 75-65% RH 0.4 w/c 3 day specimen 2 73

FIGURE Page

41 Fitting for diffusion coefficient, 85-75% RH 0.4 w/c 3 day specimen 2 73

42 Fitting for diffusion coefficient, 95-85% RH 0.4 w/c 3 day specimen 2 74

43 Fitting for diffusion coefficient, 35-25% RH 0.4 w/c 7 day specimen 1 74

44 Fitting for diffusion coefficient, 45-35% RH 0.4 w/c 7 day specimen 1 75

45 Fitting for diffusion coefficient, 55-45% RH 0.4 w/c 7 day specimen 1 76

46 Fitting for diffusion coefficient, 65-55% RH 0.4 w/c 7 day specimen 1 77

47 Fitting for diffusion coefficient, 75-65% RH 0.4 w/c 7 day specimen 1 78

48 Fitting for diffusion coefficient, 85-75% RH 0.4 w/c 7 day specimen 1 79

49 Fitting for diffusion coefficient, 95-85% RH 0.4 w/c 7 day specimen 1 80

50 Fitting for diffusion coefficient, 35-25% RH 0.4 w/c 7 day specimen 2 80

51 Fitting for diffusion coefficient, 45-35% RH 0.4 w/c 7 day specimen 2 81

52 Fitting for diffusion coefficient, 55-45% RH 0.4 w/c 7 day specimen 2 81

53 Fitting for diffusion coefficient, 65-55% RH 0.4 w/c 7 day specimen 2 82

54 Fitting for diffusion coefficient, 75-65% RH 0.4 w/c 7 day specimen 2 82

55 Fitting for diffusion coefficient, 85-75% RH 0.4 w/c 7 day specimen 2 83

56 Fitting for diffusion coefficient, 95-85% RH 0.4 w/c 7 day specimen 2 83

57 Fitting for diffusion coefficient, 35-25% RH 0.5 w/c 3 day specimen 1 84

58 Fitting for diffusion coefficient, 45-35% RH 0.5 w/c 3 day specimen 1 84

59 Fitting for diffusion coefficient, 55-45% RH 0.5 w/c 3 day specimen 1 85

60 Fitting for diffusion coefficient, 65-55% RH 0.5 w/c 3 day specimen 1 85

61 Fitting for diffusion coefficient, 75-65% RH 0.5 w/c 3 day specimen 1 86

FIGURE Page

62 Fitting for diffusion coefficient, 85-75% RH 0.5 w/c 3 day specimen 1 86

63 Fitting for diffusion coefficient, 95-85% RH 0.5 w/c 3 day specimen 1 87

64 Fitting for diffusion coefficient, 35-25% RH 0.5 w/c 3 day specimen 2 88

65 Fitting for diffusion coefficient, 45-35% RH 0.5 w/c 3 day specimen 2 88

66 Fitting for diffusion coefficient, 55-45% RH 0.5 w/c 3 day specimen 2 89

67 Fitting for diffusion coefficient, 65-55% RH 0.5 w/c 3 day specimen 2 89

68 Fitting for diffusion coefficient, 75-65% RH 0.5 w/c 3 day specimen 2 90

69 Fitting for diffusion coefficient, 85-75% RH 0.5 w/c 3 day specimen 2 90

70 Fitting for diffusion coefficient, 95-85% RH 0.5 w/c 3 day specimen 2 91

71 Fitting for diffusion coefficient, 35-25% RH 0.5 w/c 7 day specimen 1 91

72 Fitting for diffusion coefficient, 45-35% RH 0.5 w/c 7 day specimen 1 92

73 Fitting for diffusion coefficient, 55-45% RH 0.5 w/c 7 day specimen 1 92

74 Fitting for diffusion coefficient, 65-55% RH 0.5 w/c 7 day specimen 1 93

75 Fitting for diffusion coefficient, 75-65% RH 0.5 w/c 7 day specimen 1 93

76 Fitting for diffusion coefficient, 85-75% RH 0.5 w/c 7 day specimen 1 94

77 Fitting for diffusion coefficient, 95-85% RH 0.5 w/c 7 day specimen 1 94

78 Fitting for diffusion coefficient, 35-25% RH 0.5 w/c 7 day specimen 2 95

79 Fitting for diffusion coefficient, 45-35% RH 0.5 w/c 7 day specimen 2 95

80 Fitting for diffusion coefficient, 55-45% RH 0.5 w/c 7 day specimen 2 96

81 Fitting for diffusion coefficient, 65-55% RH 0.5 w/c 7 day specimen 2 96

82 Fitting for diffusion coefficient, 75-65% RH 0.5 w/c 7 day specimen 2 97

FIGURE Page

83 Fitting for diffusion coefficient, 85-75% RH 0.5 w/c 7 day specimen 2 97

84 Fitting for diffusion coefficient, 95-85% RH 0.5 w/c 7 day specimen 2 98

85 Creep test data for 0.4 w/c 3 day specimen 99

86 Creep test data for 0.4 w/c 7 day specimen 99

87 Creep test data for 0.5 w/c 3 day specimen 100

88 Creep test data for 0.5 w/c 7 day specimen 100

LIST OF TABLES

TABLE Page

1 Coefficient used for water vapor saturation pressure determination..... 30

2 Porosity measurements..... 41

3 Elastic moduli from uniaxial compression test 50

4 Aging parameters used in viscoelastic moduli determination..... 51

5 Determined viscoelastic moduli internal variables 53

1. INTRODUCTION

1.1. Motivation

Shrinkage of portland cement concrete is one of the factors that cause cracking in concrete structures. Due to differential shrinkage, stresses develop at the surface of concrete caused by a restraint from a higher than ambient relative humidity (RH) inside the concrete. By developing a method to analyze drying diffusion rate of water (hereinafter referred to as diffusion) by collecting mass loss data continuously at a controlled RH environment, shrinkage mechanisms can be studied by comparing rate of drying of specimens and differences in the desorption. The present research seeks to validate this approach by experimentally measuring mass loss of various hardened cement paste (HCP) materials. The decrease in drying diffusivity of water vapor through cement paste at lower RH has long been recognized and will be verified. Drying shrinkage as a poroviscoelastic response has been modeled using measured RH data, but not been performed by considering water vapor diffusivity of the cement paste.

1.2. Objectives

The objectives of this research are the following: To confirm that diffusion coefficient (drying rate) decreases as ambient RH is lowered, and to demonstrate that drying shrinkage may be modeled as a poroviscoelastic response by considering an average diffusion coefficient for a given material and prescribed boundary condition.

This thesis follows the style of Cement and Concrete Research.

Drying diffusion is modeled after a one-dimensional Fick's law of diffusion, assuming linearity over each of the small RH steps. Drying rate measured by drying diffusion coefficient can be obtained by fitting the model to the experimental data. Desorption isotherm can also be obtained from the mass loss data.

Using the results from the diffusion model, viscoelastic shrinkage can be modeled by creating a pore humidity history with an average drying diffusion coefficient. The shrinkage model will be verified by using viscoelastic creep parameters from creep tests of sealed specimens.

2. PREVIOUS WORK

2.1. Non-linear Drying Diffusion

Drying mechanisms in porous materials, particularly gels, were extensively studied by Scherer [1]. After an initial period of constant rate of mass loss of free water evaporating from the surface, meniscus retreats into the pores and moisture is transported onto the surface by flow and evaporated on the surface, in addition to diffusion from the vapor phase. This is referred to by Scherer as the first falling rate period (FRP1). As water is dried from the pores, the flux of water to the surface also decreases as capillary pressure gradient is low near the surface. When evaporation inside the body is controlled by diffusion of vapor, it is called the second falling rate period (FRP2). As a porous material, concrete has long been recognized to have a non-linear drying rate at different RH. Bazant et al. [2] used non-linear diffusion theory to obtain drying diffusion coefficients through different geometries, including slab, cylindrical and spheres, by considering the pore humidity and water content's effect on drying diffusion by the finite difference method, and fitted data with the non-linear diffusion coefficient. The decrease in diffusion coefficient is noted as pore humidity drops, and the diffusion coefficient ceases to decrease at lower humidity. Bazant et al. [3] has studied cracking and microcracking's effect on diffusivity of moisture through cement paste and concluded that small, thin specimens, combined with gradual decrease in RH will prevent cracking, and the effect of microcracking on diffusion is substantial.

Diffusion of water vapor has been studied both experimentally and modeled numerically. The drying rate in cement-based materials is generally modeled after the diffusion theory based on Fick's Law of diffusion [2, 4-6]. Bazant et al. [4] proposed that for water diffusion in nonsaturated concrete, the diffusion is sufficiently slow that phases of water in the pore structure remain in thermal equilibrium. The diffusion rate as a function of the pore RH, temperature and self-desiccation is expressed as:

$$\frac{\partial \varphi}{\partial t} = \mathrm{div}(C \,\mathrm{grad}\, \varphi) + \frac{\partial \varphi_s}{\partial t} + K_T \frac{\partial T}{\partial t} \tag{1}$$

where φ is the pore RH, $\frac{\partial \varphi_s}{\partial t}$ is the self-desiccation, $K_T \frac{\partial T}{\partial t}$ represents the change in RH due to temperature and C is the diffusion coefficient. For constant temperature and negligible aging of the cement paste, both $\frac{\partial \varphi_s}{\partial t}$ and $K_T \frac{\partial T}{\partial t}$ can be eliminated from the equation. However, assuming a constant desorption isotherm for cement paste, which is a function of water/cement (w/c) ratio, age, and pore size distribution, is not an accurate treatment. Xi et al. [5, 6] presented a method in which the isotherm of the cement paste is taken into account when analyzing diffusion. An empirical equation of the diffusion coefficient proposed is

$$D = \alpha_{\mathrm{h}} + \beta_{\mathrm{h}}[1\text{-}2^{-10^{\gamma_h (H-1)}}] \tag{2}$$

where D is the diffusion coefficient, H is the RH, α_h, β_h, and γ_h are fitting parameters. Three diffusion mechanisms, ordinary diffusion, Knudsen diffusion and surface diffusion were taken into account in the empirical formula. The model presented was

able to fit experimental data well. The approach, however, requires calibration from experimental data, meaning that diffusion coefficients are not obtained directly and also the isotherm is determined by a model.

Diffusion of ions can be affected by change in cement chemistry from external environments. Carbonation, as shown by the work of Sarott et al. [5], affects diffusion rates of radioactive ions through HCP discs of high w/c ratios. It was found that carbonation of the HCP discs significantly lowers the diffusion coefficient of the radioactive substances tested.

2.2. Shrinkage Mechanisms

The primary mechanism of shrinkage of HCP is due to moisture transport. Moisture transport mechanisms include: capillary stresses at higher RH levels due to the stress induced by a meniscus in the pores, disjoining pressure, and surface energy [6-9]. The effect on shrinkage from each of the aforementioned mechanisms depends on pore RH, with solid surface energy dominating the shrinkage behavior at lower RH levels, since capillaries cannot exist at low RH due to high capillary stresses [10]. Capillary stresses controlling shrinkage at RH > 50% [7, 9, 11].

Ferraris and Wittmann [12] have investigated shrinkage on thin-walled cement tubes by adsorption from low RH (less than 40%) at different temperature and found that an equation by Bangham describes shrinkage well at low RH. The equation is

$$\frac{\Delta l}{l} = \lambda \Delta \gamma \,, \tag{3}$$

where $\Delta\gamma$ is the change in surface energy given by Gibb's equation, $\lambda = \frac{OP}{3E}$, O is the specific surface of the material, P is the specific weight of the nonporous material, and E is the Young's modulus of the material. This equation indicates that solid surface energy controls shrinkage at low RH.

Beltzung and Wittmann [13] have studied the combined effect of disjoining pressure and capillary suction in shrinkage of cement pastes by measuring disjoining pressure of a few layers of adsorbed layers of water between two quartz spheres. At lower radii of curvatures, accounting for the difference in surface tension due to adsorbed layers of water in the nanoscale lowers the capillary pressure significantly below 2 nm. The Kelvin equation relates equilibrium liquid and air in porous materials [14]. Simulation of gas adsorption on a wedge forming menisci with molecular modeling has been done by Wahab et al. [15], validating the Kelvin-Laplace equation.

Ayano and Wittmann [16] have studied drying diffusion and shrinkage of thin specimens bunched together by measuring mass and weight loss and using finite element analysis to determine diffusion coefficient without having to obtain a desorption isotherm. Small strips that were bunched up and sealed so that only one side is exposed to drying. Specimens were weighed and length change measured in the course of the experimental program. The presence of a small gap between specimens has been shown to not affect diffusion by a significant amount.

2.3. Shrinkage Prediction

Empirical modeling efforts in determining concrete structural element shrinkage have been done extensively. The B3 model by Bazant et al. [17], CEB-FIP 1990 [18], ACI-209R-82 [19] are some of the models proposed. Empirical models were developed by using databases of in service concrete data in order to try to determine relationships between shrinkage and each of the relevant parameters, such as compressive strength, moisture condition, size, etc. A model describing ultimate shrinkage was derived by Hansen [20] by considering mortar as a two phase material with the theory of elasticity with good agreements for various w/c ratios tested by another study, except for 0.35 w/c. However, the model does not account for viscoelastic effects and time.

Poroelasticity has been widely used in the fields of petroleum and geotechnical engineering to model coupled behavior of fluid and the porous media within porous rocks in various saturation conditions. The theory is first proposed by Biot [21] as a more general theory compared to the principle of effective stress by Terzaghi [22]. The constitutive equation for an isotropic poroelastic solid [23-25] is

$$\varepsilon_{ij} = \frac{1}{2G}\left(\sigma_{ij} - \frac{\nu}{1+\nu}\delta_{ij}\sigma_{kk}\right) - \frac{\alpha}{3K}p\delta_{ij}, \tag{4}$$

where ε_{ij} is the stress tensor, σ_{ij} is the stress tensor, δ_{ij} is the kronecker delta, G is the shear modulus of the solid, K is the bulk modulus of the solid, p is the pore fluid pressure, ν is the poisson's ratio and α is the Biot-Willis effective stress coefficient given by $1-\frac{K_p}{K_s}$. Neglecting temperature changes and for a body without externally

applied stress, Bentz et al. [26, 27] modeled the axial drying shrinkage of partially saturated porous Vycor® 7930 glass rods by the use of a modified version of the Biot's elastic constitutive equation

$$\varepsilon = \frac{Sp_{cap}}{3}\left(\frac{1}{K} - \frac{1}{K_s}\right), \tag{5}$$

where S is the saturation factor that accounts for the non-saturated state of the porous body, p_{cap} is the pore pressure of the pore fluid, K is the bulk modulus of the porous solid and K_s is the bulk modulus of the solid phase. Porous Vycor glass is considered as elastic in this model.

For materials such as HCP, viscoelasticity must be accounted for. To analytically account for viscoelasticity, Read [28] developed the correspondence principle. For porous solids, the correspondence principle has been used to account for viscoelasticity of the porous solid. Grasley [29] modeled autogeneous shrinkage accounting for viscoelastic properties for autogeneous shrinkage by applying the correspondence principle to Eq. (5). Results of leaving S in the time domain instead of transforming $S\sigma$ yielded a small difference for the range of RH analyzed. The method involved measuring RH directly with instruments embedded in the specimen.

Drying shrinkage is different than autogeneous shrinkage due to the internal RH being controlled by the ambient RH. Fu et al. [30] examined eigenstresses due to thermal drying of cement pastes and different drying rates at different temperatures. A theoretical model of drying shrinkage, drying creep and drying mass in HCP was proposed by

Benboudjema et al. [31] for 50-100% RH. Using strain induced by the pore fluid pressure, the following constitutive equation was used in the modeling of shrinkage:

$$\boldsymbol{\sigma} = (1-\phi)\tilde{\boldsymbol{\sigma}} - \phi p_s \mathbf{1} \tag{6}$$

where $\boldsymbol{\sigma}$ is the apparent stress tensor, ϕ is the porosity, $\tilde{\boldsymbol{\sigma}}$ is the effective stress tensor, p_s is the pore pressure and $\mathbf{1}$ is the second order unit tensor. The effective stress tensor is given by

$$\tilde{\boldsymbol{\sigma}} = \mathbf{E_s}(\varepsilon - \varepsilon^{bc}) \tag{7}$$

where $\mathbf{E_s}$ is the stiffness tensor of the solid skeleton, ε the strain tensor and ε^{bc} is the basic creep tensor. Applying the Boltzmann superposition principle and noting that the apparent stress equals to zero for a free drying shrinkage condition with no externally applied loads, Eq. (6) and Eq. (7) can be rewritten as

$$\mathbf{E} = (1-\phi)\mathbf{E}_s, \tag{8}$$

and

$$\varepsilon^{ds} = \phi[\mathbf{E}^{-1} p_s + \int_0^t \mathbf{J}^{bc}(t-\tau) d(h p_s)], \tag{9}$$

where $\mathbf{J}^{bc}$ is the creep compliance tensor. $\mathbf{J}^{bc}$ is calculated using a model that separates the creep driving mechanism from two scales differing in size of the porosity. The model is used in CAST3M, a finite element software for modeling cementitious materials. Modeling data was fitted to the experimental data obtained from Day et al. [32]. This method, however, requires substantial computing power.

2.4. Limitations in Current Modeling and Measurements

Empirical models can only be used to determine structural elements shrinkage. The present modeling approaches for shrinkage mostly involve in some sort of measurement or numerical analysis. Drying viscoelastic shrinkage modeling has not been carried out by considering an internal RH history obtained experimentally by considering the diffusion rate. Shrinkage can be estimated by the approach described herein with estimated diffusion coefficients and prescribed boundary RH for the geometry of interest.

This study will involve obtaining drying diffusion coefficient by directly fitting the diffusion equation based on Fick's second law of diffusion. This method does not require specialized finite element software and less computational power. By obtaining drying diffusion coefficients of cement pastes with small step changes in ambient RH, the non-linear diffusion coefficients can be obtained directly from experimental data. The decrease in diffusivity of water vapor in cement pastes can be examined by comparing diffusion coefficients at different RH levels. Drying shrinkage modeling by using drying diffusion coefficients require less computational power and does not require embedded sensors to monitor RH. The poroviscoelastic modeling approach can be verified by comparing to experimental data.

3. EXPERIMENTAL

The decrease/change in diffusion rate can be measured by mass loss of cement paste at different RH levels. Shrinkage of cement paste can be measured by length change in specimens subjected to changing external RH. In order to obtain mass loss data and shrinkage at different RH, a controlled test environment capable of changing RH and keeping temperature constant is required. Mass loss and shrinkage need to be measured in such environments for the duration of the test. The obtained data were analyzed and used to determine diffusion coefficient, diffusion coefficients were then used as input parameters for the shrinkage model. To verify the poroviscoelastic shrinkage model, creep compliance coefficients of the materials also needed to be obtained from separate creep tests of sealed specimens. This section details the methods used to acquire the required data.

3.1. Mass Loss and Shrinkage Tests

The equipment used to provide a testing environment with controlled temperature and RH for this study is a Cincinnati Sub-Zero temperature chamber model no. ZPH-8-1.5-H/AC with an 8 cu. ft volume. The chamber is capable of rapid change in RH and maintaining ±3% RH. Specimens and measuring scales were placed on a stainless steel rack near the middle of the chamber. Moisture in air is controlled by an evaporator and dehumidification coil, which the air passes through. Air is recirculated by a fan, supplying the specimens with consistent air flow at each of the different RH levels and minimizing RH differences due to the position of the strip within the chamber.

Since both diffusion and shrinkage might be affected by the presence of carbon dioxide in the ambient atmosphere due to carbonation measures to prevent carbonation shrinkage were employed. Reagent grade lithium hydroxide monohydrate crystals ($LiOH\text{-}H_2O$), manufactured by Sigma Aldrich were placed in glass petri dishes within the chamber in order to absorb carbon dioxide from the air in the chamber prior to the starting of the experiments. CO_2 reacts with $LiOH\text{-}H_2O$ and forms a carbonate, effectively removing the CO_2 from air. $LiOH\text{-}H_2O$ has been employed in environments where CO_2 removal is necessary [33, 34].

RH and temperature were measured continuously at set intervals by a solid state sensor mounted in the chamber. Temperature level was set at 23^oC throughout the testing program. The time for each step varied between 5-7 hours for desorption in order to shorten time required for each test. To minimize cracking on the surface of the strips, RH steps were in 10% increments, with the initial RH set at 95%, reaching a low of 25% at the end of the test. The testing began once the mass of the strips equilibrated at 95%. A typical test duration including all of the RH steps varied between specimens and ranged from 4-7 days.

3.1.1. Mass Loss Rate Measurements

The scales used were manufactured by Mettler-Toledo. Models PB303-FACT and PL80-3 were used in this study. Both scales have a 0.001 g sensitivity to ensure a sufficient resolution and the ability to measure small mass change. Specimens were attached to spring-loaded grips with hooks, and were hung below the scales for weighing. Figure 1 illustrates the setup of the scale in the chamber.

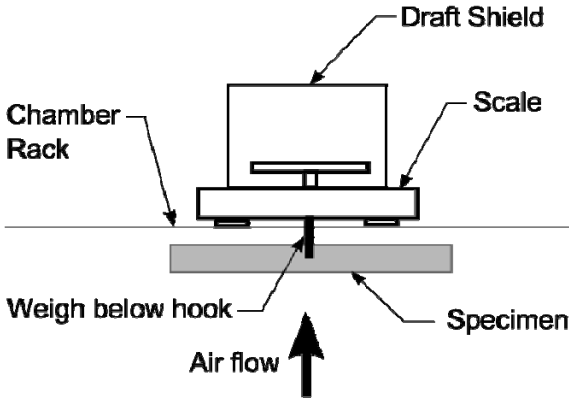

Figure 1: Mass loss measurement setup illustration

3.1.2. Shrinkage Measurements

To measure free shrinkage, simple frames were made by using a long threaded rod attached with aluminum pieces cut to the desired length. Pieces were secured onto the threaded rod by stainless steel nuts. Height was adjusted for different specimen dimensions by adjusting the position of the nuts on the threaded rod. Rubber pads were attached on the bottom to isolate vibration. For this research, Linear Variable Differential Transformers (LVDTs) manufactured by Macrosensors were used to measure length change due to free shrinkage from diffusion. The LVDT bracket was secured onto a piece of aluminum bent 90 degrees by two screws. An LVDT was mounted in the LVDT bracket. A paper clip was attached on one end of a piece of HCP strip. HCP Strip was then placed into the bracket. A brass screw with the LVDT core was placed onto the paper clip, in the channel of the LVDT and an adhesive was used to secure the screw onto the paper clip. Prior to starting of the test, the LVDT was adjusted so that when the cement paste shrinks, the LVDT core would stay in the measuring

range of the LVDT. Figure 2 illustrates the set up with a front and side view of the apparatus.

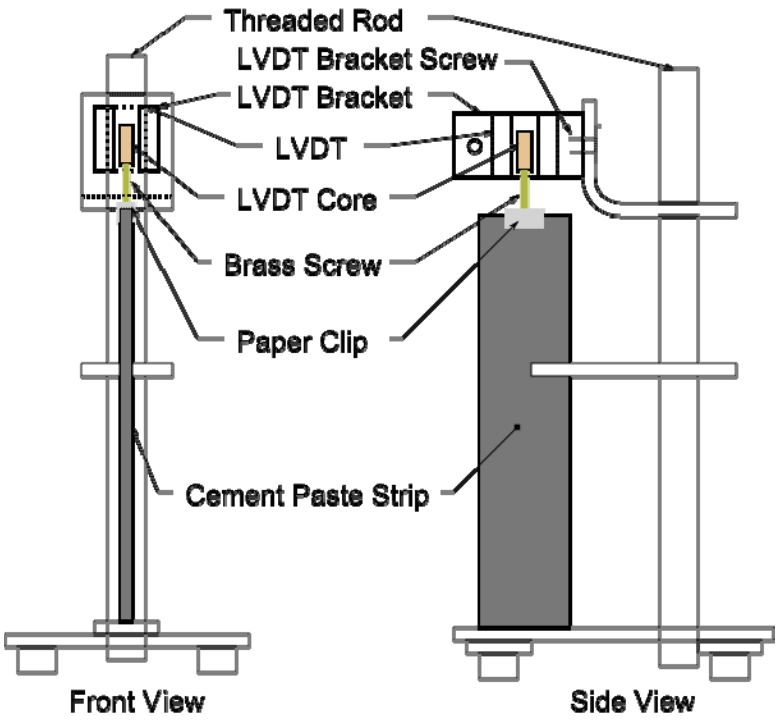

Figure 2: LVDT measurement setup

3.1.3. Specimens

HCP strips of two different w/c were cast in this study. The w/c used were 0.4 and 0.5. ASTM Type I cements were used for mixing. HCP strips aged 3 and 7 days were made for testing. HCP strips were made by casting fresh cement paste on an acrylic sheet and separated by 2mm thick acrylic strips. Fresh cement paste was mixed in accordance to ASTM C305-06 [35]. Fresh cement paste was placed on the sheet and the surface finished. The mold containing fresh cement paste with the finished surface was placed in a container filled with water for curing. HCP strips were demolded after 24 hours to ensure strength gain, and they were placed in a vacuum-sealed container filled with water. Strip dimensions varied slightly between specimens were approximately 45mm in width, 2mm in thickness and 200mm in length. Actual dimensions were measured by a precision caliper and recorded. Specimens were made thin in order to reduce time for equilibration of water mass loss.

After the testing is finished, the strips were tested for carbonation by spraying an alcohol solution with 2% Phenolphthalein, a pH indicator. Carbonation causes the pH of HCP to drop. A color change of the Phenolphthalein solution to pink indicates a pH of 12-14 (basic), whereas a clear color indicates a neutral pH.

3.1.4. Porosity

Porosity measurements were also made with the HCP strips. Strips were dried to saturated surface dry (SSD) condition and then weighed on a scale. Strips were then placed a drying oven at 110 C for 24 hours and reweighed.

3.1.5. Data Acquisition

The chamber was connected to a PC via a serial cable. RH and temperature levels were measured by probes connected to the controller within the chamber and recorded by CSZ-supplied software. To record the mass change from the scales, a LabView program was written to obtain mass data from the scales. The scales have serial RS303 ports and connected directly to a PC via serial cables. A National Instrument data logger model number SCC-68 is used for data acquisition for the shrinkage. LVDTs were connected to a separate signal conditioner, and the signal conditioner is connected to SCC-68. LVDTs were calibrated by adjusting voltage output on the signal conditioner with a LVDT calibration apparatus with a micrometer to note the actual displacement.

3.2. Elastic and Creep Test

3.2.1. Testing Environment and Apparatus

To prevent temperature effects, both the elastic and creep tests were done in facilities with air conditioning, maintaining a constant temperature. A creep frame was used to load multiple specimens in axial compression in order to measure creep strain. Procedures are described in ASTM C512 [36] with modifications detailed in this section. The creep frame was loaded by placing a hydraulic jack between the top loading plates. The top plate was secured by a top bolt during loading. As the hydraulic jack was raised, the spring between the bottom plates was compressed. After loading, the plate directly underneath the hydraulic jack was secured by a nut. This maintains the load by putting the threaded rods in tension. Specimens were loaded centrically by steel ball bearings on

the end caps. Hydraulic pressure was subsequently released after loading and the specimens were kept in compression by the steel rods. The test apparatus is illustrated in Figure 3.

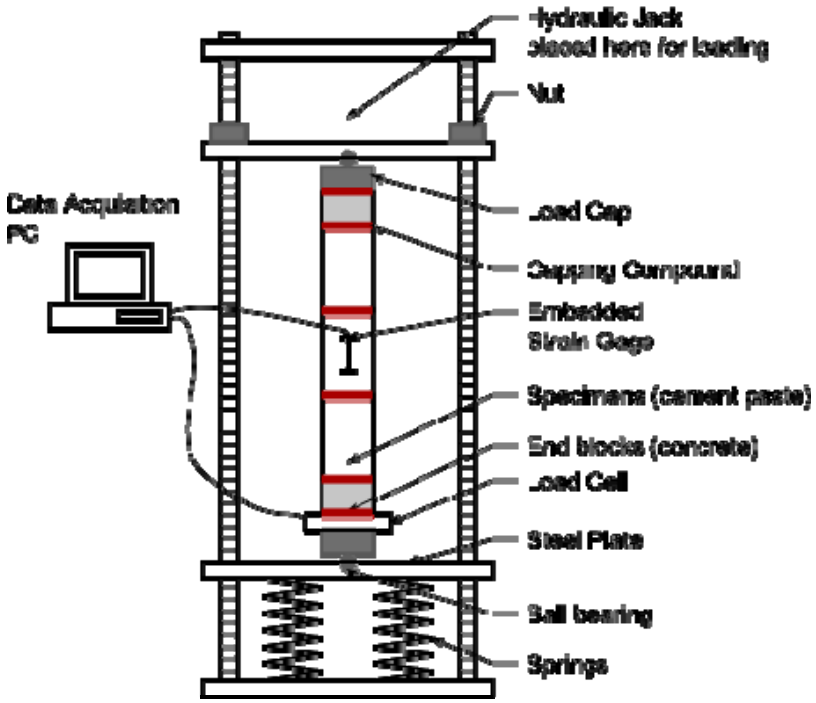

Figure 3: Creep frame apparatus

A load cell was placed on the bottom to record load loss during the creep test. As the specimens creep, applied load decreases due to the change of the compressed length of the springs. HCP exhibits significant creep compared to concrete specimens. By obtaining a load curve with respect to time instead of assuming a constant load, the viscoelastic compliance as a function of time was more accurate. To avoid damage from stress such as cracking, the uniaxial stresses applied to the specimens were between 2-3.5 MPa. Both elastic and viscoelastic moduli need to be obtained for modeling

purposes. Testing of the elastic moduli followed ASTM C469 [37], with minor modifications. Ultimate strength of the specimens were not performed to determine the stress for testing. Applied uniaxial stress was 2.5 MPa for all of the specimens tested.

3.2.2. Specimens

Test specimens for uniaxial compression tests (elastic moduli determination) were 101.6 mm diameter and 203.2 mm height, with two LVDT mounted on the side.

For the creep test, embedded strain gages manufactured by Tokyo Sokki Kenkyujo were used to collect deformation data. Strain gages were of a three-wire type, and were secured by fishing strings onto cylinder molds. Cement paste was placed into the cylinder mold after preparation. The cylinder's dimensions were 4" diameter and 8" height. Cement paste was mixed in accordance to ASTM C305-06 [35]. Cement paste cylinder was demolded after 24 hours and wrapped with aluminum foil backed adhesive tape to prevent drying, which would increase creep of concrete under load [38]. Figure 4 illustrates a cross section of the test specimen.

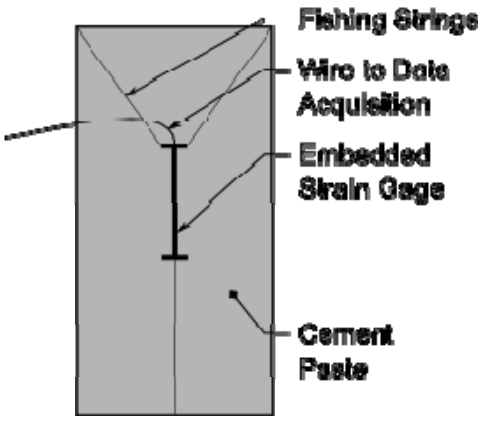

Figure 4: Cement paste cylinder

Sulfur based capping compound was placed on both end of the cylinder to ensure specimens will be loaded centrically. High strength capping compound in accordance with ASTM C-617 was used [39].

3.2.3. Data Acquisition

A National Instrument data logger model number SCC-68 was used for data acquisition. Strain gages were connected to SCC-SG 01 quarter bridge strain measurement modules, Each capable of connecting two strain gages. The load cells were manufactured by Honeywell Sensotec. Calibration factors were obtained and input into the data acquisition program from the manufacturer in order to ensure a correct load conversion factor for the voltage. A National Instrument LabView program was used to collect the data.

4. MODELING TECHNIQUES

4.1. Drying Diffusion

One-dimensional diffusion is assumed for modeling of a thin, wide strip. Several challenges, including the time required for equilibration of cement strip, require some modification to the classical diffusion equation solution for modeling. Figure 5 is a flowchart that describes the problem solving process. Due to time constraints, mass loss in the HCP strips would not be equilibrated at the end of each step. Mass at the end of each step was estimated by a fit. Desorption isotherms were fitted with a second degree polynomial function. Mass loss was then converted into concentration of water vapor by a function considering thermodynamics of vapor and liquid phase of water. The analysis included a method to account for the non-uniform initial moisture profile, caused by the non-equilibrated state at the end of each step. Linearity of the diffusion coefficient was assumed for each of the small step changes in RH.

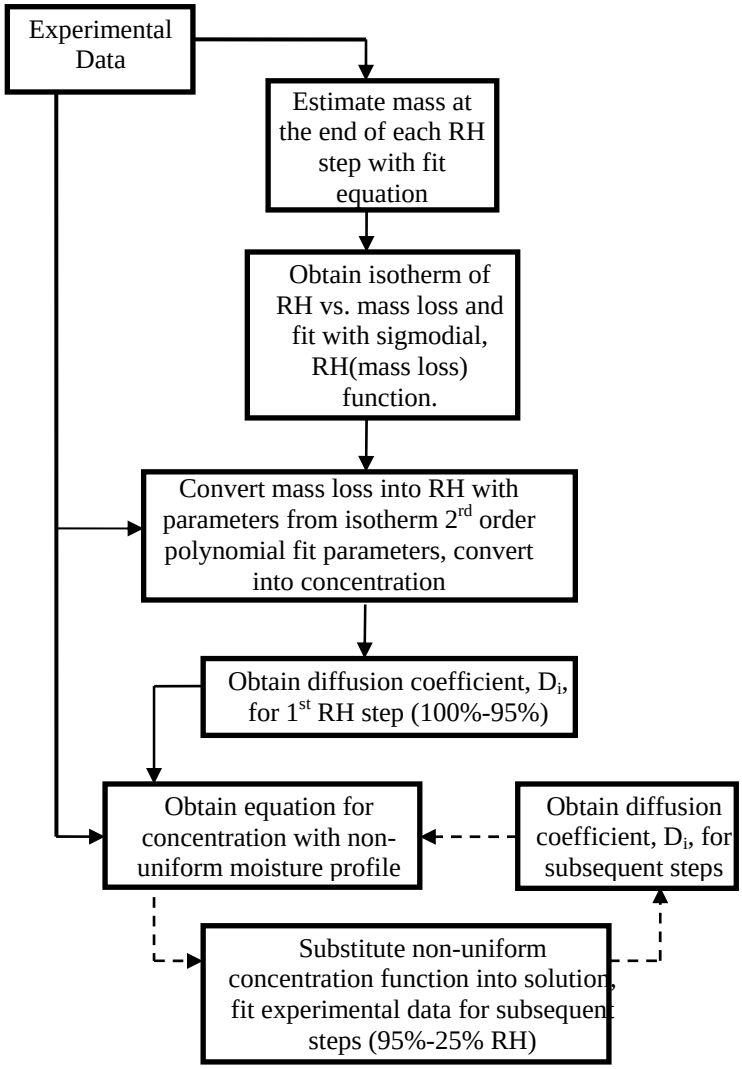

Figure 5: Diffusion solution flowchart

4.1.1. Non-Linear Diffusion Modeling by Small Change in RH

In order to utilize the solution to the heat equation for the determination of drying diffusion coefficient D of HCP, mass loss data was obtained from experiments and converted to water vapor concentration. Diffusion of water vapor in a thin HCP strip has the same form as the heat equation,

$$\frac{\partial \phi}{\partial t} = D\frac{\partial^2 \phi}{\partial x^2} \tag{10}$$

where ϕ is the mass vapor concentration, and D is the diffusion coefficient. Thickness of the strip is L. The boundary condition and initial condition are as follows:

$$\begin{aligned} &\phi(0,t) = \phi_{final} \\ &\phi(L,t) = \phi_{final} \\ &\phi(x,0) = \phi_{int} \end{aligned} \tag{11}$$

At $t = 0$, the concentration profile is uniform. $f(x) = \phi_{int} - \phi_{final}$ denotes the magnitude of the RH step change, which is a constant. Eq. (10) is solved accordingly:

$$\phi(x,t) = \frac{2}{L}\sum_{n=1}^{\infty} e^{-\frac{n^2\pi^2 Dt}{L^2}} \sin(\frac{n\pi x}{L})\int_0^L (\phi_{int} - \phi_{final}) \sin(\frac{n\pi s}{L})ds + \phi_{final} \tag{12}$$

Since $f(x) = (\phi_{int} - \phi_{final})$ is a constant, the integral $(\phi_{int} - \phi_{final})\int_0^L \sin(\frac{n\pi s}{L})ds$ can be evaluated. Eq. (12) is simplified as:

$$\phi(x,t) = 4(\phi_{int} - \phi_{final})\sum_{n=1}^{\infty} e^{-\frac{n^2\pi^2 Dt}{L^2}} \sin(\frac{n\pi x}{L}) + \phi_{final} \tag{13}$$

Mass loss data from the experiment was an average mass loss of the strips, independent of spatial coordinate x. Therefore, converted concentration data of the strips from the experiments was also only as a function of time. The average concentration across the thickness $\phi_{avg}(t)$ in the strip must be used instead of the concentration as a function of both time and position of the strip. This is done by integrating Eq. (13) with respect to x:

$$\begin{aligned} &\phi_{avg}(t) = \frac{1}{L}\int_0^L \phi(x,t)dx \text{ or} \\ &\phi_{avg}(t) = \frac{4(\phi_{int} - \phi_{final})}{L}\int_0^L \sum_{n=1}^{\infty} e^{-\frac{n^2\pi^2 Dt}{L^2}} \sin(\frac{n\pi x}{L})dx + \phi_{final} \end{aligned} \tag{14}$$

.

After converting mass loss data into concentration, ϕ_{int}, ϕ_{final} were determined by multiplying the boundary RH of each step by a factor to convert RH into concentration of water vapor in air. This procedure will be explained in Section 4.1.3. D can then be determined by fitting the converted experimental data with Eq. (14). The mass loss of a cementitious sample may be expressed as

$$\Delta M(t) = M(t) - M_0 \tag{15}$$

where $M(t)$ is the mass at time *t*, and M_0 is the initial mass of the saturated specimen. $M(t)$ may be determined according to

$$M(t) = M_v(t) + M_l(t) + M_{solid} \tag{16}$$

where M_v is the mass of the vapor, M_l is the mass of the liquid, and M_{solid} is the mass of the solid phase. Assuming constant porosity, the average degree of saturation, S_{avg}, may be determined as

$$S_{avg}(t) = \frac{V_l(t)}{V_p} = \frac{M_l(t)}{\rho_w V_p} \tag{17}$$

where ρ_w is the density of water, V_l is the volume of the liquid in the pores, and V_p is the total volume of pores in the specimen. Rearranging Eq. (17), we find that

$$M_l(t) = \rho_w S_{avg}(t) V_p . \tag{18}$$

The volume fraction of the pores that contain vapor is $(1 - S_{avg})$ such that M_v may be expressed as

$$M_v(t) = (1 - S_{avg}(t)) V_p \phi(t) \tag{19}$$

where ϕ is the concentration of the water vapor molecules in the vapor. Combining Eq. (16), (18), (19), and recognizing that $V_p = PV_T$ where P is the porosity and V_T is the specimen volume, we can write

$$M(t) = PV_T S_{avg}(t)\left(\frac{\phi(t)}{S_{avg}(t)} - \phi(t) + \rho_w\right) + M_{solid} . \tag{20}$$

Since M_0 is the mass at $M(t=0)$ and $S_{avg}(t=0) = 1$ we find that

$$M_0 = PV_T \rho_w + M_{solid} . \tag{21}$$

Combining (15), (20), and (21) we find that

$$\Delta M(t) = \left(1 - S_{avg}(t)\right) PV_T \left(\rho_w - \phi\right). \tag{22}$$

However, since $\rho_w \gg \phi$, we can closely approximate the mass loss in the specimen as

$$\Delta M(t) \approx \left(1 - S_{avg}(t)\right) PV_T \rho_w. \tag{23}$$

With knowledge of the desorption curve (i.e. $S_{avg}(t) = S_{avg}\left(RH_{avg}(t)\right)$), the mass change can be written in terms of the average RH, RH_{avg}, in the specimen cross section.

Due to time constraints, the RH step time length was generally insufficient for full equilibration in many of the steps. This causes the RH inside of the strip to be higher than at the surface (boundary). Modifying the solution in Eq. (14) would account for the non-uniform moisture profile in the initial condition, denoted as $\phi_{int@\%RH}(x)$.

$$\phi_{int@\%RH}(x) = A_1 + A_2 \sin(A_3 x + A_4) \tag{24}$$

where $A_1 + A_2 + A_3 + A_4$ are fitting parameters obtained by fitting Eq. (24) to the non-uniform moisture profile at time *t*, before the next RH step occurs in Eq. (14). $\phi_{int@\&RH}(x)$ is a function of the spatial coordinate x only. The boundary condition and initial conditions become

$$\begin{aligned} &\phi(0,t) = \phi_{final} \\ &\phi(L,t) = \phi_{final} \\ &\phi(x,0) = \phi_{int@\%RH}(x) + (\phi_{int} - \phi_{final}) \end{aligned} \tag{25}$$

where ϕ_{int} and ϕ_{final} are the boundary concentrations at the beginning of each of the steps.

Since ϕ_{int} was obtained from the concentration data converted from the original mass loss data, the value must be adjusted by adding $\phi_{int@\%RH}(x)$, from Eq. (24) of the previous RH step to obtain the new boundary condition. Otherwise, the curve fit would overestimate the initial concentration. Eq. (13) becomes

$$\phi(x,t) = \frac{2}{L}\sum_{n=1}^{\infty} e^{-\frac{n^2\pi^2 Dt}{L^2}} \sin(\frac{n\pi x}{L}) \int_0^L (\phi_{int@\%RH}(s) + (\phi_{int} - \phi_{final})) \sin\frac{n\pi s}{L} ds + \phi_{final} \tag{26}$$

or

$$\begin{aligned} \phi(x,t) &= \frac{2}{L}\sum_{n=1}^{\infty} e^{-\frac{n^2\pi^2 Dt}{L^2}} \sin(\frac{n\pi x}{L}) \int_0^L \phi_{int@\%RH}(s) \sin\frac{n\pi s}{L} ds \\ &+ \frac{4(\phi_{int} - \frac{1}{L}\int_0^L \phi_{int@\%RH}(x)dx - \phi_{final})}{L} \sum_{n=1}^{\infty} e^{-\frac{n^2\pi^2 Dt}{L^2}} \sin(\frac{n\pi x}{L}) + \phi_{final} \end{aligned} \tag{27}$$

Using the same technique of integration of Eq. (27) shown in Eq. (14), the average concentration can be obtained as,

$$\begin{aligned} \phi(t) &= \frac{2}{L^2}\int_0^L \left(\sum_{n=1}^{\infty} e^{-\frac{n^2\pi^2 Dt}{L^2}} \sin(\frac{n\pi x}{L}) \int_0^L \phi_{int@\%RH}(s) \sin\frac{n\pi s}{L} ds \right) dx \\ &+ \frac{4(\phi_{int} - \frac{1}{L}\int_0^L \phi_{int@\%RH}(x)dx - \phi_{final})}{L} \int_0^L \sum_{n=1}^{\infty} e^{-\frac{n^2\pi^2 Dt}{L^2}} \sin(\frac{n\pi x}{L}) dx + \phi_{final} \end{aligned} \tag{28}$$

.

The values of D for each of the subsequent steps were then determined by fitting Eq. (28) to the experimental data. Care must be taken to include the correct $\phi_{int@\%RH}(x)$ for fitting each of the steps, which is a function of the non uniform profiles, $\phi_{int@\%RH}(x)$ obtained from all of the previous steps.

4.1.2. Sensitivity of Summation Terms

To reduce computation time during the fitting of D, summation in the solution in Eq. (28) was carried to 50 terms. The sensitivity of the calculated diffusion coefficient to number of the terms in the summation is shown in Figure 6.

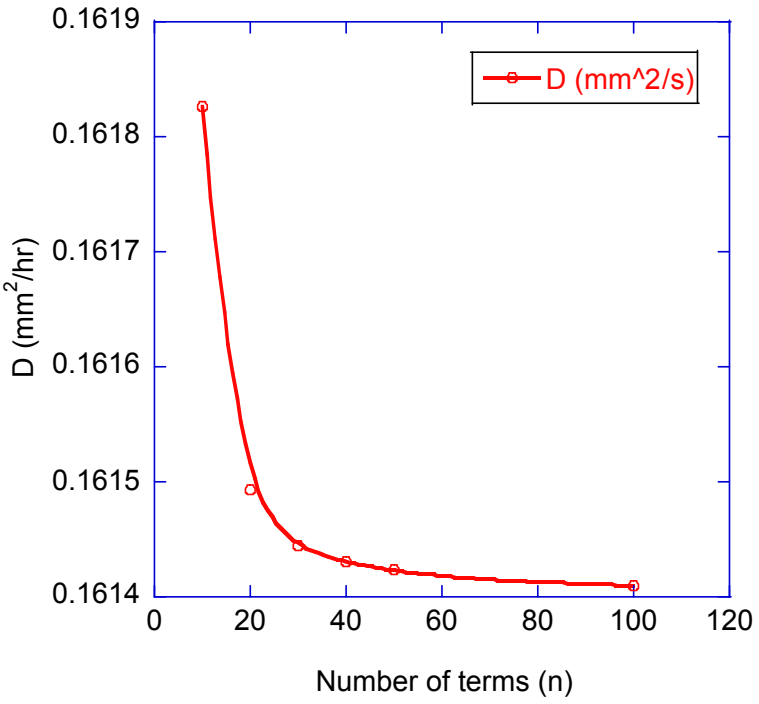

Figure 6: Solution sensitivity to number of terms in the summation of Eq. (28)

Figure 6 was obtained from diffusion coefficient determination at 95-85% RH step for a selected specimen. The difference in diffusion coefficient from 10 terms to 50 terms indicated a decrease of only 0.025%, and the solution converged as terms were increased. Difference between 100 and 50 terms was 0.008%. Using 50 terms in the summation was therefore considered adequate for an accurate diffusion coefficient determination.

4.1.3. Determining Parameters Needed for Diffusion Modeling

If insufficient time is given for the mass to reach equilibrium, the moisture profile within the thin HCP specimen considered would not be equilibrated. A final mass loss at infinite time must be determined for each RH step in order to construct an accurate desorption isotherm. The following fitting function was used to determine the final mass loss at each step by fitting the mass loss for each step:

$$M_{avg} = \left(C_1 e^{-a_1 t} + C_2 e^{-a_2 t} + C_3 e^{-a_3 t} + C_4 \right) \tag{29}$$

where M_{avg} is the average mass loss during testing in grams, C_i and a_i are the fitting parameters. M_{final} is estimated by calculating M_{avg} at $t = \infty$, which yields $M_{final} = C_1 + C_2 + C_3 + C_4$. Once the final mass equilibrated at each of the steps were obtained, an isotherm of $M_{avg}(RH)$ can be obtained by plotting equilibrated mass as a function of RH. The saturation S at each of the steps can be calculated by dividing M_{final} by the total amount of vapor and liquid water in the pore space

$$S = 1 - \frac{M_{avg}(RH)}{\mathrm{V}_{\mathrm{tot}} \phi \rho_w} \tag{30}$$

Where $\mathrm{V}_{\mathrm{tot}}$ is the total volume of the specimen, ϕ is the porosity of the specimen, and ρ_w is the density of water. By plotting an isotherm $RH(S)$, a sigmodial function was used to fit the isotherm according to

$$RH(S) = F_1 + \frac{F_2 - F_1}{1 + e^{\left(-\frac{(S - F_3)}{F_4}\right)}}, \tag{31}$$

where F_1, F_2, F_3, F_4 are fitting parameters.

Bazant et al. [4] proposed that for water diffusion in non-saturated concrete, the diffusion is sufficiently slow that for phases of water in the pore structure to remain in thermal equilibrium. The ideal gas equation can be utilized under this assumption:

$$PV = nRT, \tag{32}$$

where n is the number of moles, and can be rewritten as $\frac{m}{M}$. m is the mass and M is the molar mass of the ideal gas. R is the universal gas constant, T is temperature in Kelvin, P is the absolute pressure in kPa and V is the volume of the gas. By rearranging the terms, concentration $\phi = \left(\frac{m}{V}\right)$ of the water vapor in the pores can be rewritten as

$$\phi = RH(S)\frac{e_{H_2O} M}{RT} \tag{33}$$

Where e_{H_2O} is the saturation water vapor pressure. This is given by [40]:

$$e_{H_2O} = a_0 + T(a_1 + T(a_2 + T(a_3 + T(a_4 + T(a_5 + Ta_6))))) \quad (34)$$

Where T is the temperature in Celcius and the coefficients a_i are given in Table 1.

Table 1: Coefficient used for water vapor saturation pressure determination

Coefficient a_i	Value of a_i
a_0	6.108
a_1	4.437 E-1
a_2	1.429 E-2
a_3	2.651 E-4
a_4	3.031 E-6
a_5	2.034 E-8
a_6	6.136 E-11

The same procedure was repeated to convert the other boundary conditions (RH at each step) to concentration of water vapor in air.

4.2. Drying Shrinkage

Due to the viscoelastic nature of cement based materials, loading history greatly affects shrinkage. A change in RH induces pore stress on the pore structure, thereby causing shrinkage. By converting the concentration of water vapor in air back to RH as a

function of time and location x, RH history can be obtained for viscoelastic modeling. Diffusion from the HCP pore network into the ambient environment creates a negative pore stress in the pore fluid, thereby causing shrinkage. The shrinkage modeling was based on poroelasticity [27, 29] with slight modifications detailed in this section. Modifying Eq. (5) for a linear viscoelastic material yields

$$\varepsilon(x,t) = \int_0^t \frac{S(x,t)\partial P(x,t)}{3\partial t}\left(B(t-t') - \frac{1}{K_{solid}} \right) \tag{35}$$

where $\varepsilon(x,t)$ is the shrinkage of the strip as a function of time t and spatial coordinate x, $S(x,t)$ is the saturation factor, $P(x,t)$ is the pore pressure/stress, $B(t-t')$ is the viscoelastic bulk compliance and K_{solid} is the elastic bulk modulus of the cement paste. K_{solid} used in modeling is 40 GPa [29, 41]. Applying Laplace transform to Eq. (35) yields

$$\bar{\varepsilon}(x,s) = \frac{S(x,t)\bar{P}(x,s)}{3}\left(\frac{1}{s\bar{K}(s)} - \frac{1}{K_{solid}} \right), \tag{36}$$

where $\bar{K}(s)$ is the viscoelastic bulk modulus in the transform domain. Several approximations were made in order to simplify the solution. Due to the complexity in obtaining the Laplace transform of SP multiplied together, S was left in the domain solution for the viscoelastic strain. The methods and approximations used in the determination of $S(x,t)$ and $\bar{P}(x,s)$ is outlined the following sections. Desorption isotherms with mass loss data was plotted against RH to obtain saturation factors as a function of RH. A second-order polynomial fit was used for the determination. $RH(x,t)$

was then used as an input into the approximate S function for $S(x,t)$. Values of S at larger RH were less accurate, but pore stress was also smaller at large S.

4.2.1. Constant Diffusion Coefficient Approximation

Due to the viscoelastic properties of cement paste, it is necessary to solve the problem in the transform domain. To solve the diffusion equation in the transform domain, a constant diffusion coefficient was used by calculating an average diffusion coefficient determined from Section 4.1.3. This allows for a quicker, more compact solution of concentration ϕ, and a simpler calculation of strain in transform domain $\bar{\varepsilon}(x,s)$. $\overline{RH}(x,s)$ can be determined by solving for the concentration in the transform domain according to

$$s\bar{\phi}(x,s) - \phi(x,0) = D\frac{\partial^2 \bar{\phi}}{\partial x^2}, \tag{37}$$

where $\bar{\phi}(x,s)$ is the concentration in transform domain. The boundary condition is a function of time, in piecewise functions

$$\begin{aligned} &\phi(0,t) = \phi(L,t) = \phi_{final1}(1 - H(t - t_1)) + \\ &\sum_{i=1}^{n} \phi_{final-i}(H(t - t_i) - H(t - t_{i+1})) \end{aligned} \tag{38}$$

where $H(t-t_i)$ is the Heaviside step function, t_i denotes the time at each step *i*, and $\phi_{final-i}$ denotes concentration at each step *i*. Concentration $\bar{\phi}(x,s)$ can be rewritten in

terms RH with Eq. (33). Figure 7 shows the boundary condition plotted as a function of time.

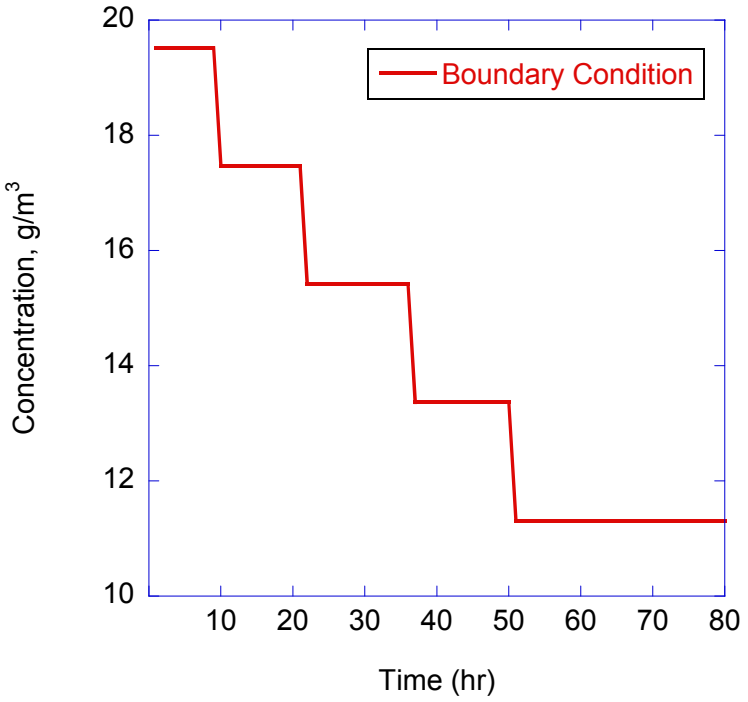

Figure 7: Changes in concentration (boundary condition) as a function of time

4.2.2. Pore Stress Approximation

Pore stress is given by the Kelvin-Laplace equation when shrinkage is dominated by capillary effects:

$$\sigma = -\frac{\ln(RH/100)RT}{V_m} \quad (39)$$

Here, σ is the pore stress, RH is the relative humidity, R is the ideal gas constant, T is the temperature in Kelvin, and V_m is the molar volume of water.

Since the solution Eq. (36) is in the transform domain, σ must be determined in the transform domain. However, Laplace transform cannot be applied directly for this form for the RH history considered. An approximate function was used instead, since the RH range was narrow and the error introduced would be minimal. A linear fit can be used to approximate σ as a function of RH.

$$\sigma = M_0 + M_1 RH \tag{40}$$

$$\bar{\sigma}(x,s) = \frac{M_0}{s} + M_1 \overline{RH}(x,s) \tag{41}$$

where M_0 and M_1 are fitting parameters. Eq. (40) can be easily transformed into Eq. (41).

$\overline{RH}(x,s)$ was determined from Eq. (39) by substituting concentration ϕ obtained from Section 4.2.1, and was substituted into Eq. (41). Results of the approximation are shown in Figure 8.

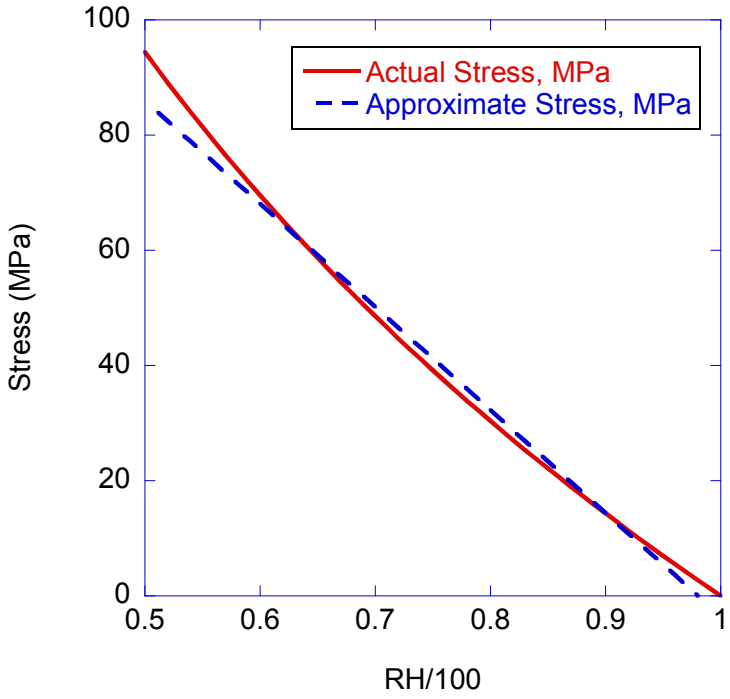

Figure 8: Pore stress approximation plot

Some error is introduced at the limits of the RH boundaries due to the non-linearity of the pore stress from Eq. (39). At regions near 100% RH, this approximation function actually predicts a positive stress developing in the pore space, which is clearly not in reality and not predicted by the Kelvin-Laplace equation (Eq.(39)). During the desorption process, negative pore stress exerted on the pore walls cause the specimen to shrink.

4.2.3. Saturation Factor Approximation

As water leaves the cement paste matrix due to a moisture gradient, the effective saturation also lowers. A desorption isotherm is constructed with the mass loss predicted

at the end of each step from Eq. (29) and porosity measurement. A second order polynomial fit is used to obtain $S(RH)$ according to

$$S(RH) = M_0 + M_1 RH + M_2 RH^2, \tag{42}$$

where M_0, M_1, and M_2 are fitting parameters. Since RH is a function of both x and t, $S(x,t)$ is obtained from Eq. (42). Figure 9 shows the approximation for a specimen of 0.5 w/c at an age of 7 days. Note that the approximation is poor at higher saturation levels, but the pore stress is also the lowest at higher saturation. The obtained curve is of similar form to that suggested by Bazant and Baweja [42]

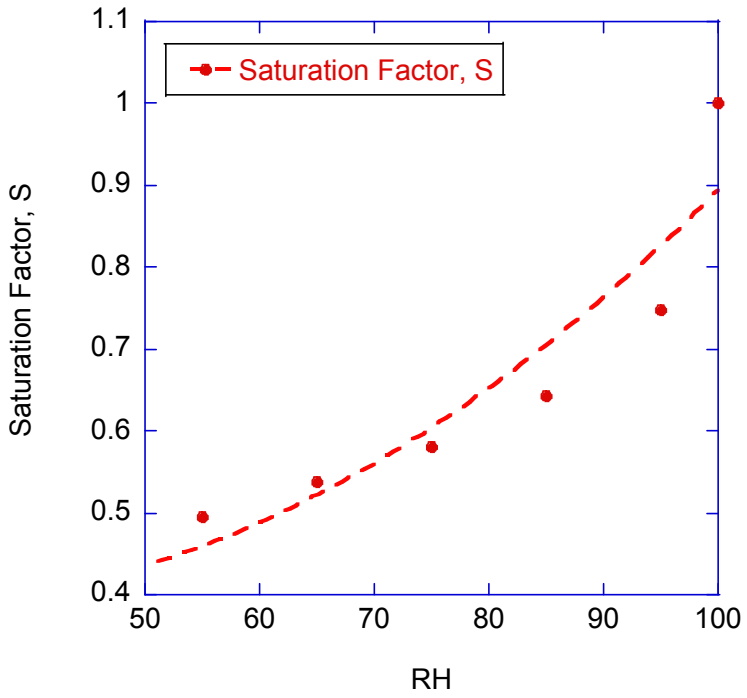

Figure 9: Saturation factor approximation, 0.5 w/c 7 day

Approximation error is much less pronounced at lower RH levels. A cement paste with a lower w/c ratio, such as 0.4, will produce a better fit curve due to a tighter pore size

distribution. Mass loss at the end of 95% RH for lower w/c pastes is much less, producing a flatter desorption isotherm.

4.2.4. Viscoelastic Strain from RH History

The viscoelastic uniaxial compliance, denoted by $J(t)$, is given by

$$J(t) = \frac{1}{E_0} + \frac{1}{E_1} e^{(-t/\tau_1)} + \frac{1}{E_2} e^{(-t/\tau_2)} \quad , \tag{43}$$

where E_0 is the elastic modulus, E_1 and E_2 are viscoelastic components, τ_1 and τ_2 are relaxation times. Eq. (43) is transformed into the transform domain to get $\bar{J}(s)$, then $\bar{J}(s)$ is substituted into Eq. (36). The average viscoelastic shrinkage strain $\bar{\varepsilon}(s)$ in the transformed domain can be determined as

$$\bar{\varepsilon}(s) = \frac{1}{L}\int_0^L \frac{S(x,t)\bar{P}(x,s)}{3}\left(3(1-2\nu)s\bar{J}(s) - \frac{1}{K_{solid}}\right)dx, \tag{44}$$

Note that this is slightly different compared to Eq. (36). $\bar{K}(s)$ is converted to $\bar{J}(s)$ by assuming a constant Poisson's ratio ν .To obtain $\varepsilon(\Delta t)$, an algorithm written for Mathematica by Mallet is used [43, 44]. The algorithm was written based on a numerical inversion technique of Laplace transform developed by Durbin [45]. Inputting values of E_0, E_1 and E_2 allows for numerical integration Eq. (36) at specific time intervals Δt. Shrinkage can be modeled by fitting the experimental data to the fitting parameters of $\varepsilon(\Delta t)$.

4.2.5. Validation of Shrinkage Model

Fitting model by iterating arbitrary viscoelastic parameters may provide a good fit, but it is not supported by actual experimental data. In order to validate the shrinkage model, the viscoelastic fitting parameters from Eq. (43) used to fit the shrinkage data were obtained by fitting for the viscoelastic parameters from data obtained by a creep test considering aging. Aging needs to be accounted for because specimens were sealed in the creep test to avoid drying creep from occuring; this means that the moist specimens will continue to hydrate (age) during the creep test. To account for aging, the solidification theory developed by Bazant et al. [46] was used. Viscoelastic properties were obtained by fitting a Kelvin chain to the test data. The values from the Kelvin chain was then input into the shrinkage model to obtain a shrinkage curve. The viscoelastic parameters from fitting creep test data with only a normal Kelvin chain would also be used as input data into the shrinkage model to compare the differences between using aging and non-aging viscoelastic parameters fit from the creep test.

4.2.6. Viscoelastic Compliance from Experimental Data

Due to higher creep of the cement paste versus concrete, the load applied by the spring in the creep frame was expected to drop by a significant amount in the duration of the test. Load data was obtained from the load cell, as described in Section 3.2.1. The obtained fit curves for the stress and strain data as a function of time were used to calculate viscoelastic compliance fit data. The following fit function is used to fit the stress and strain data

$$\sigma(t), \varepsilon(t) = M_1 + M_2 e^{-M_3 t} + M_4 e^{-M_5 t}, \tag{45}$$

where M_1, M_2, M_3, M_4 and M_5 are fitting parameters. Applying Laplace transform to stress and strain functions obtained in Eq. (45), viscoelastic modulus can be obtained by the following equation

$$s\bar{E}(s) = \frac{\bar{\sigma}(s)}{\bar{\varepsilon}(s)} \tag{46}$$

where $\bar{\sigma}(s)$ and $\bar{\varepsilon}(s)$ are transformed from Eq. (45). Viscoelastic compliance is given by

$$\bar{J}(s) = \frac{1}{s^2 \bar{E}(s)}. \tag{47}$$

Applying inverse Laplace transform to Eq.(47), The viscoelastic compliance $J(t)$ can be obtained for the test data. This is as opposed to a constant stress situation, where the stress function would simply be a constant before Laplace transform is applied.

4.2.7. Obtaining Elastic Moduli and Viscoelastic Parameters

Elastic moduli of the HCP specimens were obtained by loading specimens and using a linear fit to determine the elastic modulus of a stress-strain curve. Viscoelastic parameters from the Kelvin chain from Eq. (43) were fitted to experimental data obtained from the apparatus described in Sections 3.2. Since the specimens of the creep test were sealed to prevent moisture loss, substantial aging occurs during loading and must be accounted for. To account for aging, the solidification theory was used [46]. For solidifying materials,

$$J(t,t') = \frac{1}{E_0 v(t')} + \int_{t'}^{t} \frac{1}{v(\theta)} \frac{\partial J(\theta - t')}{\partial \theta} d\theta, \tag{48}$$

where $J(t,t')$ is the viscoelastic compliance, $J(\theta - t')$ is a Kelvin chain fit equation in the same form as Eq. (43), E_0 is the elastic modulus of the solid phase, and $v(t)$ is the aging function. t' denotes the age at which the specimen is first loaded. As the aging of the cement paste fraction continues, the skeleton stiffens as a function of time. The aging function, $J(t,t')$ was determined by plotting the elastic modulus of the paste at different ages and fitting the following equation:

$$v(t) = \frac{1}{\beta_1 e^{\varpi_1} + \beta_2 e^{\varpi_2}}, \tag{49}$$

where $\beta_1, \beta_2, \omega_1$ and ω_2 are fitting parameters. $v(t')$ was normalized to 1 for the fitting function, which indicates that the specimen at the time of loading has the same stiffness as the elastic modulus when the loading begins. Substituting the values from Eq. (49) into Eq. (48), fitting parameters of Eq. (43) can be found by fitting experimental data obtained in Section 4.2.6.

5. RESULTS AND DISCUSSION

5.1. Porosity

An accurate porosity measurement is essential to determine the saturation level in the desorption isotherm, which in turn affects the shrinkage modeling. Table 2 shows the porosity measurements. Porosities of 0.5 w/c specimens at different ages were obtained previously with the same type of cement. It is seen that the porosities of 0.4 w/c specimens were significantly lower than the porosity of 0.5 w/c pastes.

Table 2: Porosity measurements

Material	Age	Porosity
0.4 w/c	3	0.43
	7	0.37
0.5 w/c	3	0.52
	7	0.47

5.2. RH(S) Approximation

Figure 10-13 shows the fitting of the sigmodial curve against the desorption isotherms. A sigmodial function described in Eq. (31) is able to provide good fits against the final estimated mass loss. The curve fits provide reasonable accuracy for converting mass loss of specimens to concentration of water vapor in air.

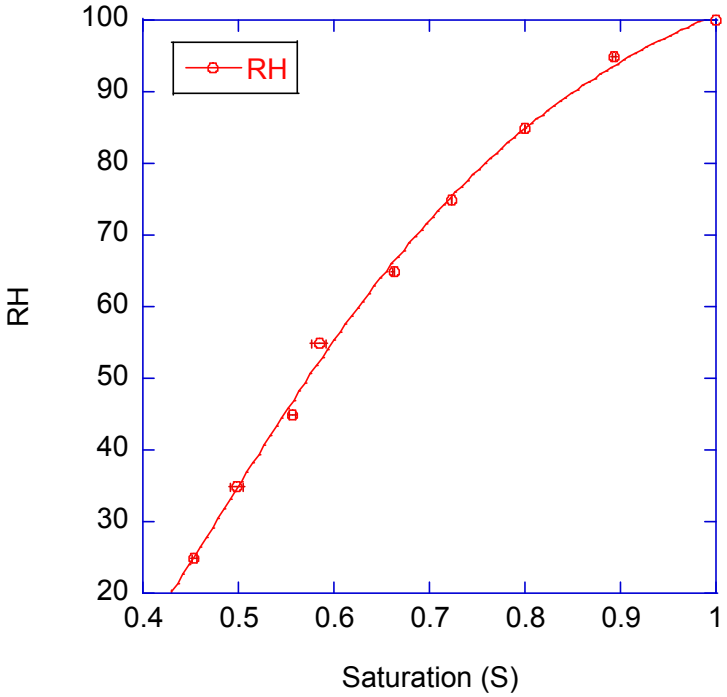

Figure 10: Sigmodial curve fit for *RH(S)*, 0.4 w/c 3 day

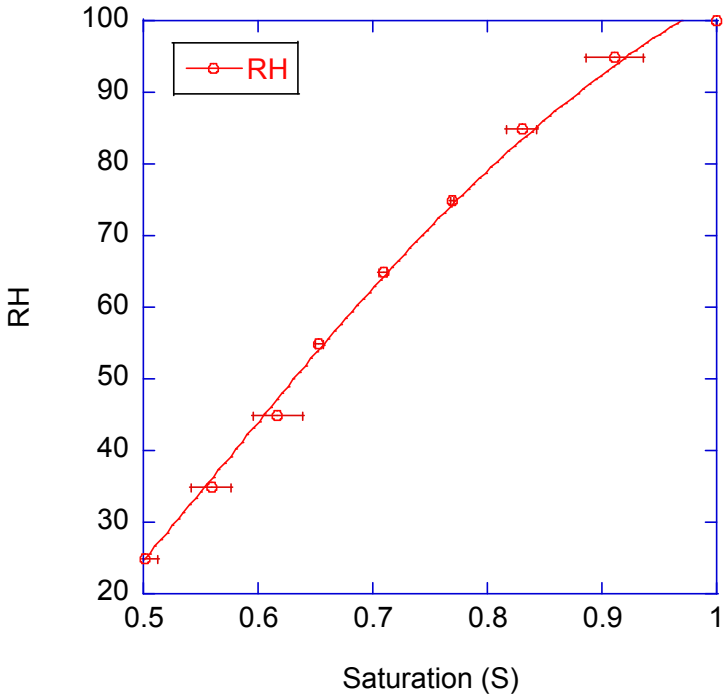

Figure 11: Sigmodial curve fit for *RH(S)*, 0.4 w/c 7 day

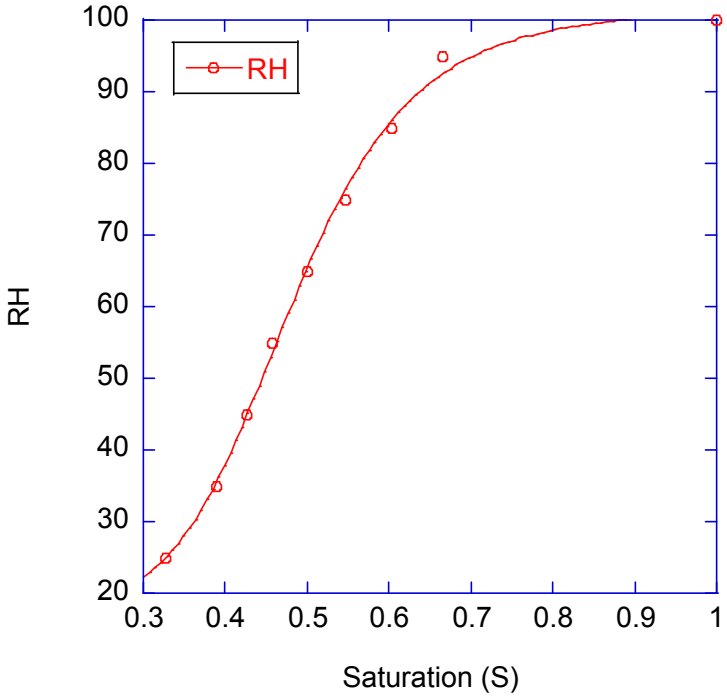

Figure 12: Sigmodial curve fit for *RH(S)*, 0.5 w/c 3 day

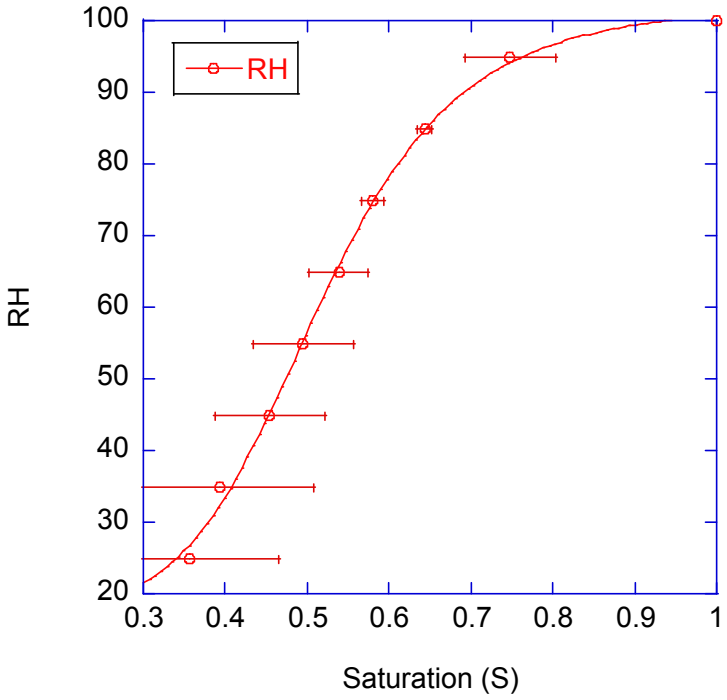

Figure 13: Sigmodial curve fit for *RH(S)*, 0.5 w/c 7day

5.3. Desorption Isotherm in Different Cement Pastes

Figure 14 illustrates the differences in the desorption isotherm *S(RH)* of both 0.4 and 0.5 w/c and at different ages, with mass loss points estimated by Eq. (29). It is evident that the pore size distribution evolves as a function of age due to the continued effect of hydration and decrease in porosity, as the amount of water available in the pore space is decreased due to consumption from hydration. The Kelvin equation can be used to determine pore size distribution as a function of RH of the isotherm. A large drop in saturation at a certain RH indicates a large concentration of pores of a certain size.

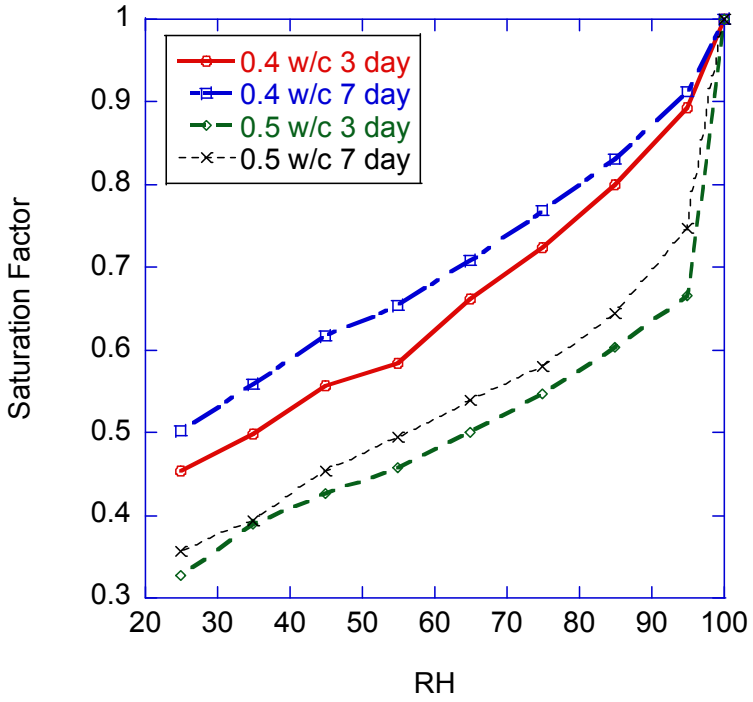

Figure 14: Desorption isotherms of different w/c and age

An extended summary for utilizing the Kelvin equation to determine pore size distribution for porous materials were extensively covered by Lowell and Shields [47]. By rewriting the Kelvin equation with the parameters for water vapor, a pore size distribution (radii of the pores) as a function of RH can be determined. The drop in saturation at the 95% RH indicates that a substantial amount of large pores exist in 0.5 w/c specimens, compared to the 0.4 w/c specimens. This is greatly affected by the w/c ratio, in which the 0.5 w/c specimens have significantly more large pores than 0.4 w/c specimens.

5.4. Diffusion Rates in HCP

Rapid change in RH(S) at higher RH levels causes the conversion from mass loss to RH to be highly non-linear at higher RH levels. Eq. (28) is therefore unable to provide an accurate fit. This is illustrated by Figure 15 for 0.5 w/c pastes at 3 day of age. The remaining fitting curves for 100-95% RH are therefore omitted. At the lower RH steps, however, Eq. (28) fits the experimental data well. The fit curves at each RH step for the materials tested are listed in Appendix A for reference.

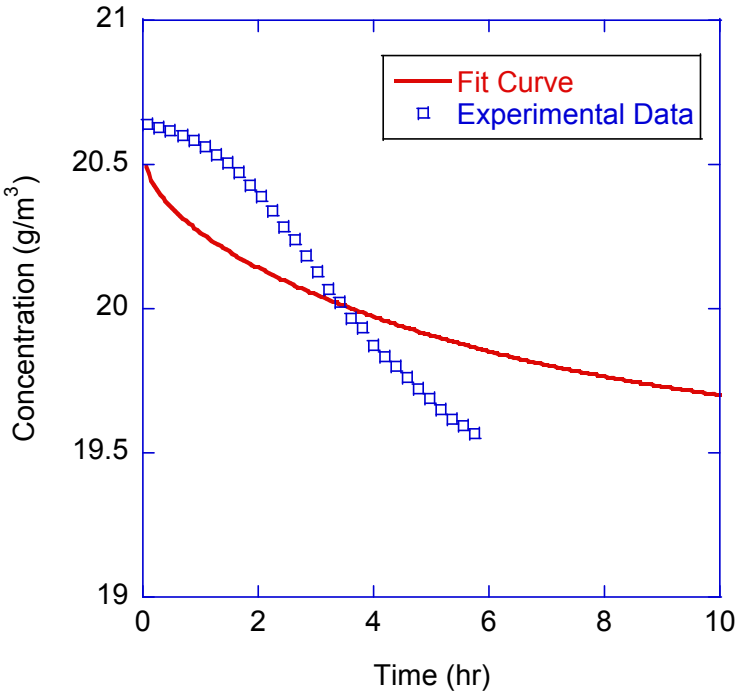

Figure 15: Illustration on the effect of non-linearity of the isotherm on predicted concentration

As shown on the graphs in Appendix A, the approach to account for non-uniform cross section RH is necessary, since mass loss has not been equilibrated at the end of most steps. The remaining diffusion coefficients of HCP strips determined at different RH steps and ages are plotted in Figure 16.

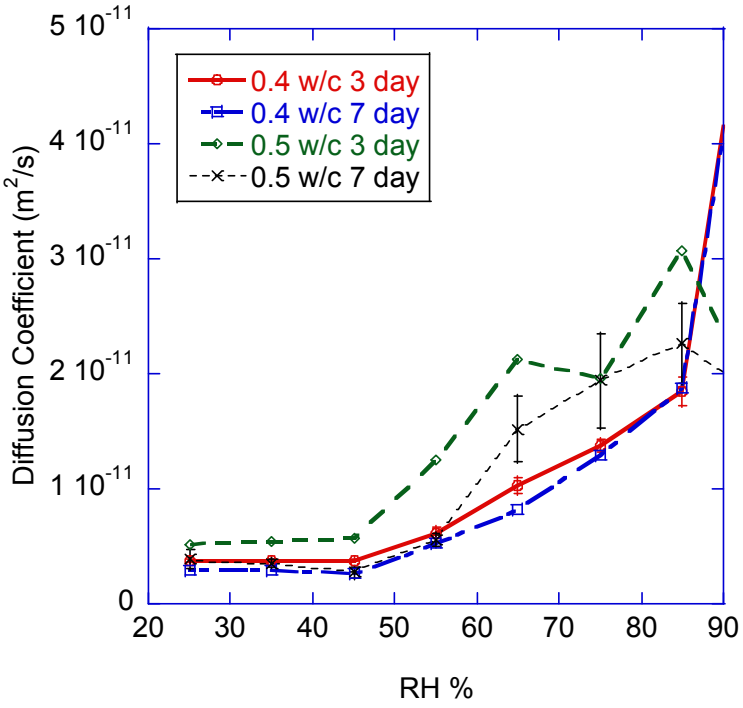

Figure 16: Diffusion coefficient of different w/c and age

A slight difference is noted between ages, and a noticeable difference between w/c ratios. As previously mentioned, due to the non-linearity of the saturation coefficient, the fitting is poor between 100-95% RH for 0.5 w/c specimens. From the mass loss data, however, it is evident that the diffusion rate at higher RH is higher than that of 95-85% RH. The diffusion coefficients were not included at that step as a result. Curve fitting for the other steps are consistent. The diffusion rate of 0.5 w/c specimens is also noted to be higher compared to 0.4 w/c at RH levels above 55%. Diffusion rate lowers as the specimens were dried to a lower RH. Below 50% RH, the diffusion rates

between specimens becomes constant and are very close to one another, with 0.5 w/c 7 day being slightly higher. Similar observations were also made previously [2] and is consistent with the findings of [48]. A lower drying rate indicates that drying takes longer, as shown in the experimental data. For the mass loss, none of the steps below 55% were close to equilibration after 20 hours, comparing to the higher levels of RH, which in general were close to equilibration after ~15 hours. A change in diffusion mechanism is evident from the experimental results. Due to high negative pressure of the pore fluid below 50% RH, instability of the menisci at small pore radii <2nm results [49], as shown by an abrupt change in diffusion coefficient. A 3D representation is shown in Figure 17. It is seen that at 55% RH, moisture equilibration takes significantly longer for this specimen.

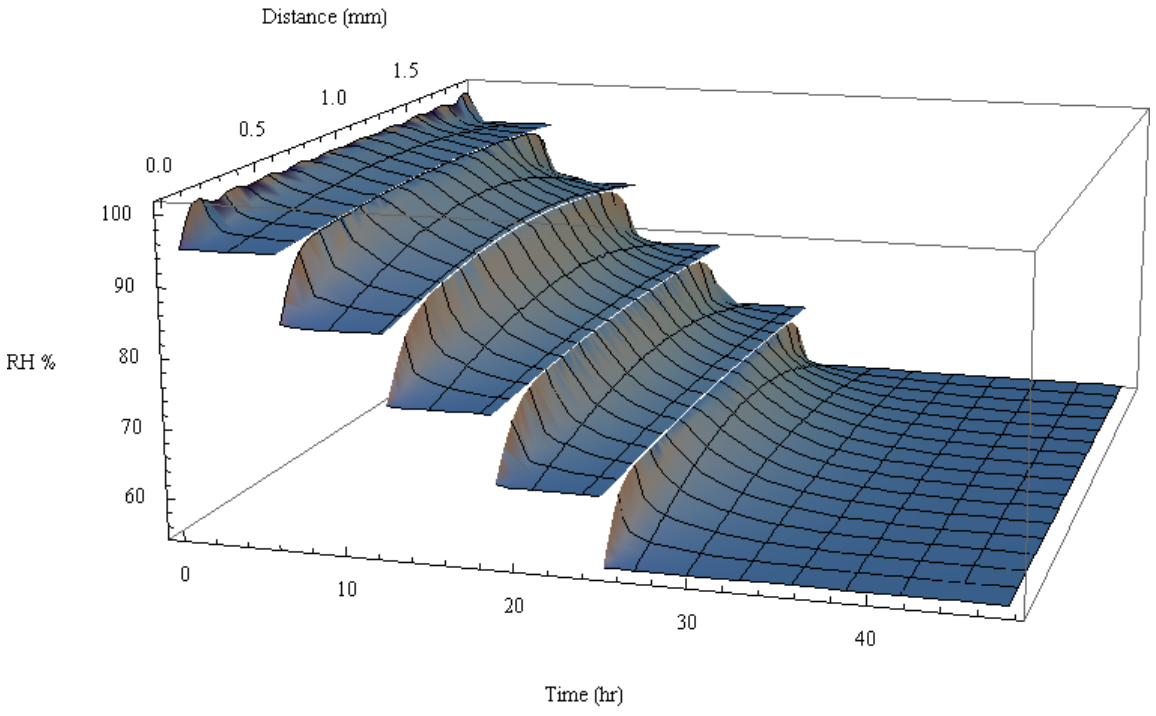

Figure 17: RH of cement paste strip as a function of time and spatial coordinate x

5.5. Shrinkage Modeling

5.5.1. Testing Results from Creep Tests

The stress and strain of the various specimens were plotted and shown in Appendix B. As indicated by the load curve, substantial load loss occurs (over 10% for young specimens) as the specimens creep under load. Strain measurements from the two samples were averaged before creep compliance for a specific material is determined.

Figure 18 shows the viscoelastic compliance functions, determined by fitting experimental data to Eq. (43), (48) and (49) with the elastic component of different w/c ratios and age plotted. A stiffening effect over time is evident. Specimens at age 3 day have higher creep compliance than specimens at age 7 day for both of the w/c ratios. 0.4 w/c ratio specimens have lower creep compliance than a 0.5 w/c ratio, which is expected.

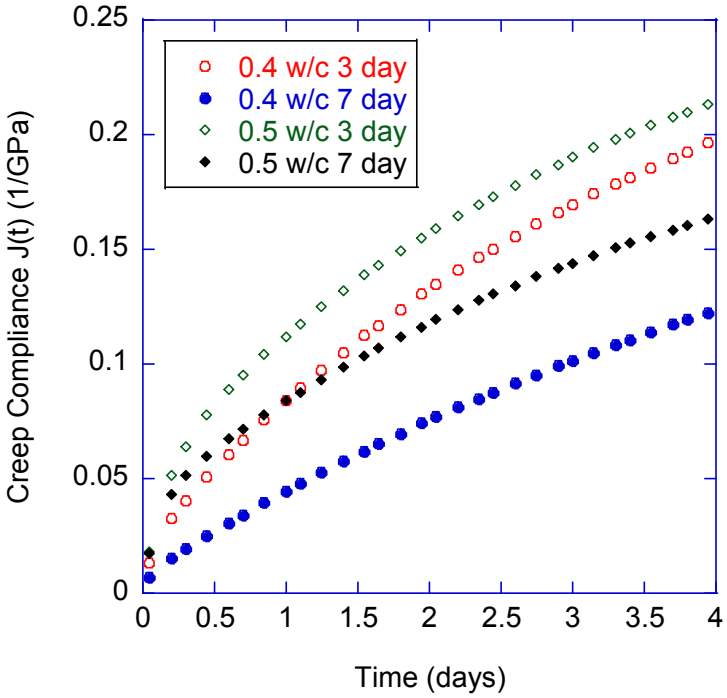

Figure 18: Viscoelastic compliance curve as a function of w/c and age

5.5.2. Obtaining Estimated Aging Function from Elastic Moduli

Elastic moduli listed in Table 3 and plotted in Figure 19 are obtained from testing solid cement paste specimens mounted with LVDT, and from the creep specimens at initial loading. Modulus increases as a function of time, and as a decreasing function of w/c ratio.

Table 3: Elastic moduli from uniaxial compression test

Material	Age (days)	Elastic Moduli (GPa)	Coefficient of Variation
0.4 w/c	3	17.64	5.1%
	7	21.51	26.1%
0.5 w/c	3	8.97	11.5%
	7	12.18	30.4%

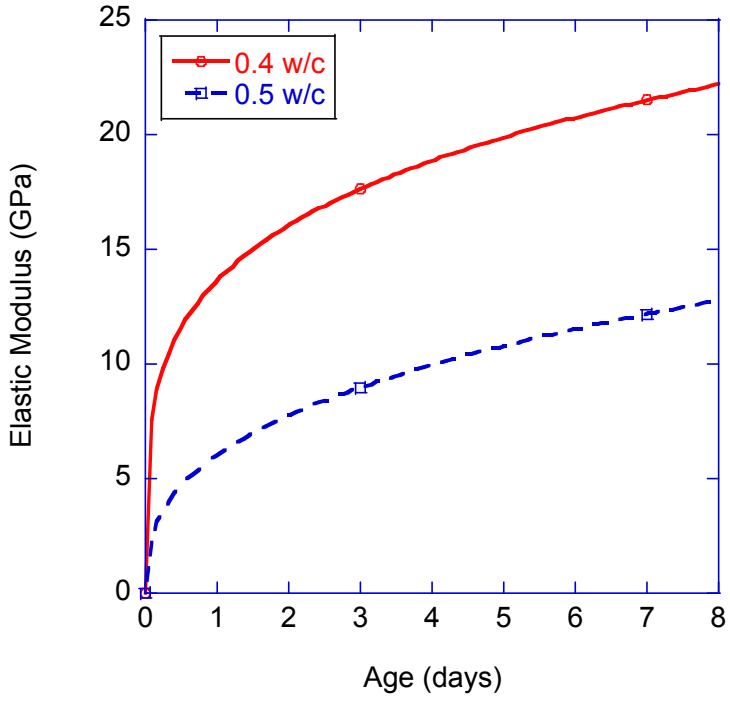

Figure 19: Elastic moduli as a function of age

In order to account for aging during the creep tests, estimated aging functions need to be obtained for the specific materials. The fitting parameters for the aging functions were obtained by normalizing the elastic moduli from Table 3 at the age of testing for the specimens. Table 4 shows the parameters used to fit Eq. (49) to the aging parameters. Figure 20 shows the fitted aging functions.

Table 4: Aging parameters used in viscoelastic moduli determination

Material	Age	β_1	β_2	ω_1	ω_2
0.4 w/c	3	0.6	0.85	0.4	0.01
	7	0.8	1.1	0.5	0.015
0.5 w/c	3	1.1	0.72	0.4	0.01
	7	1.7	1.05	0.5	0.015

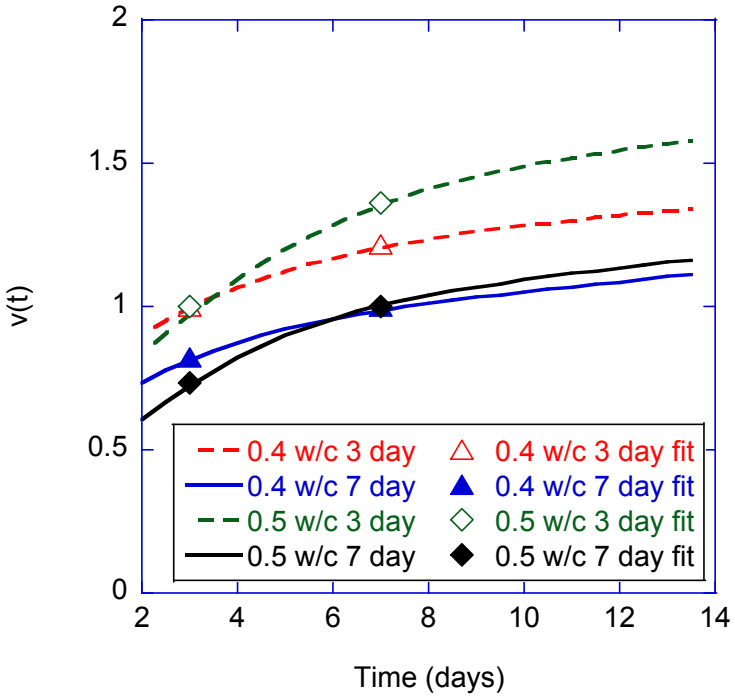

Figure 20: Aging function v(t) plotted vs. time

5.5.3. Viscoelastic Parameters

The obtained elastic moduli and viscoelastic moduli from the Kelvin chain for the shrinkage model based on Eq. (44) are shown in Table 5. Retardation times were selected to be 1 and 10 days. Non-aging viscoelastic moduli were determined from fitting the creep data directly without accounting for aging with the solidification theory. A large value of creep compliance indicates that the viscoelastic effect for the selected retardation time is minimal, as shown in the case of an aging fit for 0.5 w/c 7 day specimens.

Table 5: Determined viscoelastic moduli internal variables

Material	Age		E_1 (τ_1=1)	E_2 (τ_2=10)
0.4 w/c	3	Aging	848.3	3.26
		Non-Aging	17.59	2.49
0.5 w/c	3	Aging	507.4	4.37
		Non-Aging	10.4	3.46
	7	Aging	185,072	6.52
		Non-Aging	16.73	4.00

Viscoelastic compliance curves were plotted from the creep tests. The data points were obtained by fitting Eq. (31) to the stress and strain experimental data, and the viscoelastic compliance in the transform domain was obtained by transforming the curve fit functions in Eq. (45). The strains from the specimens were averaged in the viscoelastic compliance function calculation. The fitting curves were obtained by accounting for aging with Eq.(48), and the aging function Eq. (49). Viscoelastic compliance plotted with fitting parameters from a Kelvin chain without using solidification theory to account for aging were identical compared to viscoelastic fitting parameters with aging. Figure 21 shows the fitting of the total viscoelastic creep, including the elastic moduli.

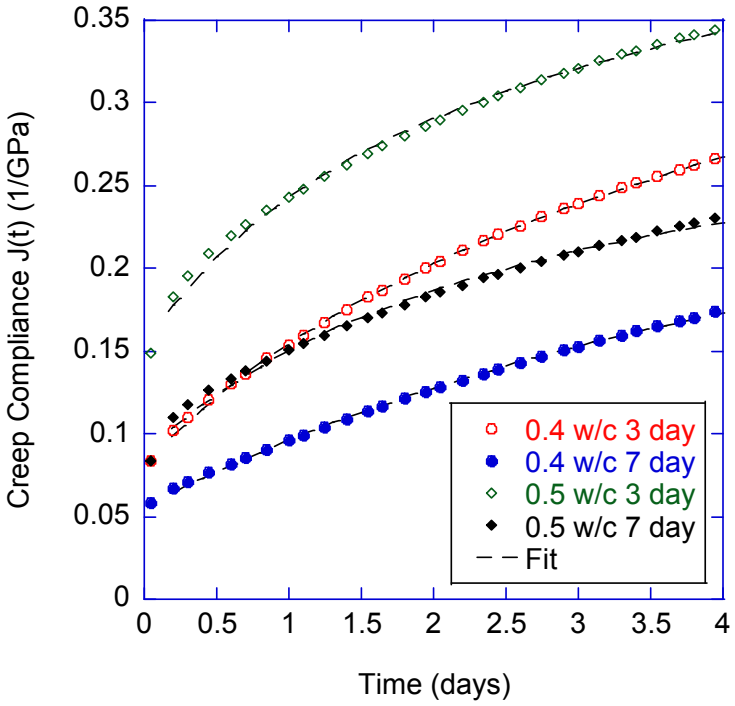

Figure 21: Fitting of total viscoelastic creep compliance curves

5.6. Modeling of Thin Cement Paste Strip

All of the Phenolphthalein solution sprayed on the thin HCP paste at the conclusion of the experiments turned pink, indicating a pH of 12 or higher. This result shows that carbonation of the cement paste from the air circulating in the chamber is minimal. The measured shrinkage data is thus attributed to moisture transport only.

Moduli, as determined from the previous section, were inserted into Eq. (44). The results were plotted against the measured data in Figure 22-29, respectively. Non-aging viscoelastic moduli, as expected, predicted greater shrinkage when utilized in the model. Aging of the shrinkage specimens was neglected due to the RH dropping below

70% in a relatively short amount of time, whereas aging continues in the creep specimens. Hydration ceases at RH below about 75% [50]. The results show a good agreement between the experimental data and modeled data for a 0.5 w/c ratio, especially for a 7 day old specimen.

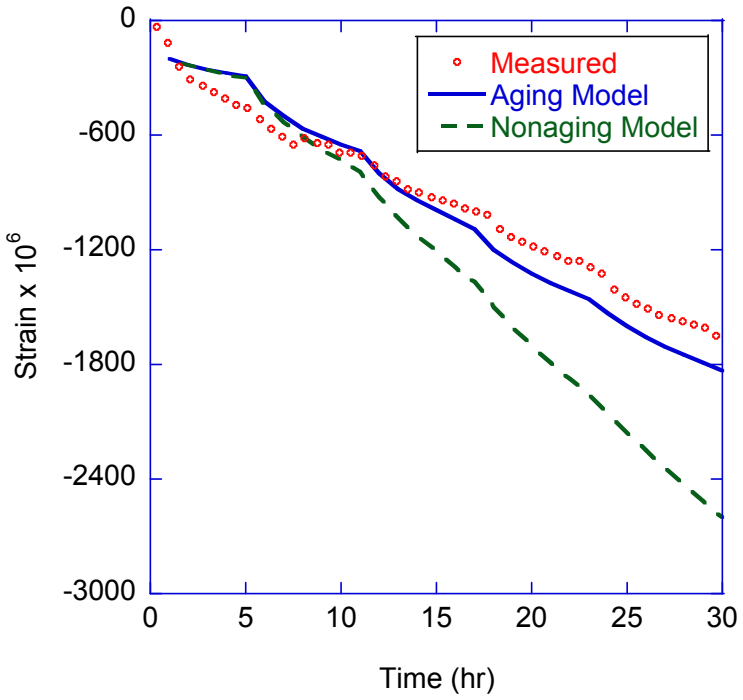

Figure 22: Shrinkage model vs. measured data, 0.4 w/c, age: 3 day specimen 1

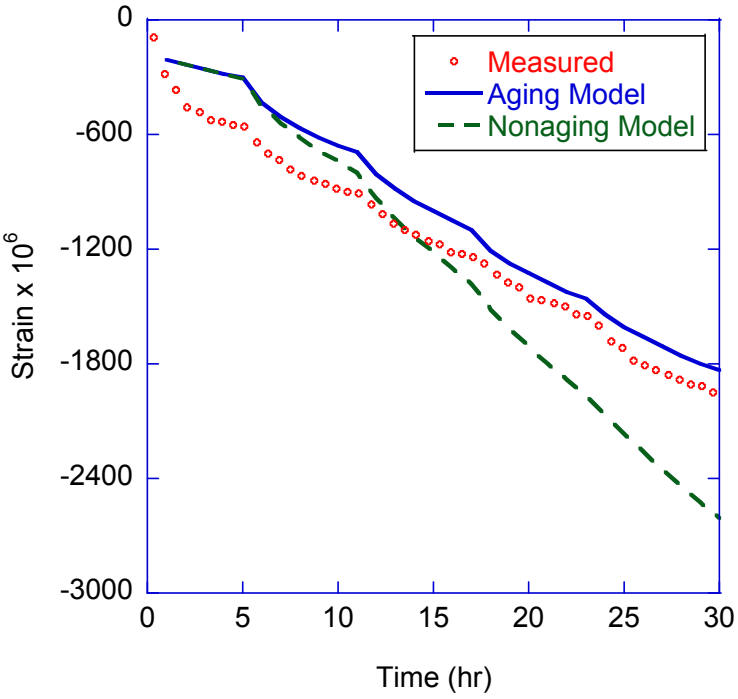

Figure 23: Shrinkage model vs. measured data, 0.4 w/c, age: 3 day specimen 2

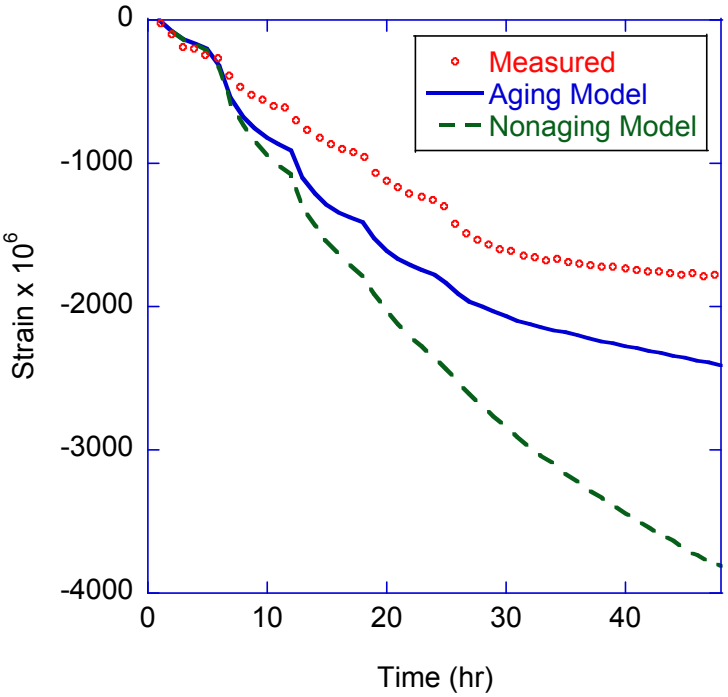

Figure 24: Shrinkage model vs. measured, 0.5 w/c, age: 3 day, specimen 1

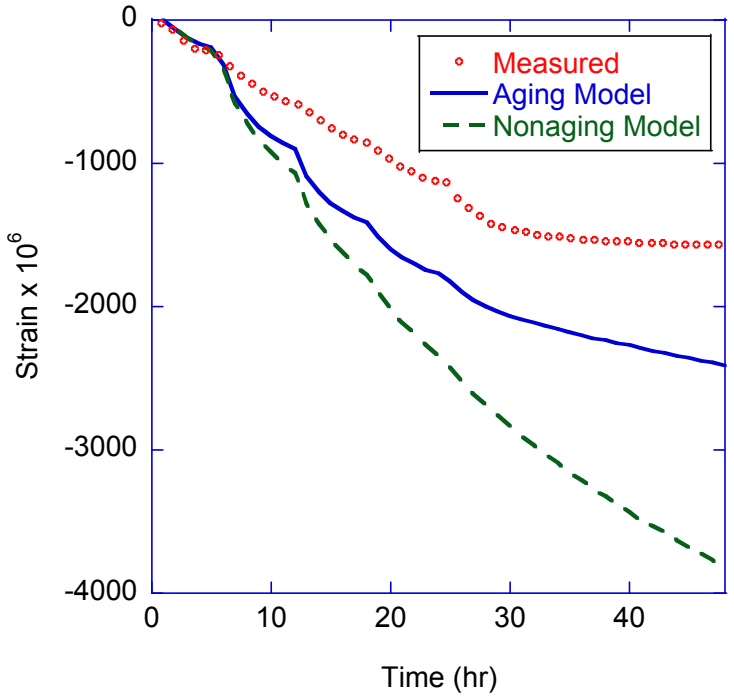

Figure 25: Shrinkage model vs. measured, 0.5 w/c, age: 3 day, specimen 2

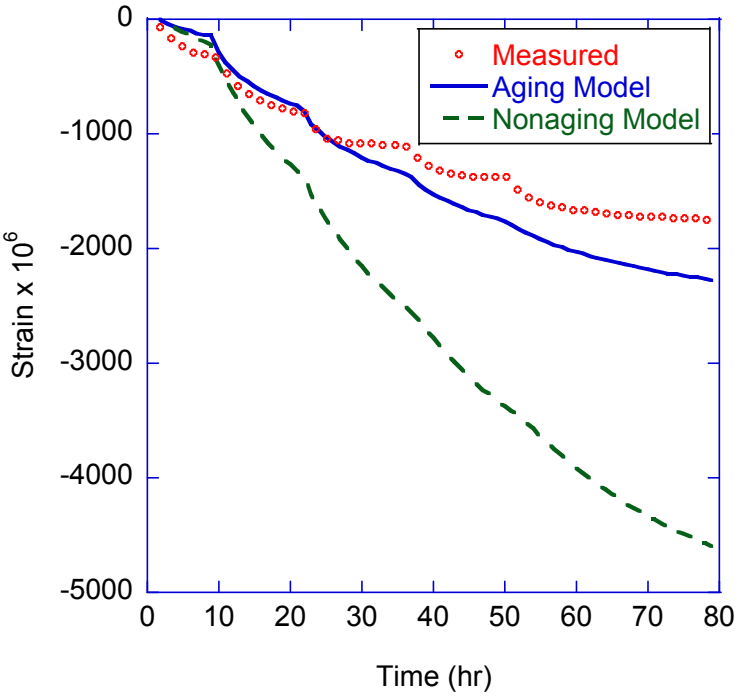

Figure 26: Shrinkage model vs. measured, 0.5 w/c, age: 7 day, specimen 1

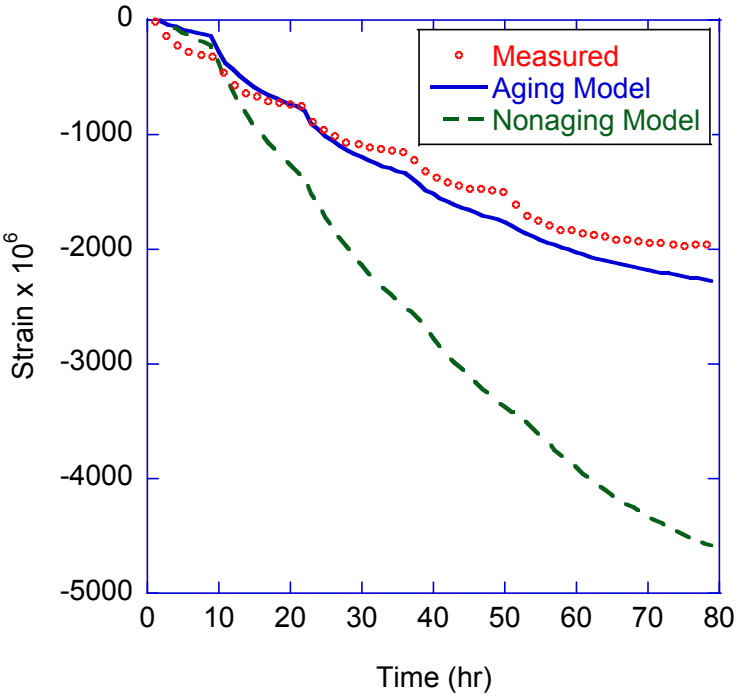

Figure 27: Shrinkage model vs. measured, 0.5 w/c, age: 7 day, specimen 2

The quality of fit for 0.4 w/c specimens were not as good as the fits of 0.5 w/c specimens. This can be attributed to the assumption of the diffusion coefficients being constant for the entire range. A steep drop off in diffusion coefficient is noted in Figure 16 for 0.4 w/c ratios, indicating that the drying rate at high RH of 0.4 w/c samples were much faster than the drying rate at lower RH. Despite the shrinkage rate varying between ages, as observed from Figures 27-28 vs. 29-30 for 0.5 w/c pastes, the final shrinkage does not vary by a significant amount. This is also noted for 0.4 w/c pastes compared to 0.5 w/c pastes.

The approximation explained in Section 4.2.2 introduces error in the beginning of the test. Combined with the effect of averaging a diffusion coefficient for the purpose of shrinkage model, some errors were evident in the modeling. When a smaller than actual diffusion coefficient was used, the internal RH change is underestimated, since mass loss from the pore space is modeled to be slower. This leads to an under prediction of the shrinkage and shrinkage rate in the beginning due to a higher actual stress being applied. This was accounted for by shifting the curve obtained from fitting, where the strain is zero, to the shrinkage value from experiments at the corresponding time. Figure 28 illustrates the procedure.

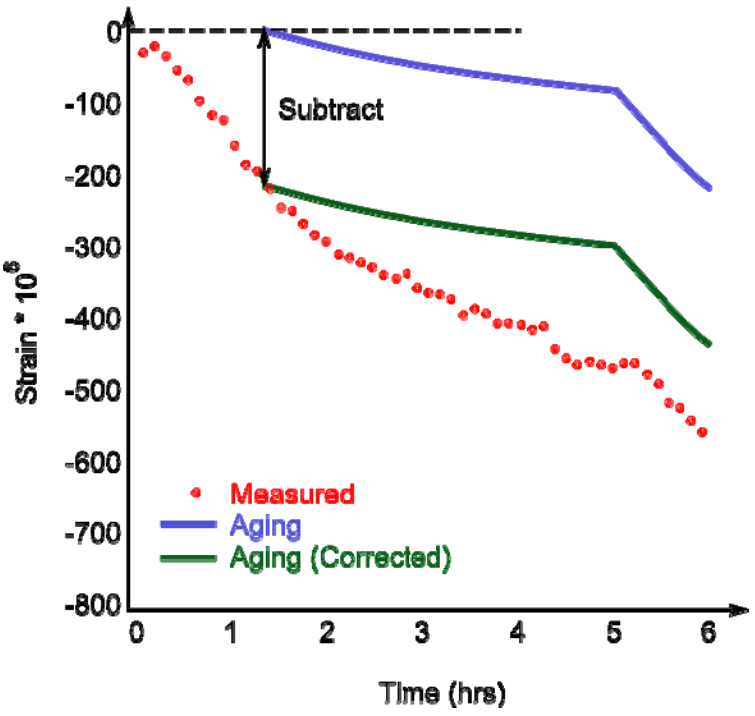

Figure 28: Illustration of shifting shrinkage curve due to stress approximation error

A similar situation arises at lower RH, where the stress is over predicted, leading to higher shrinkage predicted than observed. The error in the assumption of neglecting aging due to a short time of the drop from 95% to 75% RH is clearly illustrated on Figure 24 and Figure 25. For a 0.5 w/c paste, the time step from 95% to 75% RH was 20 hours. The shrinkage model over predicts the shrinkage due to the assumption of no aging. In reality, aging occurs in that 20 hour period in which hydration continues because RH is over 70%. Such difference is less pronounced in a 0.4 w/c paste. This may be attributed to the aging behavior differences of 0.4 and 0.5 w/c pastes. The model accurately predicts shrinkage for 0.5 w/c at 7 day age, indicating that the aging is significantly less pronounced. This is also noted by the increase in magnitude of elastic modulus shown in Table 3. For 0.5 w/c HCP, the Young's modulus increases 35.7% between 3 and 7 days, compared to 21.9% of 0.4 w/c paste. Elastic and viscoelastic stiffness gain as a function of water/cement ratio is a subject of further research. The method currently used considers a diffusion coefficient averaged over all the RH steps. More accurate predictions can be made by solving the diffusion equation with diffusion coefficients varying as a function of time/RH.

The difference of viscoelastic parameters due to accounting for aging in Eq.(48) is also noted when applied to the shrinkage modeling. Non-aging parameters significantly over predicts the shrinkage in 0.5 w/c pastes, and a less substantial, but still very pronounced over prediction is also evident in 0.4 w/c pastes. This is due to the stiffening of the cement paste during the creep test due to continued hydration, in which specimens were sealed to prevent drying from occurring.

6. SUMMARY AND CONCLUSIONS

Mass loss and shrinkage data was collected continuously on thin HCP pastes subjected to small change in RH steps during the testing program. Analysis methods on drying diffusion were developed accounting for non-equilibrated mass loss at the conclusion of each RH step. A model predicting shrinkage is also presented by the use of poromechanics and solidification theory of aging cementitious materials.

Diffusivity rate of water vapor decreases as ambient RH is lowered. Using modeling techniques described, desorption isotherm and diffusion coefficient as a function of RH were obtained from measured data. Mass loss data is converted into concentration of water vapor in air with the obtained desorption isotherm, and drying diffusion rate can be determined by fitting a modified solution of Fick's law of diffusion.

Drying shrinkage may be modeled as a poroviscoelastic response. With the determination of drying diffusion coefficients described in the diffusion modeling, RH history is recreated and used to model viscoelastic shrinkage. Shrinkage modeling is verified by performing creep tests in order to obtain the viscoelastic parameters.

6.1. Conclusion

Desorption isotherm changes as w/c is lowered and as the cement paste ages, indicating that the pore size distribution changes when a lower w/c is used (less porosity) and as hydration products form for the case of aging. It is seen that the diffusion coefficient lowers as RH decreases. At below 50% RH, the diffusion coefficients for all of the specimens tested were very similar. This can be attributed to a change in diffusion

mechanisms for water in porous media at smaller pore sizes. The observed decrease in diffusivity of water vapor at lower RH is consistent with previous findings.

With the obtained diffusion coefficients, shrinkage can be modeled with the RH history by using an average diffusion coefficient. Final shrinkage amount is not affected by the w/c and age for similar RH histories. Approximating the pore stress as a linear function introduces slight error in the modeling. The modeling technique, utilizing poroviscoelasticity, shows satisfactory results when used with viscoelastic parameters determined by creep tests accounting for aging. The determination of viscoelastic parameters must account for aging for early age specimens, due to substantial increase in both elastic and viscoelastic stiffness. However, the assumption of a constant diffusion coefficient introduces error in the higher and lower range of RH due to the stress approximation, as well as the constant diffusion coefficient used.

6.2. Future Work

Diffusion modeling techniques presented herein will be used to study shrinkage reducing mechanisms of shrinkage reducing admixtures (SRA) in HCP pastes by comparing the drying rate, as well as desorption isotherm (change in saturation) of specimens containing SRA. More accurate modeling can be done by considering diffusion rate that varies with RH. To improve prediction accuracy of drying shrinkage, several techniques, including finite difference method, can be utilized to model viscoelastic shrinkage accounting for non-linear diffusion rate. Using the actual stress predicted by the Kelvin equation will also improve prediction accuracy.

REFERENCES

[1] Scherer, G.W., Theory of drying. Journal of the American Ceramic Society, 73(1) (1990) 3-14.

[2] Bazant, Z.P., Najjar, L. J., Drying of concrete as a nonlinear diffusion problem. Cement and Concrete Research, (1) (1971) 461-473.

[3] Bazant, Z.P., W.J. Raftshol, Effect of cracking in drying and shrinkage Specimens. Cement and Concrete Research, 12(2) (1982) 209-226.

[4] Bazant, Z.P., Najjar, L.J., Nonlinear water diffusion in nonsaturated concrete. Materials and Structures, 5 (1972)3-20.

[5] Sarott, F.A., M.H. Bradbury, P. Pandolfo, P. Spieler, Diffusion and adsorption studies on hardened cement paste and the effect of carbonation on diffusion rates. Cement and Concrete Research, 22(2-3) (1992) 439-444.

[6] Hansen, W., Drying shrinkage mechanisms in portland cement paste. American Ceramic Society, 79(5) (1987) 323-328.

[7] Powers, T.C. Mechanisms of shrinkage and reversible creep of hardened cement paste. Properties of Concrete., New York, 1963, p.319-344

[8] Powers, T.C., The thermodynamics of volume change and creep. Materials and Structures, 1(6) (1968). 487-507.

[9] Wittmann, F.H., Interaction of hardened cement paste and water. Journal of the American Ceramic Society, 56(8) (1973). 409-415.

[10] Powers, T.C. Fourth international symposium on the chemistry of cement, monograph 43. National Bureau of Standards. 1962. Washington, DC U.S. Department of Commerce.

[11] Feldman, R.F., P.J. Sereda, Sorption of water on compacts of bottle-hydrated cement I. sorption + length-change isotherms. Journal of Applied Chemistry, 14(2) (1964). 87-94.

[12] Ferraris, C.F., F.H. Wittmann, Shrinkage mechanisms of hardened cement paste. Cement and Concrete Research, 17(3) (1987). 453-464.

[13] Beltzung, F., F.H. Wittmann, Role of disjoining pressure in cement based materials. Cement and Concrete Research, 35(12) (2005). 2364-2370.

[14] Thomson, W.T., Kinetic theory of gases. Philosophical Magazine, 42 (1871) 448

[15] Wahab, M., T. Zehl, U. Reimer, H.J. Mogel, P. Schiller, Simulation of fluid bridges and films. Physical Chemistry Chemical Physics, 5(21) (2003) 4880-4884.

[16] Ayano, T., F.H. Wittmann, Drying, moisture distribution, and shrinkage of cement-based materials. Materials and Structures, 35(247) (2002) 134-140.

[17] Bazant, Z.P., S. Baweja, P. Acker, I. Carol, J. Catarino, J.C. Chern, C. Heut, F.H. Wittmann, D. Carreira, Creep and shrinkage prediction model for analysis and design of concrete structures - model B-3. Materials and Structures, 28(180) (1995) 357-365.

[18] *CEB-FIP Model Code 1990*. 1990, Comité Euro-International du Béton: Lausanne, Mar. pp. 2-3, 2-28 to 2-40.

[19] ACI-209R-82: Prediction of creep, shrinkage and temperature effects in concrete structures, in ACI Committee 209. 1982, American Concrete Institute: Detroit, MI.

[20] Hansen, W., Constitutive model for predicting ultimate drying shrinkage of concrete. Journal of the American Ceramic Society, 70(5) (1987) 329-332.

[21] Biot, M.A., General theory of three-dimensional consolidation. Journal of Applied Physics, 12(2) (1941) 155-164.

[22] Terzaghi, K., Theoretical Soil Mechanics. J. Wiley & Sons , New York., 1943.

[23] Hudson, J.A., Comprehensive Rock Engineering : Principles, Practice & Projects. 1st ed., Pergamon Press, New York, 1993.

[24] Wang, H., Theory of linear poroelasticity : with applications to geomechanics and hydrogeology. Princeton Series in Geophysics. 2000, Princeton, N.J.: Princeton University Press. xii, 287 p.

[25] Detournay, E., Cheng, A.H.-D., Fundamentals of poroelasticity, Comprehensive Rock Engineering: Principles, Practice and Projects. Pergamon Press., New York, 1993.

[26] Biot, M.A., Theory of elasticity and consolidation for a porous anisotropic solid. Journal of Applied Physics, 26(2) (1955) 182-185.

[27] Bentz, D.P., E.J. Garboczi, D.A. Quenard, Modelling drying shrinkage in reconstructed porous materials: application to porous Vycor glass. Modelling and Simulation in Materials Science and Engineering, 6(3) (1998) 211-236.

[28] Read, W.T., Stress analysis for compressible viscoelastic materials. Journal of Applied Physics, 21(7) (1950) 671-674.

[29] Grasley, Z.C., Measuring and modeling the time-dependent response of cementitious materials to internal stresses, Ph.D. thesis, Department of Civil Engineering. 2006, University of Illinois: Urbana-Champaign.

[30] Fu, Y., P. Gu, P. Xie, J.J. Beaudoin, Development of eigenstress due to drying shrinkage in hardened portland-cement pastes - Thermomechanical Analysis. Cement and Concrete Research, 24(6) (1994) 1085-1091.

[31] Benboudjema, F., F. Meftah, J.M. Torrenti, A viscoelastic approach for the assessment of the drying shrinkage behaviour of cementitious materials. Materials and Structures, 40(2) (2007) 163-174.

[32] Day, R.L., P. Cuffaro, J.M. Illston, The effect of rate of drying on the drying creep of hardened cement paste. Cement and Concrete Research, 14(3) (1984) 329-338.

[33] Wang, T.C. J.P. Krivan, CO2 Absorption capacity of new and old lithium hydroxide used in underwater life support systems. Sea Technology, 18(12) (1977) 13-14.

[34] Jaunsen, J.R., The behavior and capabilities of lithium hydroxide-carbon dioxide scrubbers in a deep sea environment. United States Naval Academy, Annapolis, Annapolis, MN,1989.

[35] ASTM Standard C 305-06, Standard practice for mechanical mixing of hydraulic cement pastes and mortars of plastic consistency. 2006, ASTM International, West Conshohocken, PA, 2006.

[36] ASTM Standard C 512-02, Standard test method for creep of concrete in compression. ASTM International, West Conshohocken, PA, 2002.

[37] ASTM Standard C 469-94, Standard test method for static modulus of elasticity and poisson's ratio of concrete in compression. ASTM International, West Conshohocken, PA, 1994.

[38] Pickett, G., The effect of change in moisture content on the creep of concrete under a sustained load. American Concrete Institute Journal, 36 (1942) 333-355.

[39] ASTM Standard C 617-98: Standard practice for capping cylindrical concrete specimens. ASTM International, West Conshohocken, PA, 1998

[40] Lowe, P.R., Approximating polynomial for computation of saturation vapor-pressure. Journal of Applied Meteorology, 16(1) (1977) 100-103.

[41] Constantinides, G., F.J. Ulm, The effect of two types of C-S-H on the elasticity of cement-based materials: Results from nanoindentation and micromechanical modeling. Cement and Concrete Research, 34(1) (2004) 67-80.

[42] Bazant, Z.P., S. Baweja, Justification and refinements of model B3 for concrete creep and shrinkage 2. updating and theoretical basis. Materials and Structures, 28(182) (1995) 488-495.

[43] Mathematica., Wolfram Research, Inc, Champaign, IL, 1988-2008.

[44] Mallet, A., Numerical inversion of laplace transform (code written for Mathematica). 2000.

[45] Durbin, F., Numerical inversion of laplace transforms - efficient improvement to Dubner and Abates method. Computer Journal, 17(4) (1974) 371-376.

[46] Carol, I., Z.P. Bazant, Viscoelasticity with aging caused by solidification of nonaging constituent. Journal of Engineering Mechanics-ASCE, 119(11) (1993) 2252-2269.

[47] Lowell, S., J.E. Shields, Powder surface area and porosity. 2nd ed. Powder technology series. Chapman and Hall, New York, 1984.

[48] Xi, Y.P., Z.P. Bazant, L. Molina, H.M. Jennings, Moisture diffusion in cementitious materials - moisture capacity and diffusivity. Advanced Cement Based Materials, 1(6) (1994) 258-266.

[49] Mindess, S., J.F. Young, and D. Darwin, Concrete. 2nd ed. Prentice Hall, Upper Saddle River, NJ, 2003.

[50] Jensen, O.M., Thermodynamic limitation of self-desiccation. Cement and Concrete Research, 25(1)(1995) 157-164.

APPENDIX A

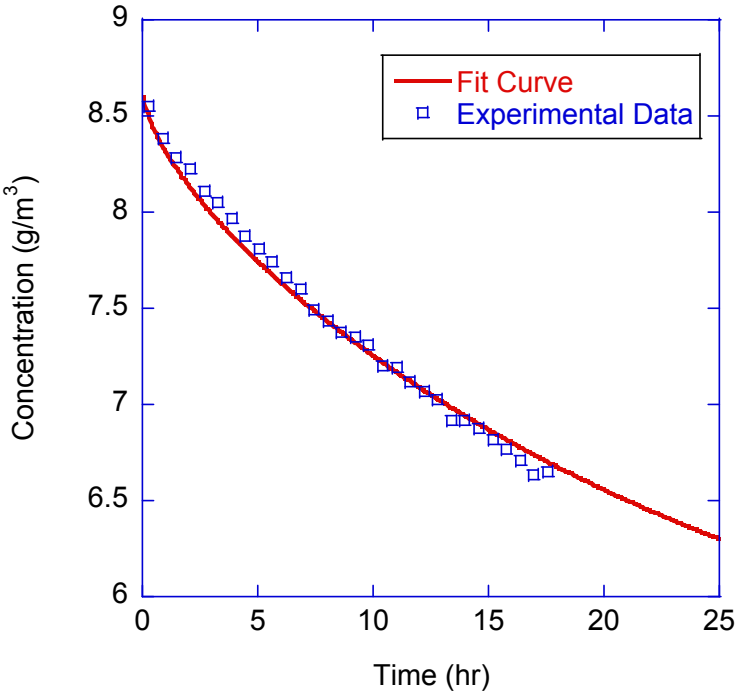

Figure 29: Fitting for diffusion coefficient, 35-25% RH 0.4 w/c 3 day specimen 1

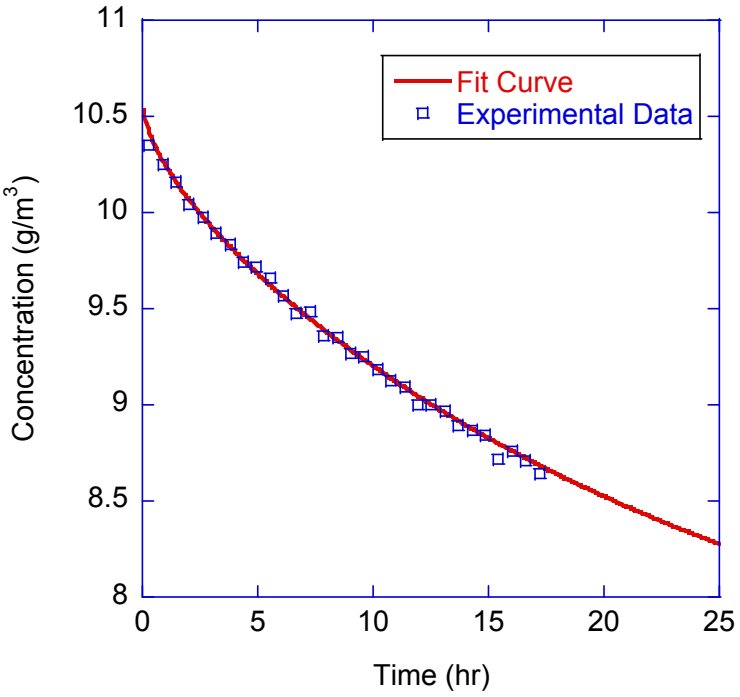

Figure 30: Fitting for diffusion coefficient, 45-35% RH 0.4 w/c 3 day specimen 1

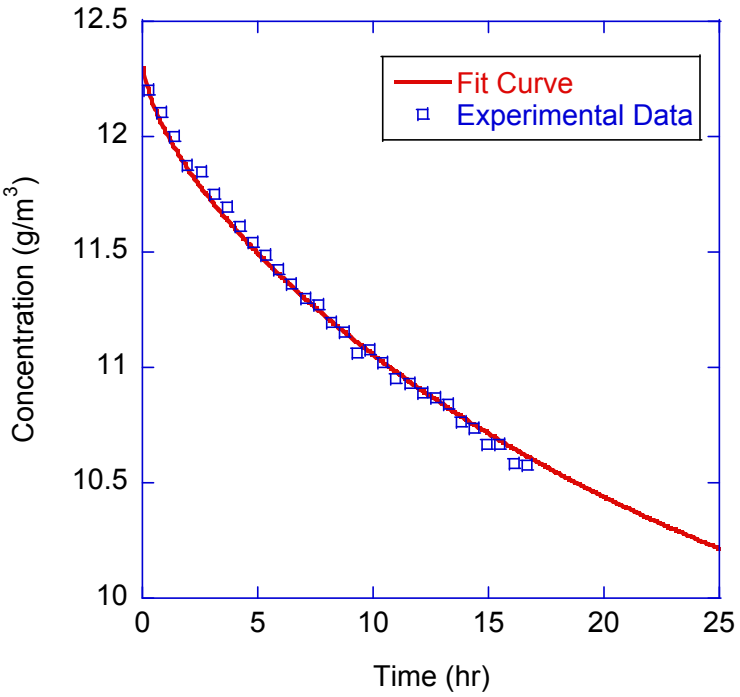

Figure 31: Fitting for diffusion coefficient, 55-45% RH 0.4 w/c 3 day specimen 1

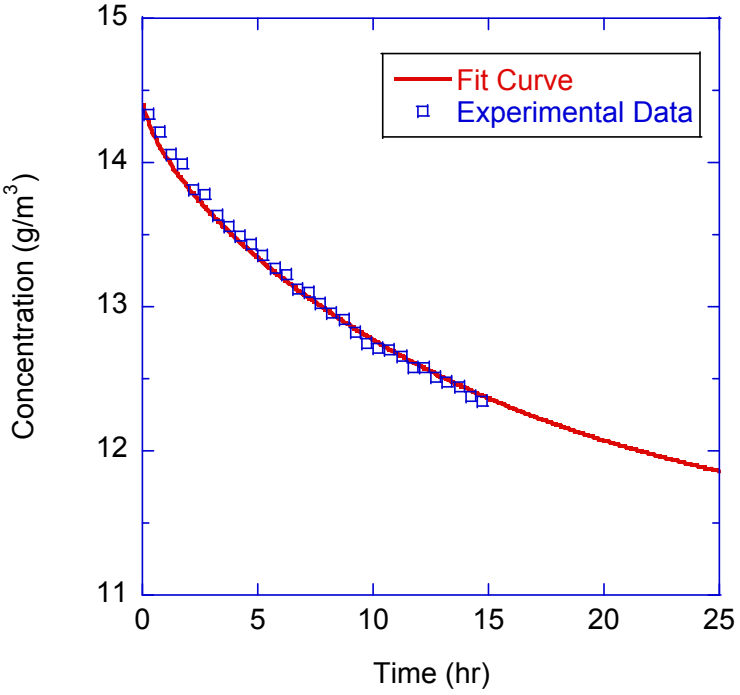

Figure 32: Fitting for diffusion coefficient, 65-55% RH 0.4 w/c 3 day specimen 1

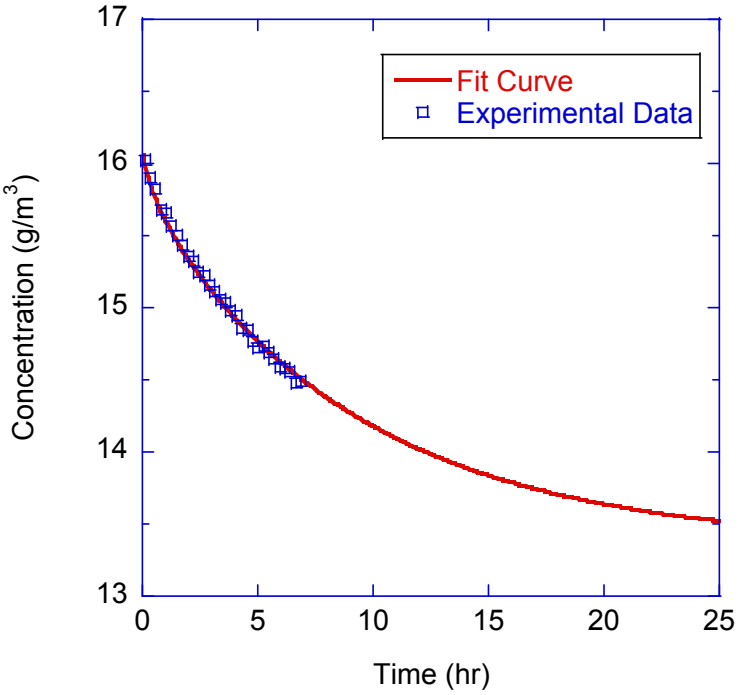

Figure 33: Fitting for diffusion coefficient, 75-65% RH 0.4 w/c 3 day specimen 1

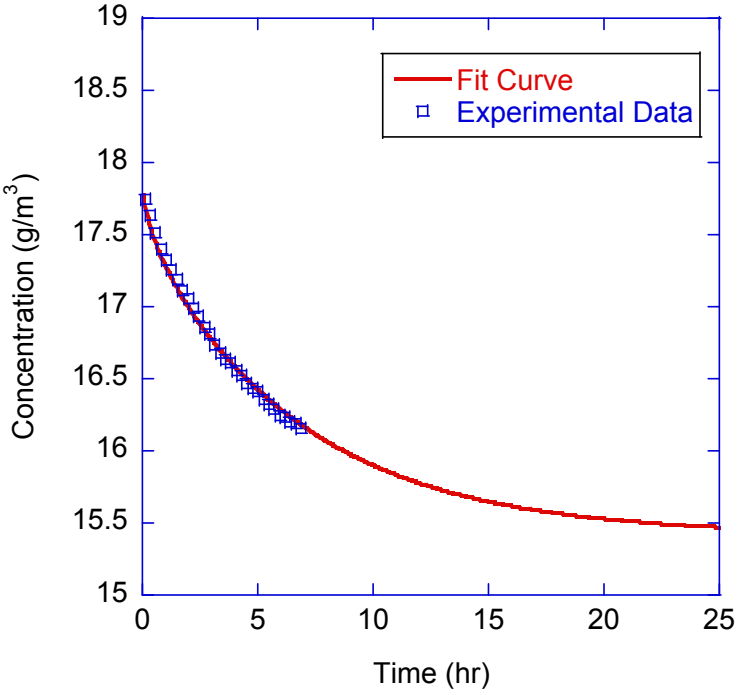

Figure 34: Fitting for diffusion coefficient, 85-75% RH 0.4 w/c 3 day specimen 1

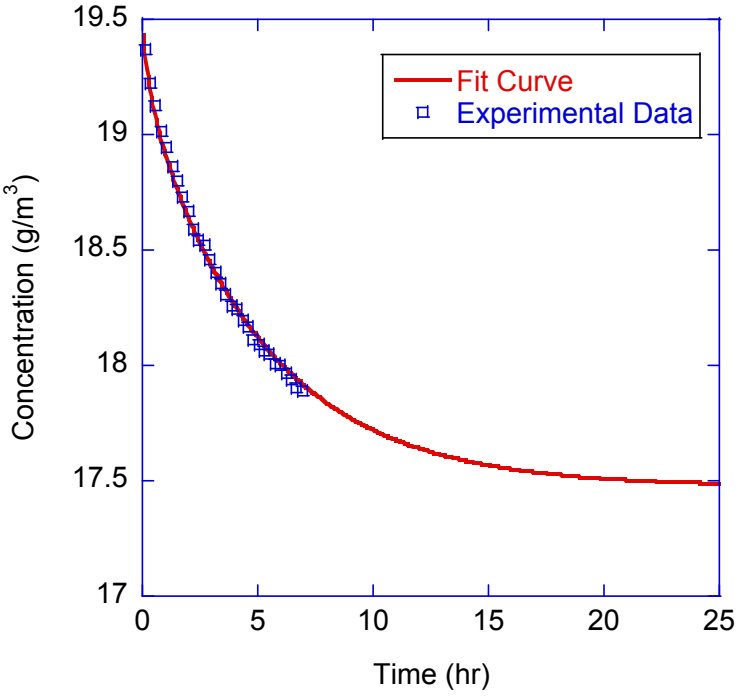

Figure 35: Fitting for diffusion coefficient, 95-85% RH 0.4 w/c 3 day specimen 1

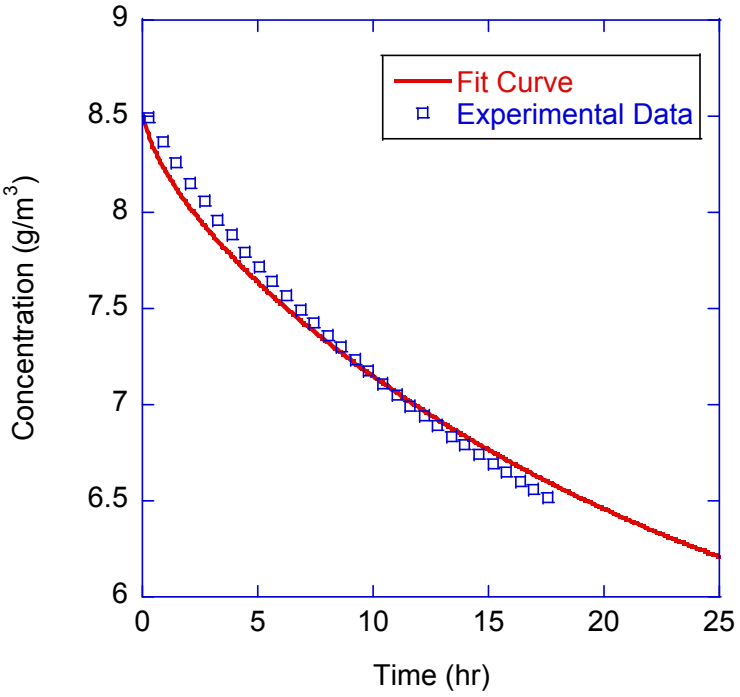

Figure 36: Fitting for diffusion coefficient, 35-25% RH 0.4 w/c 3 day specimen 2

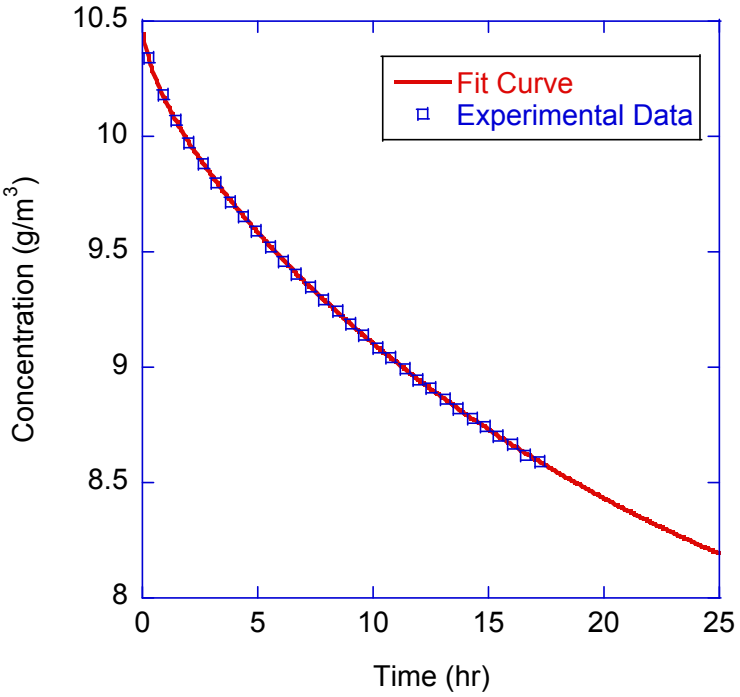

Figure 37: Fitting for diffusion coefficient, 45-35% RH 0.4 w/c 3 day specimen 2

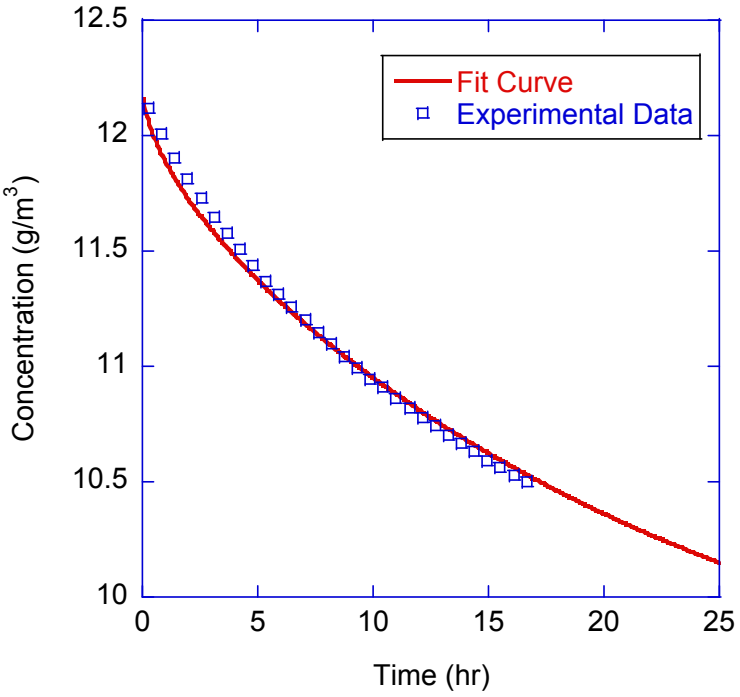

Figure 38: Fitting for diffusion coefficient, 55-45% RH 0.4 w/c 3 day specimen 2

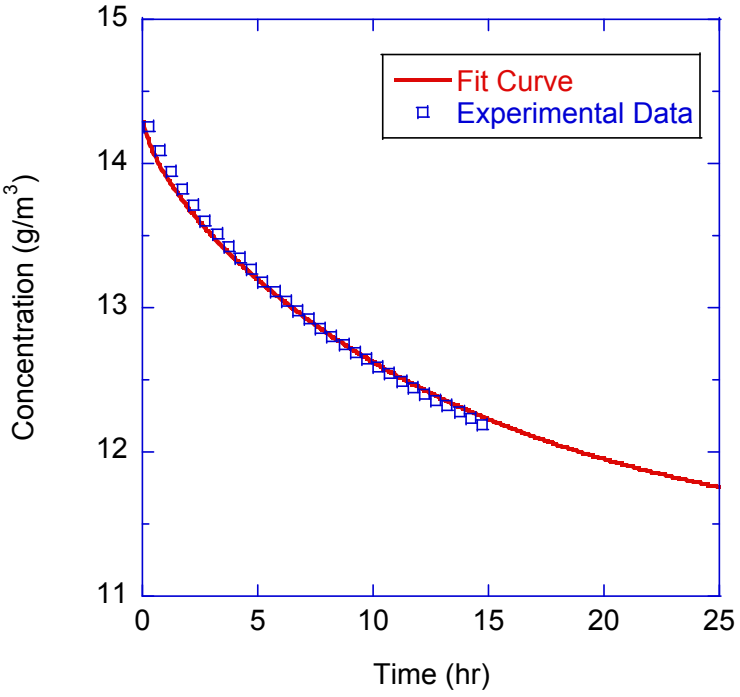

Figure 39: Fitting for diffusion coefficient, 65-55% RH 0.4 w/c 3 day specimen 2

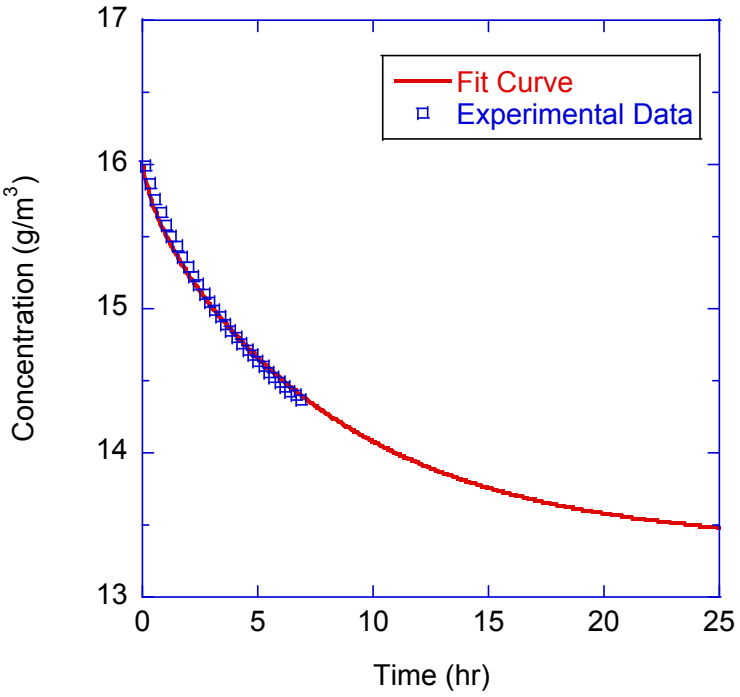

Figure 40: Fitting for diffusion coefficient, 75-65% RH 0.4 w/c 3 day specimen 2

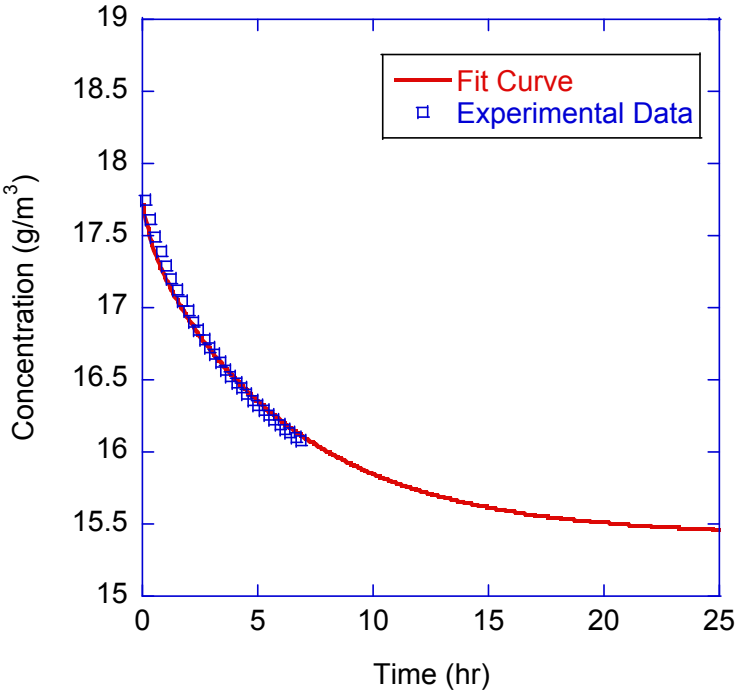

Figure 41: Fitting for diffusion coefficient, 85-75% RH 0.4 w/c 3 day specimen 2

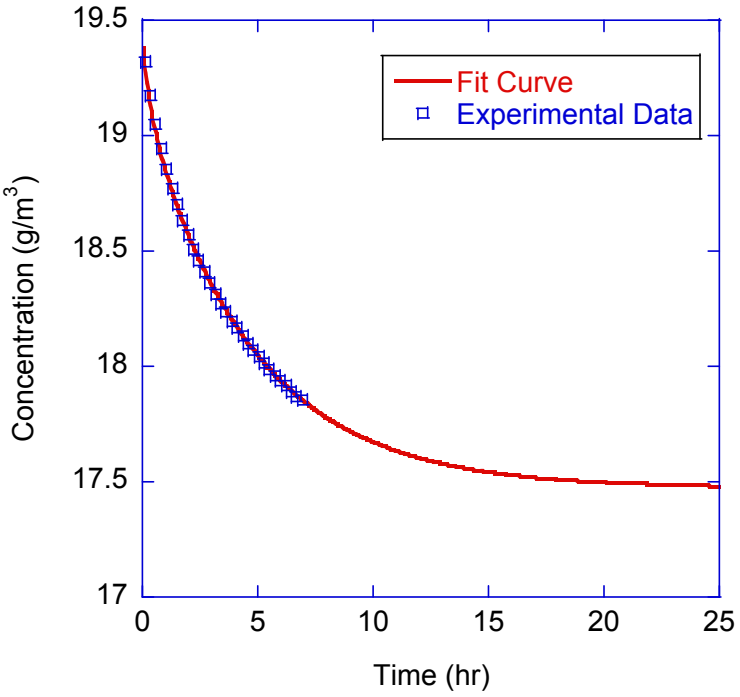

Figure 42: Fitting for diffusion coefficient, 95-85% RH 0.4 w/c 3 day specimen 2

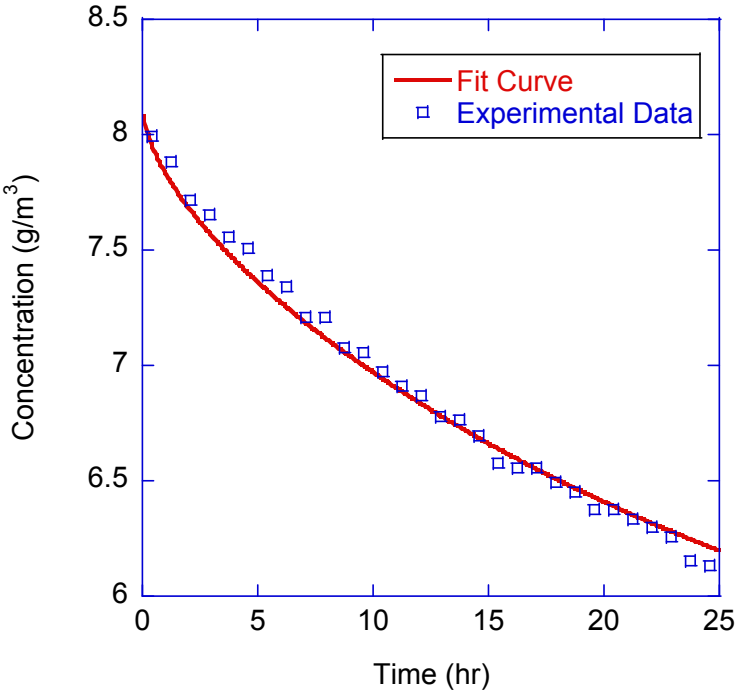

Figure 43: Fitting for diffusion coefficient, 35-25% RH 0.4 w/c 7 day specimen 1

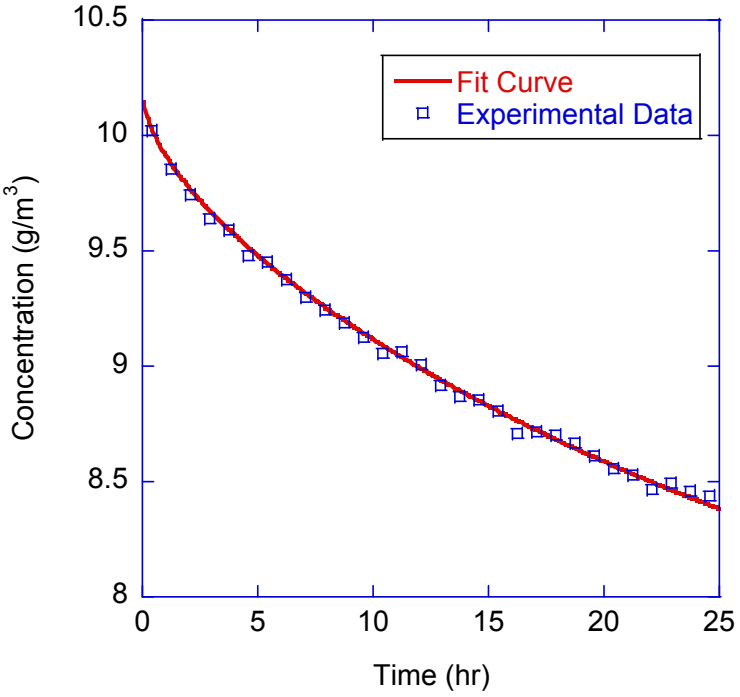

Figure 44: Fitting for diffusion coefficient, 45-35% RH 0.4 w/c 7 day specimen 1

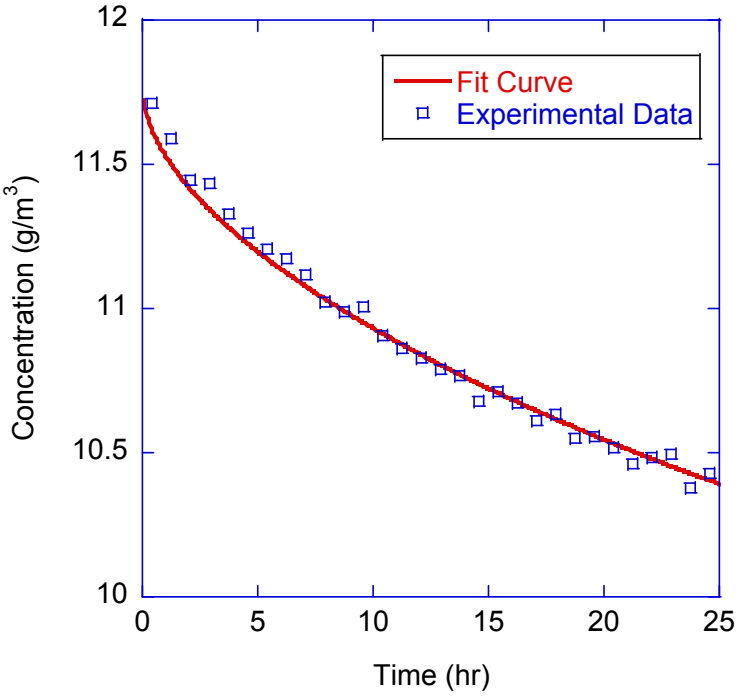

Figure 45: Fitting for diffusion coefficient, 55-45% RH 0.4 w/c 7 day specimen 1

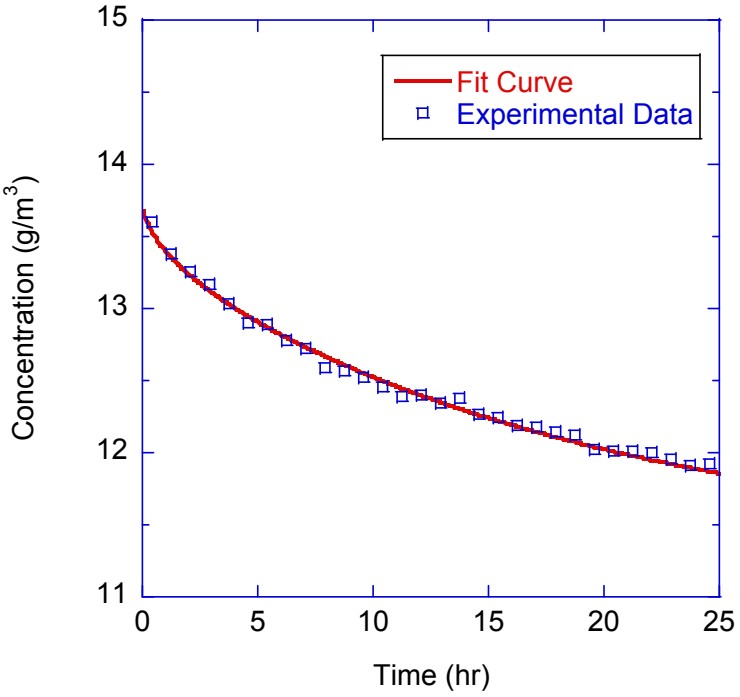

Figure 46: Fitting for diffusion coefficient, 65-55% RH 0.4 w/c 7 day specimen 1

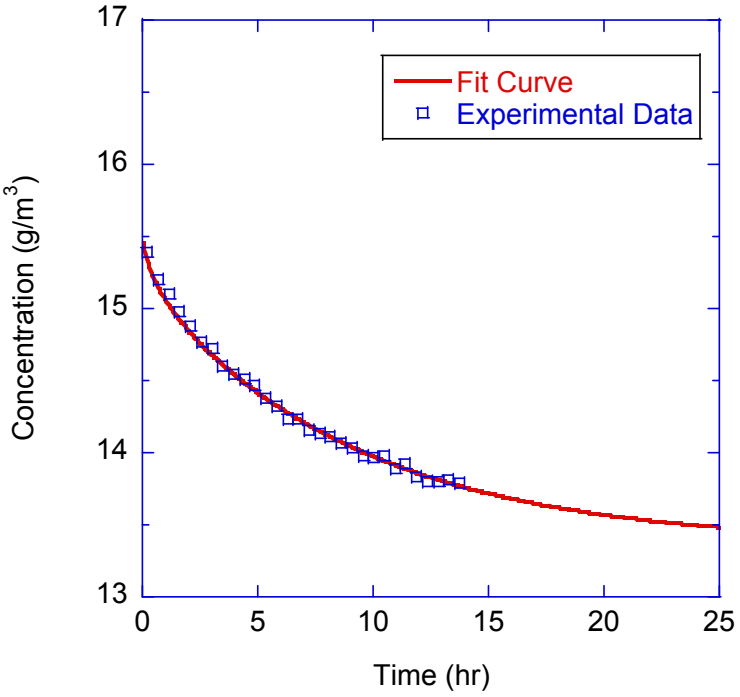

Figure 47: Fitting for diffusion coefficient, 75-65% RH 0.4 w/c 7 day specimen 1

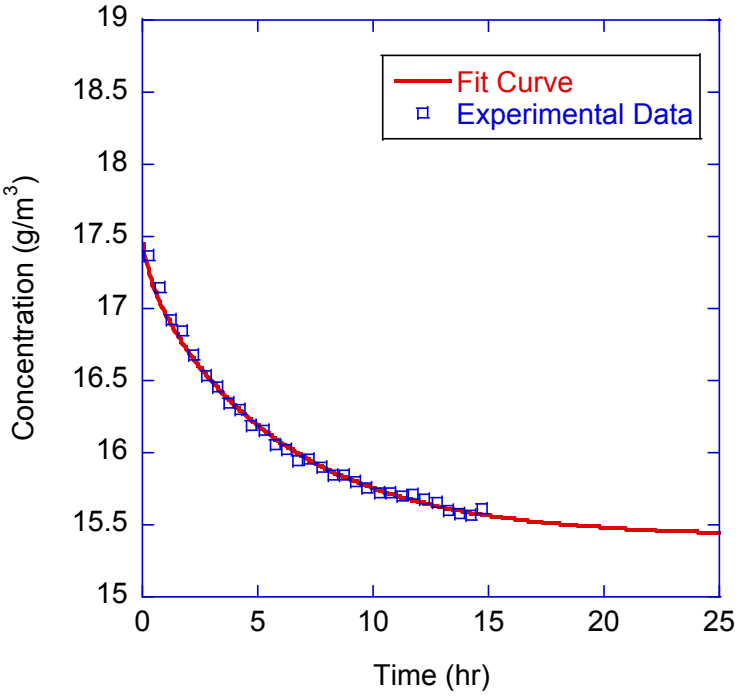

Figure 48: Fitting for diffusion coefficient, 85-75% RH 0.4 w/c 7 day specimen 1

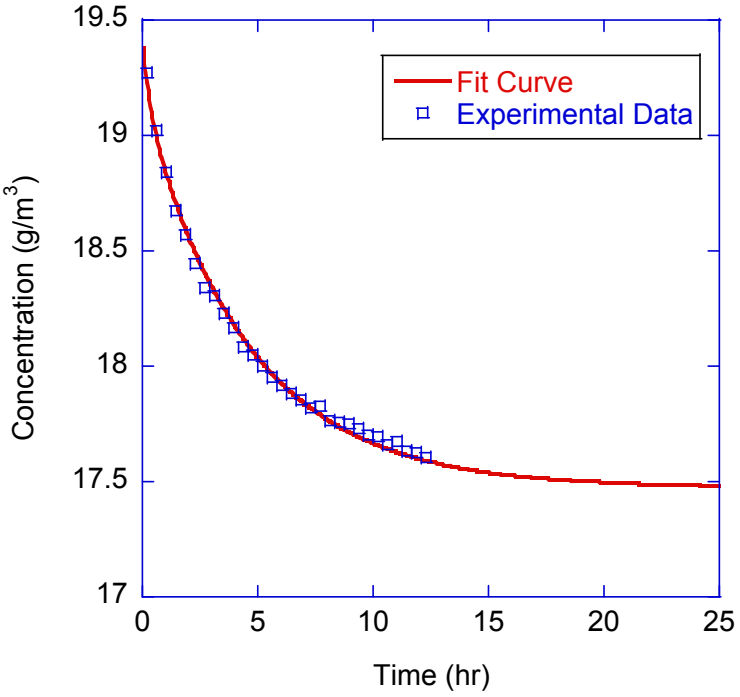

Figure 49: Fitting for diffusion coefficient, 95-85% RH 0.4 w/c 7 day specimen 1

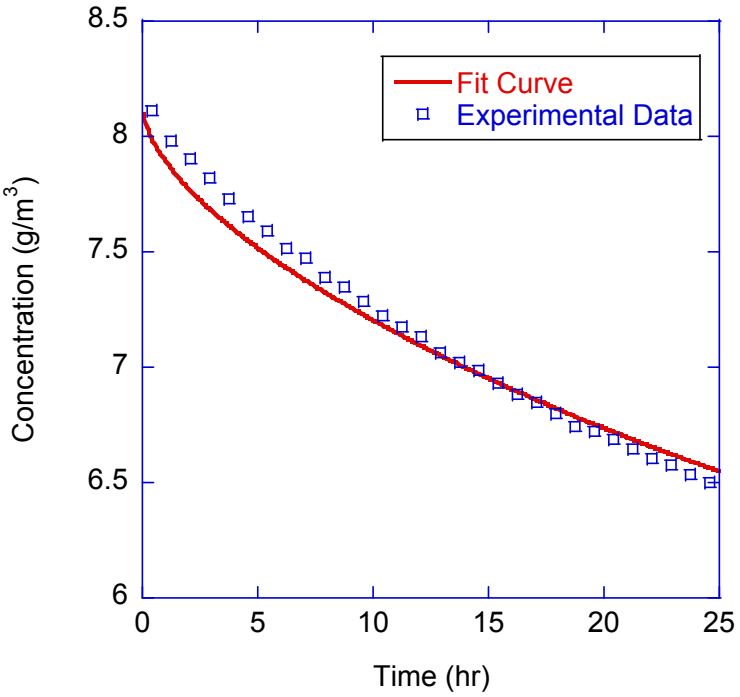

Figure 50: Fitting for diffusion coefficient, 35-25% RH 0.4 w/c 7 day specimen 2

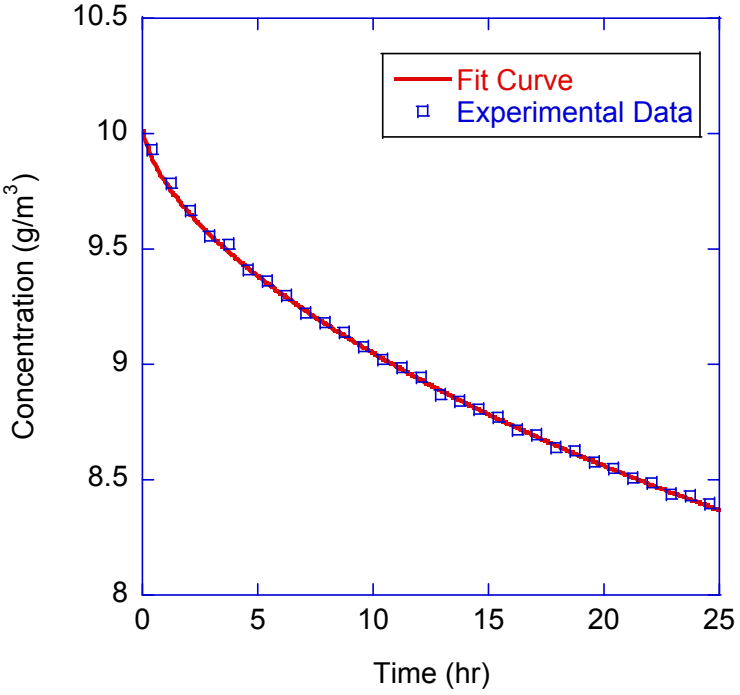

Figure 51: Fitting for diffusion coefficient, 45-35% RH 0.4 w/c 7 day specimen 2

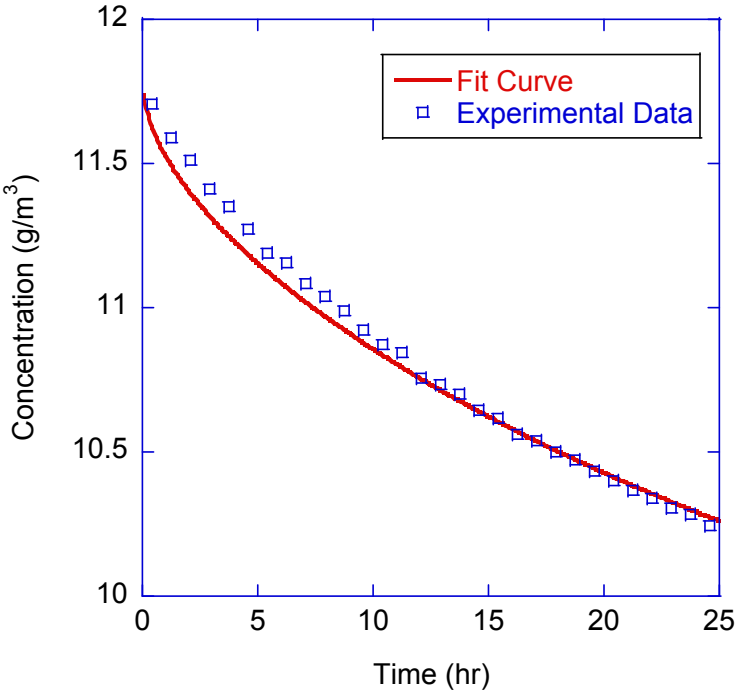

Figure 52: Fitting for diffusion coefficient, 55-45% RH 0.4 w/c 7 day specimen 2

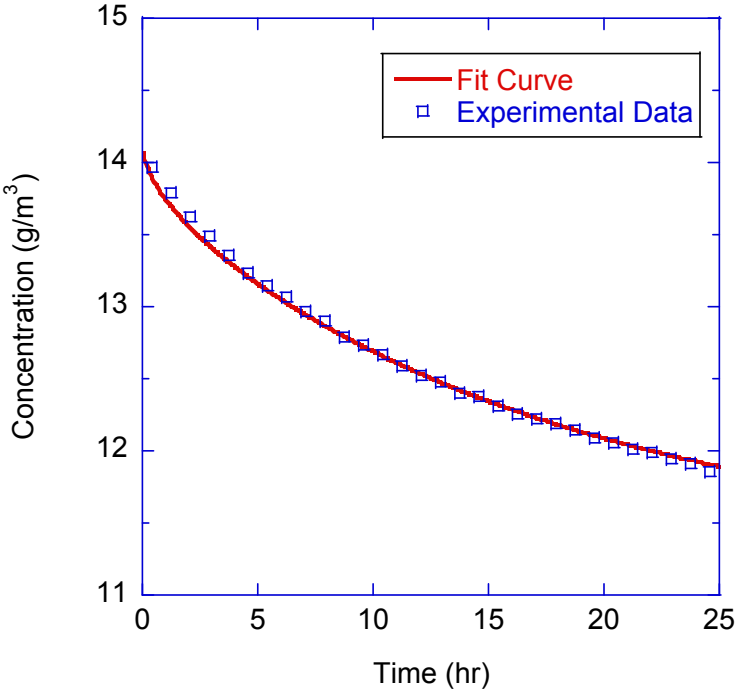

Figure 53: Fitting for diffusion coefficient, 65-55% RH 0.4 w/c 7 day specimen 2

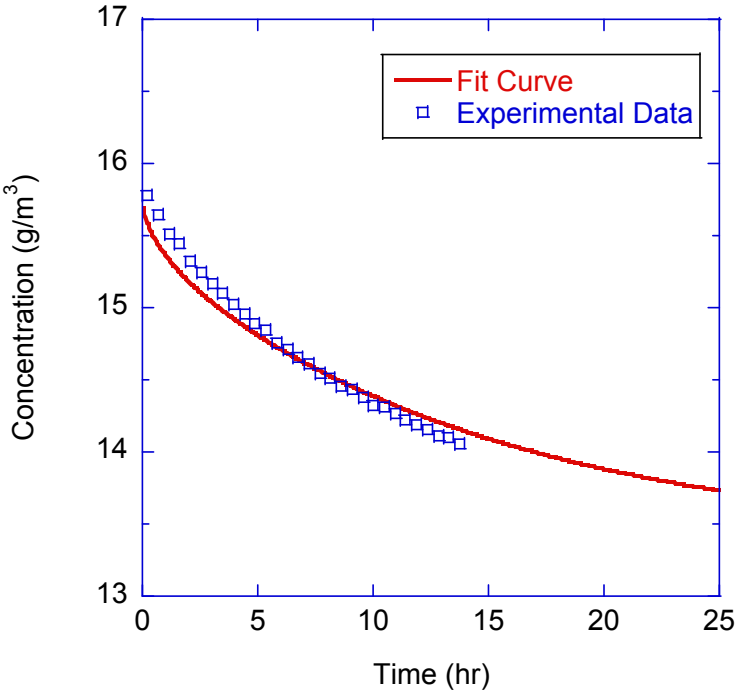

Figure 54: Fitting for diffusion coefficient, 75-65% RH 0.4 w/c 7 day specimen 2

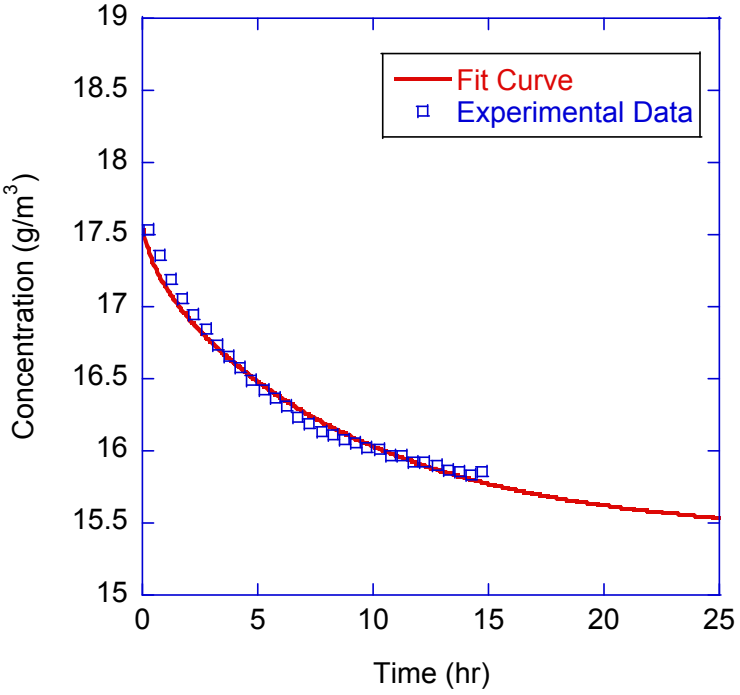

Figure 55: Fitting for diffusion coefficient, 85-75% RH 0.4 w/c 7 day specimen 2

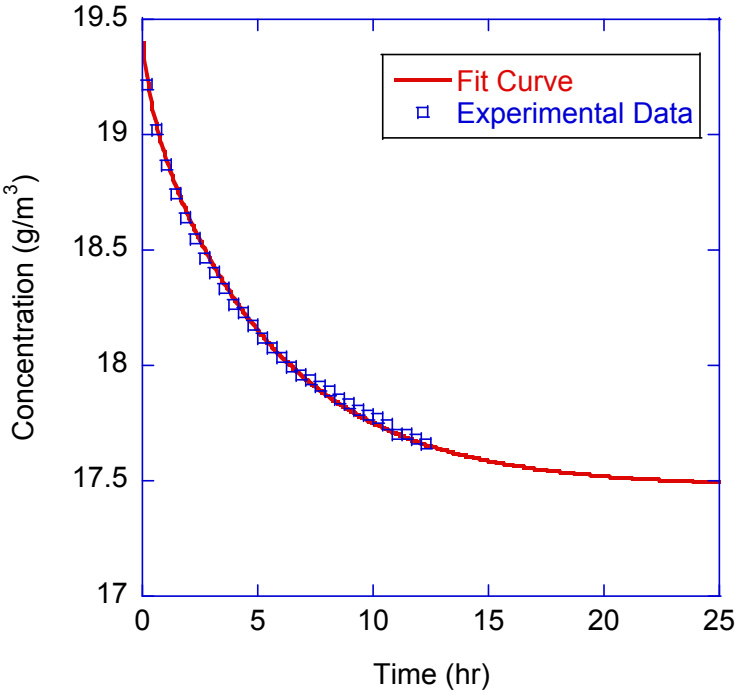

Figure 56: Fitting for diffusion coefficient, 95-85% RH 0.4 w/c 7 day specimen 2

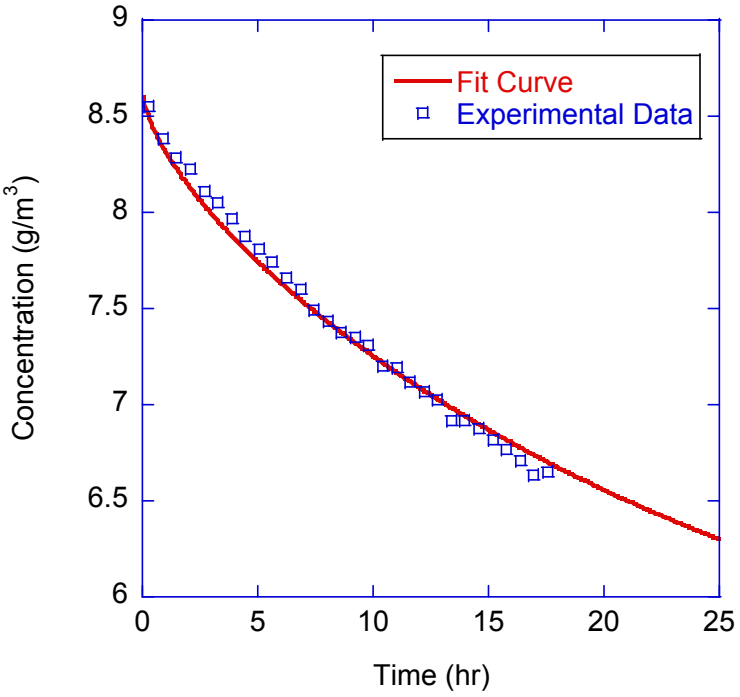

Figure 57: Fitting for diffusion coefficient, 35-25% RH 0.5 w/c 3 day specimen 1

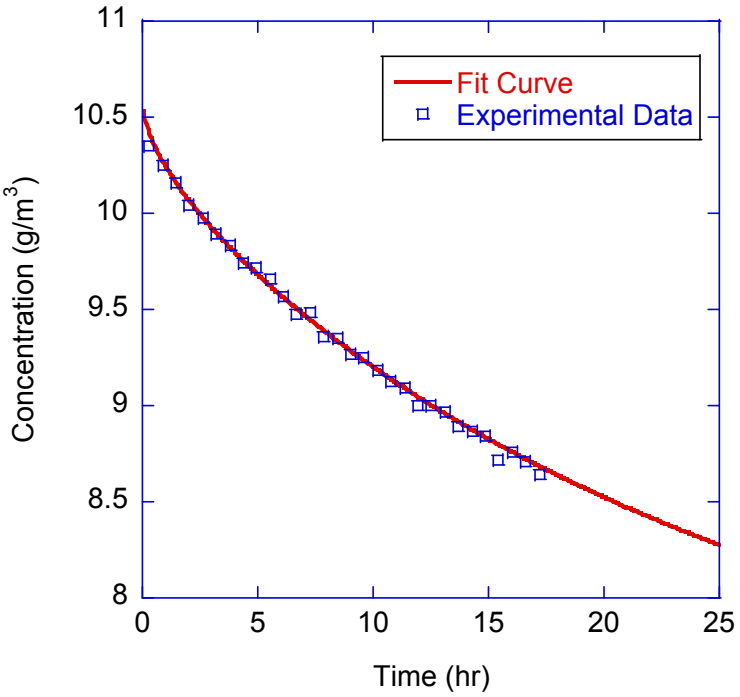

Figure 58: Fitting for diffusion coefficient, 45-35% RH 0.5 w/c 3 day specimen 1

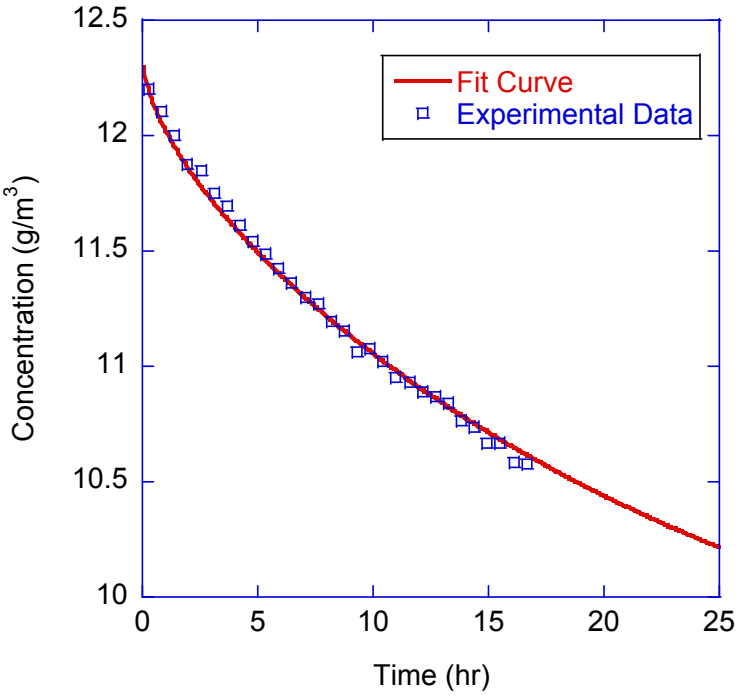

Figure 59: Fitting for diffusion coefficient, 55-45% RH 0.5 w/c 3 day specimen 1

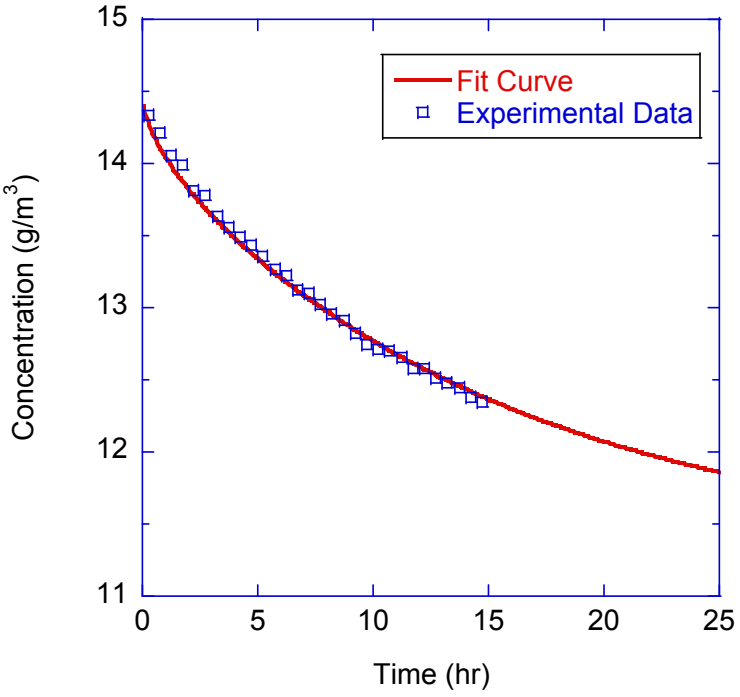

Figure 60: Fitting for diffusion coefficient, 65-55% RH 0.5 w/c 3 day specimen 1

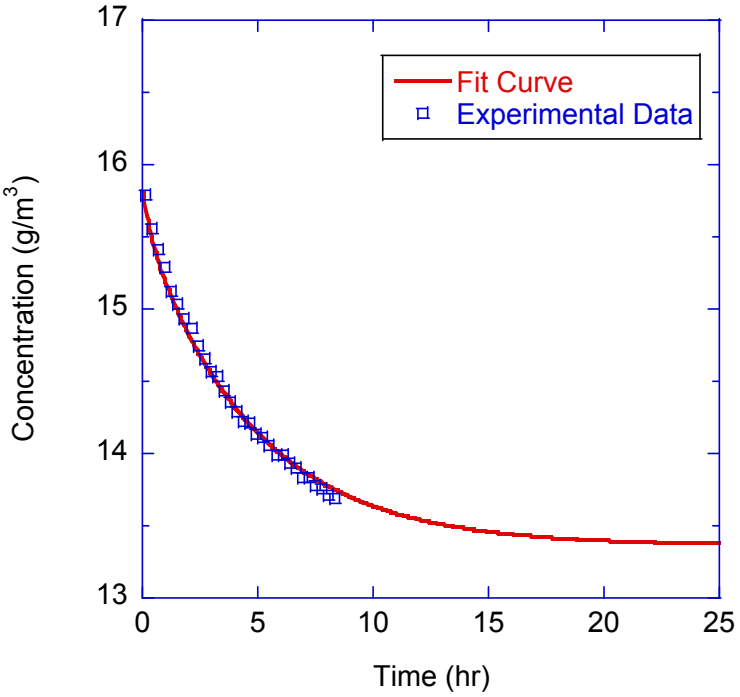

Figure 61: Fitting for diffusion coefficient, 75-65% RH 0.5 w/c 3 day specimen 1

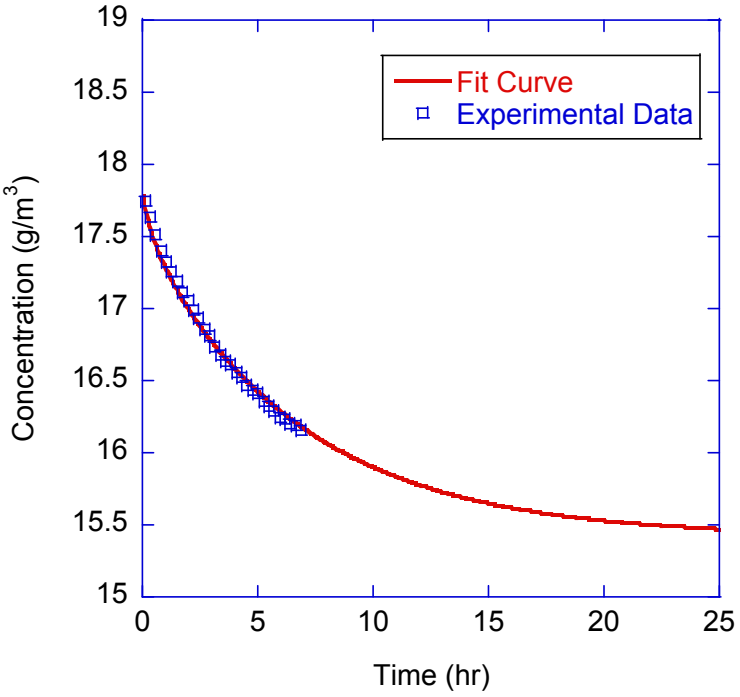

Figure 62: Fitting for diffusion coefficient, 85-75% RH 0.5 w/c 3 day specimen 1

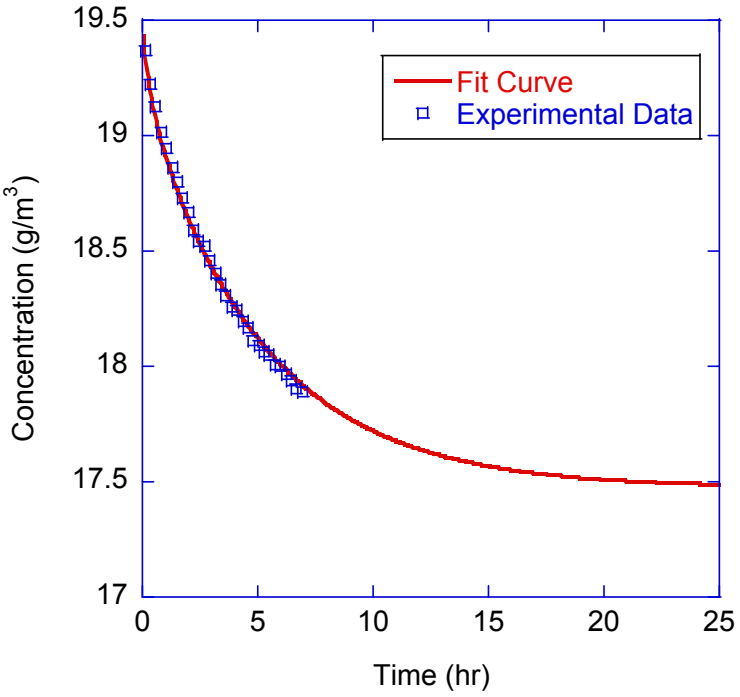

Figure 63: Fitting for diffusion coefficient, 95-85% RH 0.5 w/c 3 day specimen 1

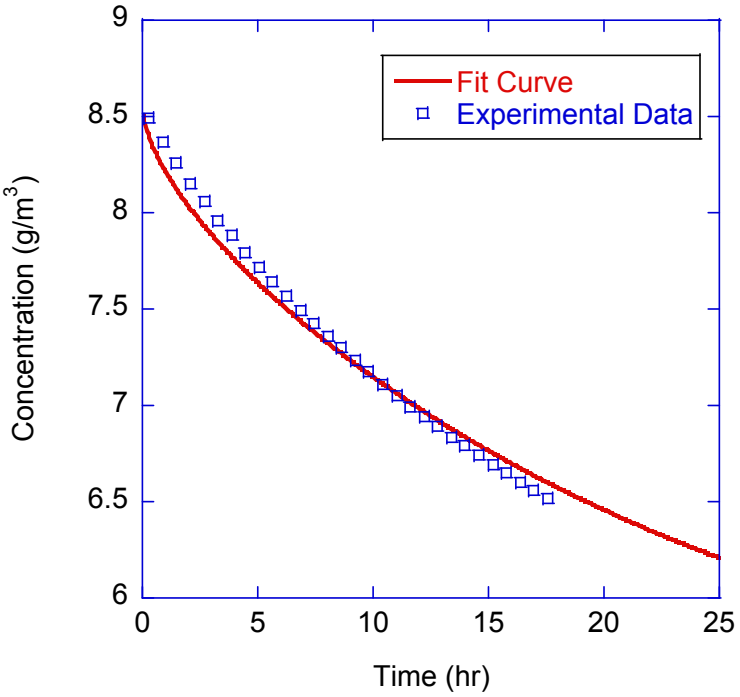

Figure 64: Fitting for diffusion coefficient, 35-25% RH 0.5 w/c 3 day specimen 2

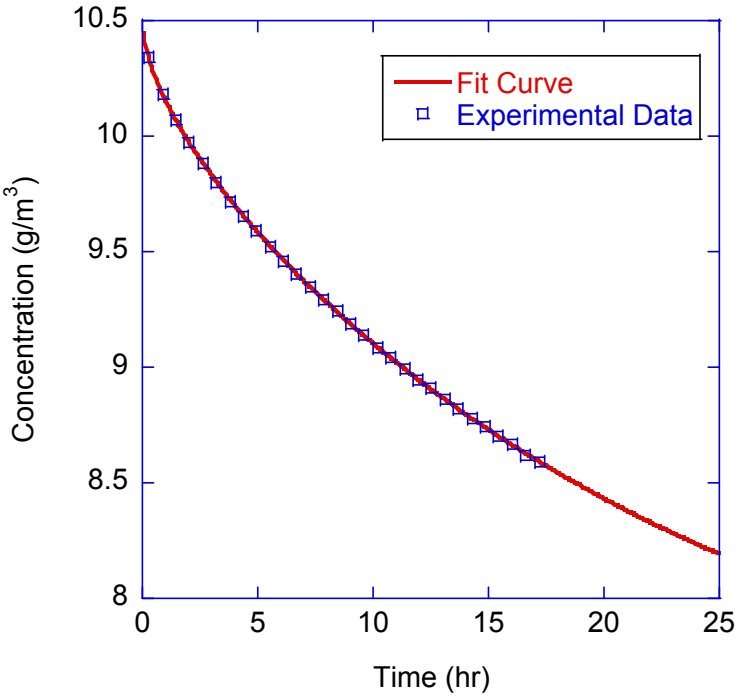

Figure 65: Fitting for diffusion coefficient, 45-35% RH 0.5 w/c 3 day specimen 2

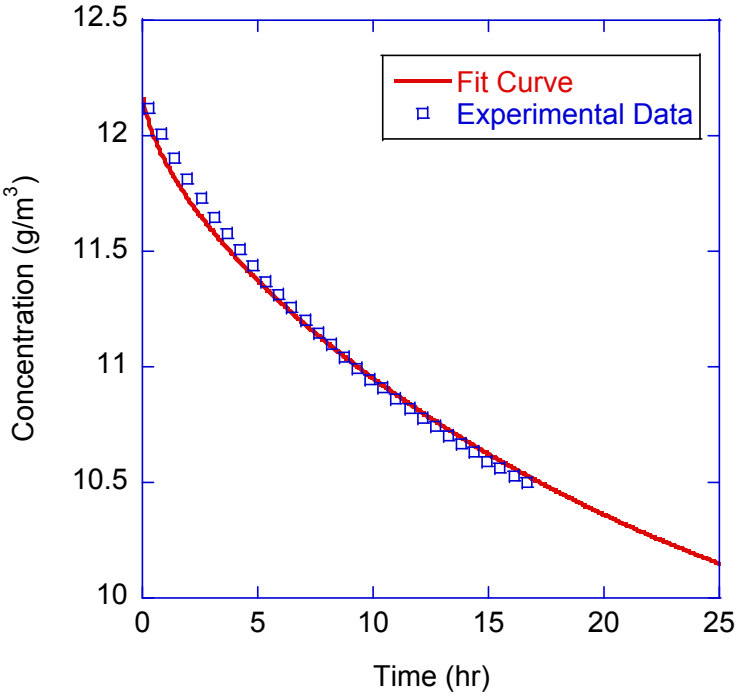

Figure 66: Fitting for diffusion coefficient, 55-45% RH 0.5 w/c 3 day specimen 2

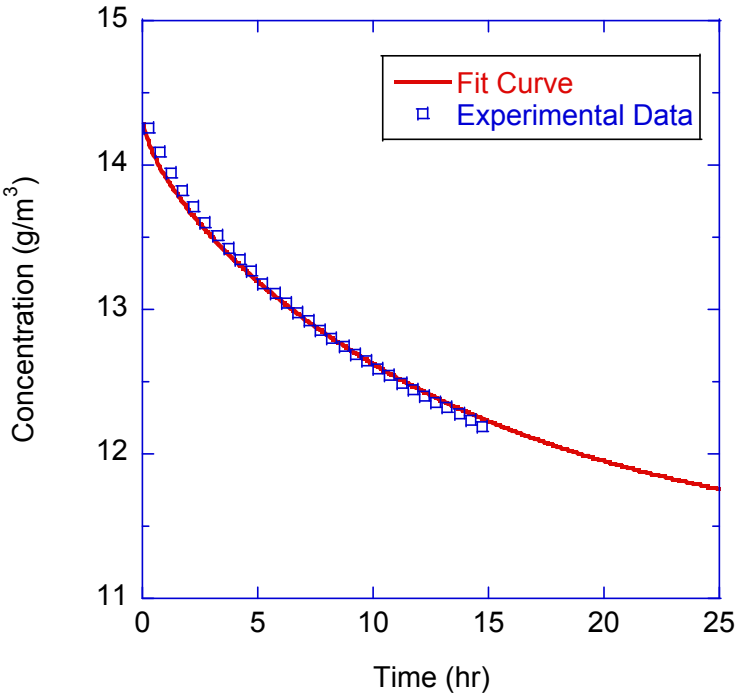

Figure 67: Fitting for diffusion coefficient, 65-55% RH 0.5 w/c 3 day specimen 2

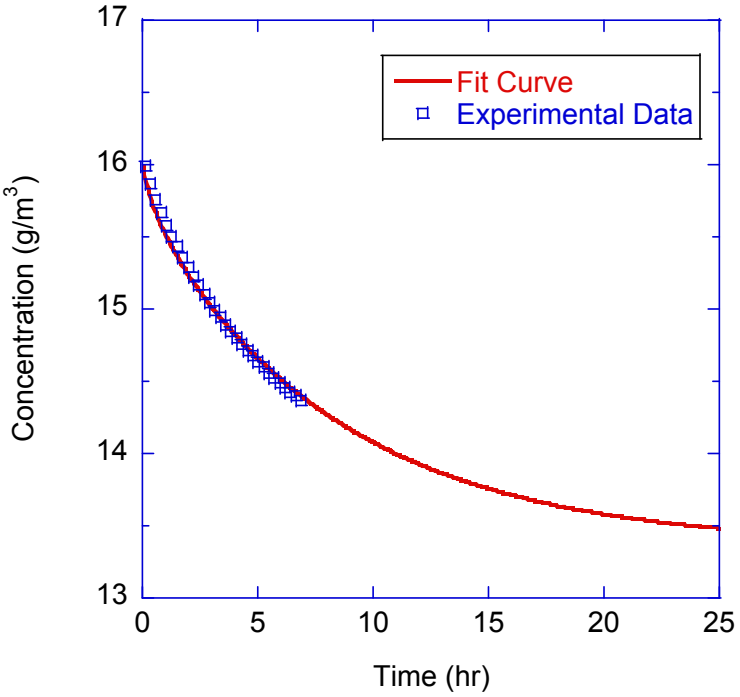

Figure 68: Fitting for diffusion coefficient, 75-65% RH 0.5 w/c 3 day specimen 2

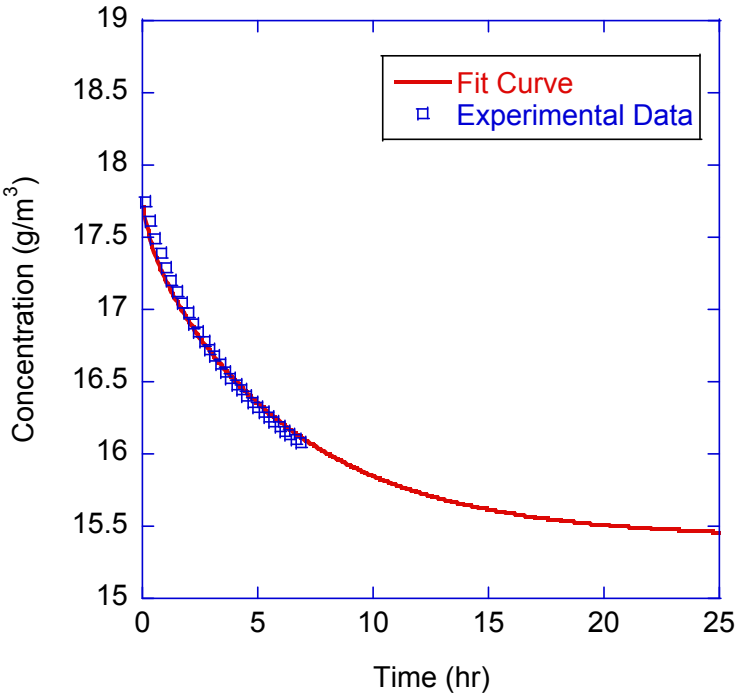

Figure 69: Fitting for diffusion coefficient, 85-75% RH 0.5 w/c 3 day specimen 2

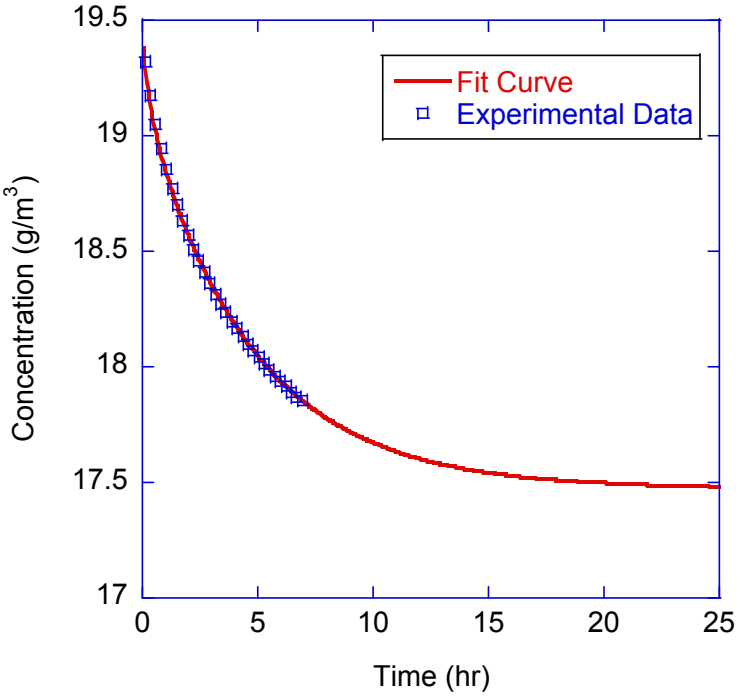

Figure 70: Fitting for diffusion coefficient, 95-85% RH 0.5 w/c 3 day specimen 2

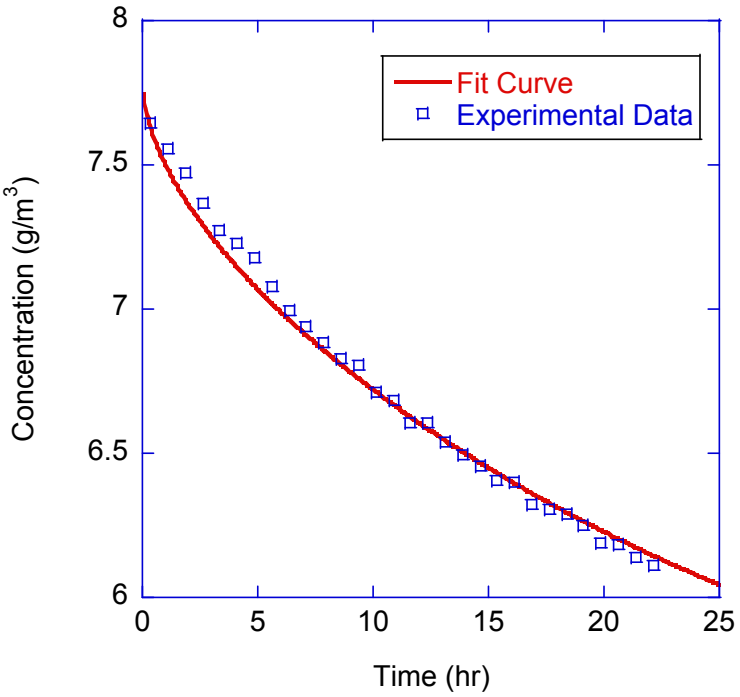

Figure 71: Fitting for diffusion coefficient, 35-25% RH 0.5 w/c 7 day specimen 1

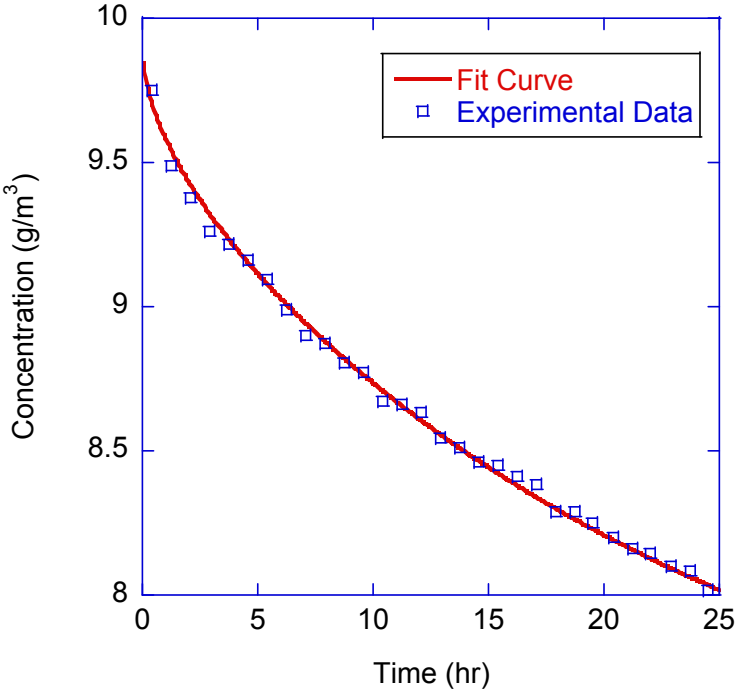

Figure 72: Fitting for diffusion coefficient, 45-35% RH 0.5 w/c 7 day specimen 1

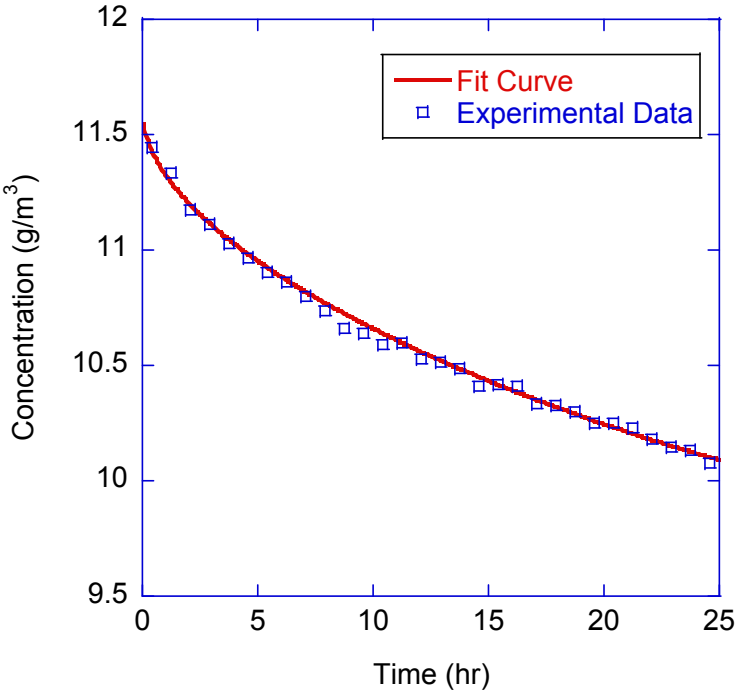

Figure 73: Fitting for diffusion coefficient, 55-45% RH 0.5 w/c 7 day specimen 1

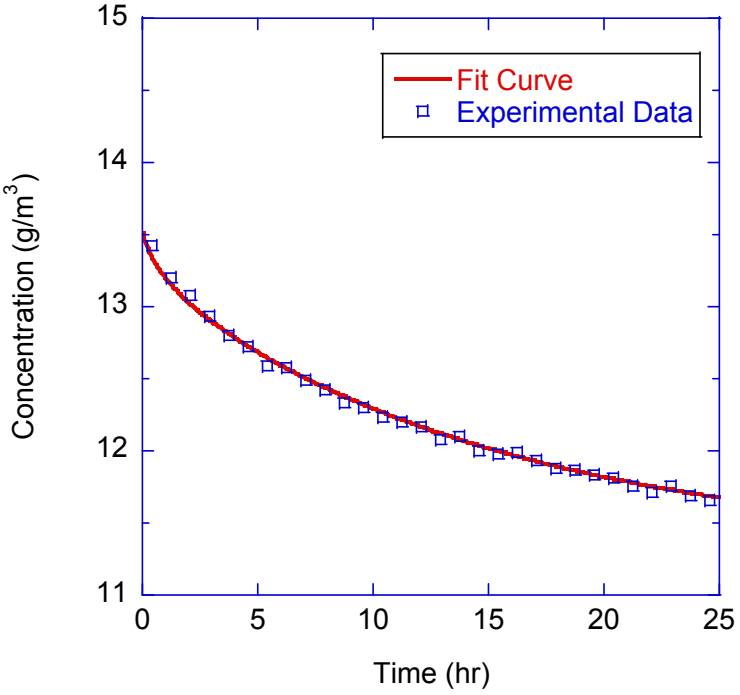

Figure 74: Fitting for diffusion coefficient, 65-55% RH 0.5 w/c 7 day specimen 1

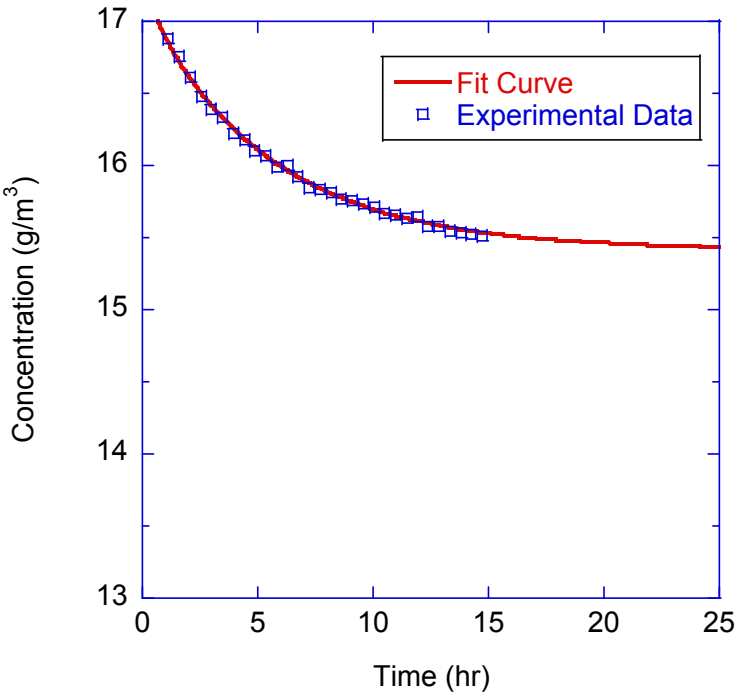

Figure 75: Fitting for diffusion coefficient, 75-65% RH 0.5 w/c 7 day specimen 1

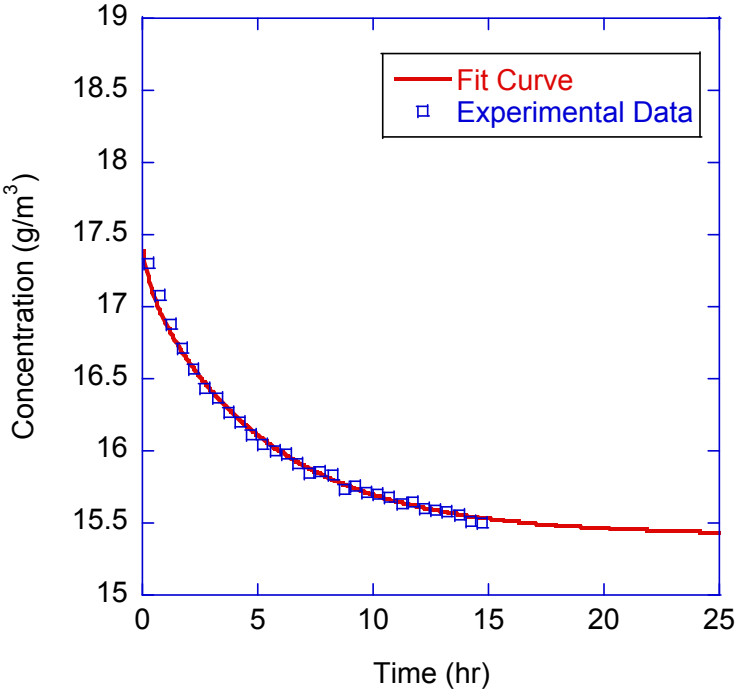

Figure 76: Fitting for diffusion coefficient, 85-75% RH 0.5 w/c 7 day specimen 1

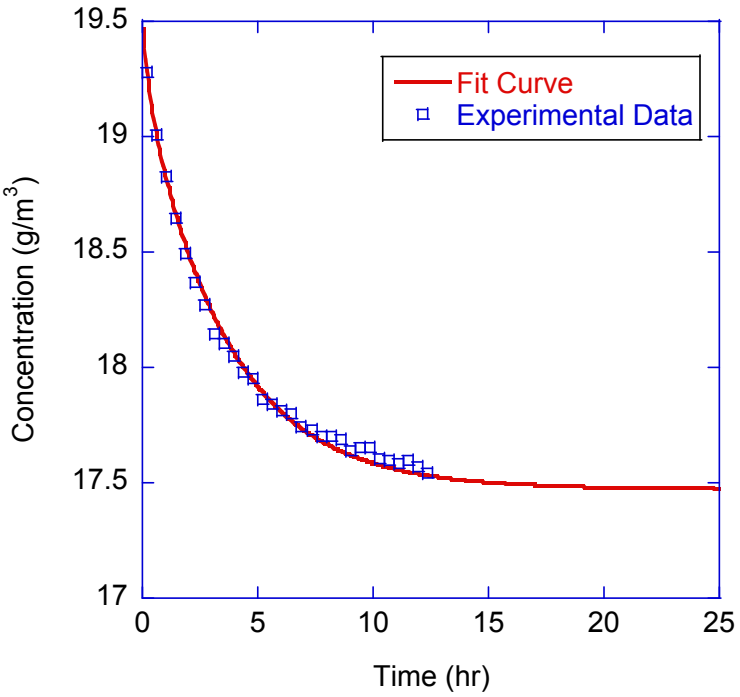

Figure 77: Fitting for diffusion coefficient, 95-85% RH 0.5 w/c 7 day specimen 1

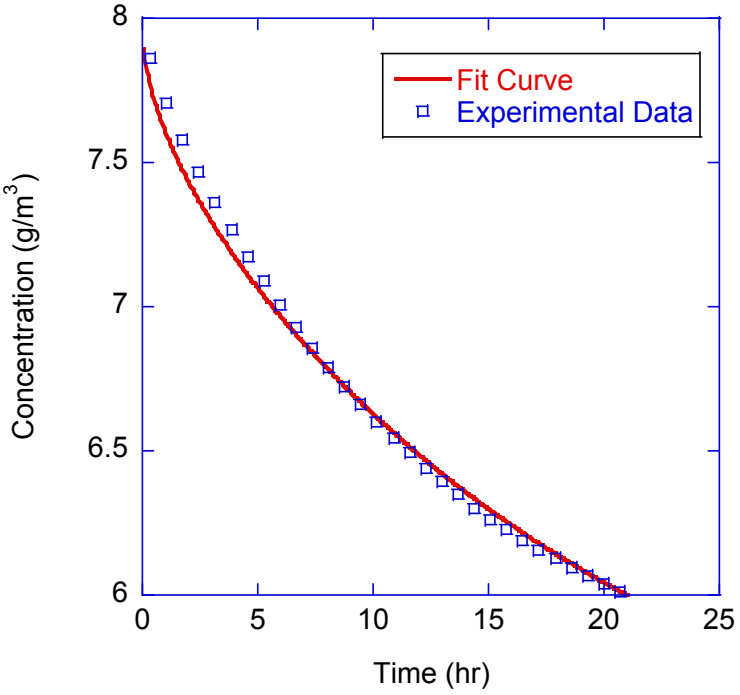

Figure 78: Fitting for diffusion coefficient, 35-25% RH 0.5 w/c 7 day specimen 2

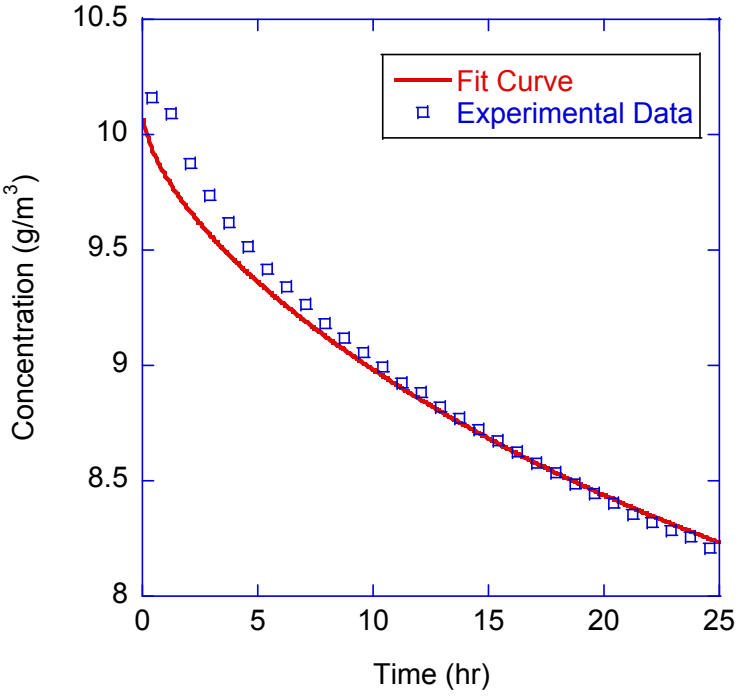

Figure 79: Fitting for diffusion coefficient, 45-35% RH 0.5 w/c 7 day specimen 2

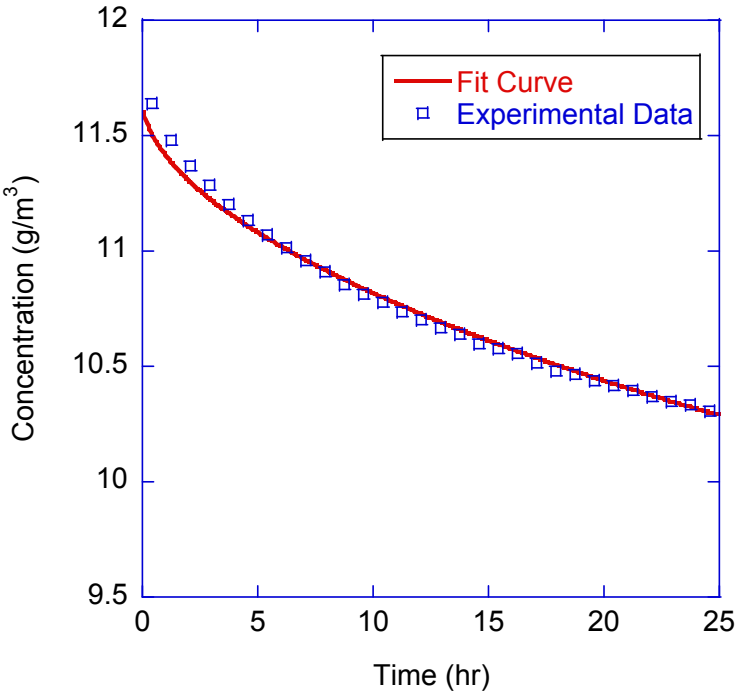

Figure 80: Fitting for diffusion coefficient, 55-45% RH 0.5 w/c 7 day specimen 2

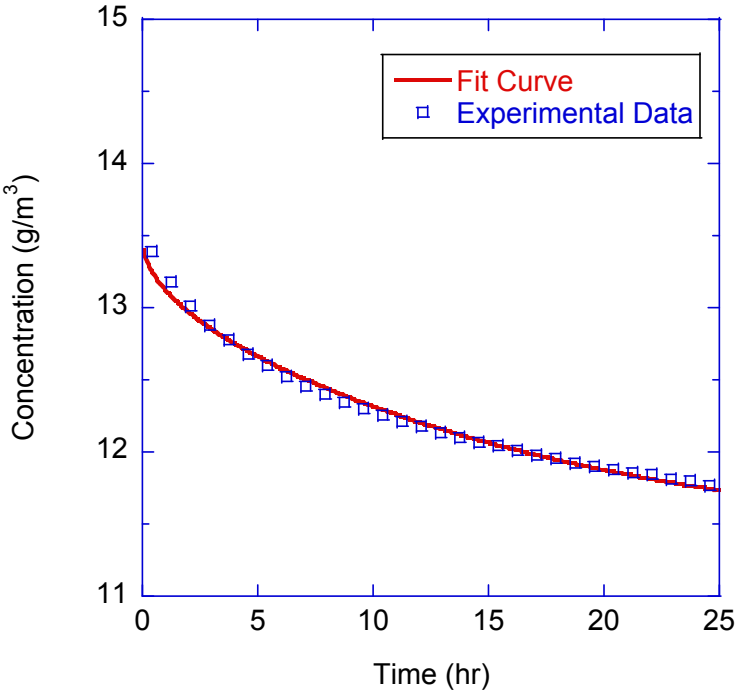

Figure 81: Fitting for diffusion coefficient, 65-55% RH 0.5 w/c 7 day specimen 2

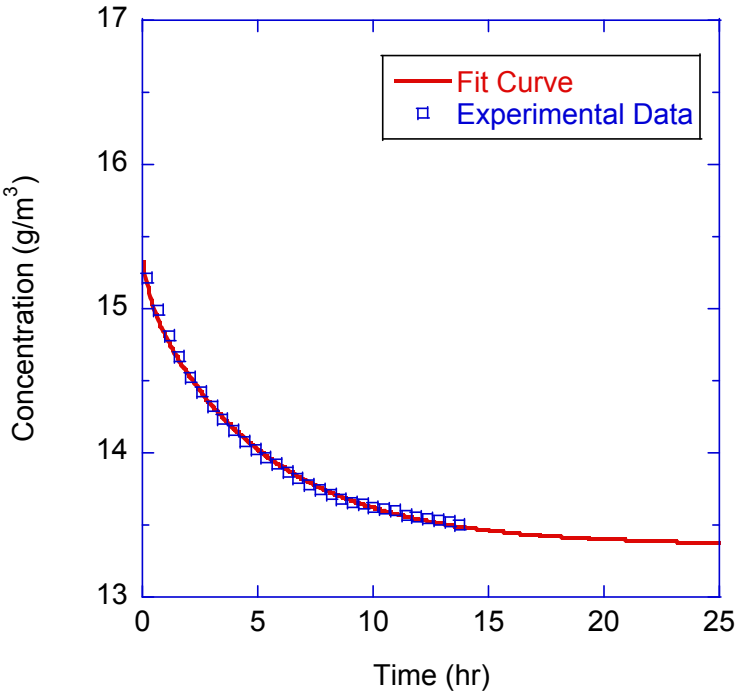

Figure 82: Fitting for diffusion coefficient, 75-65% RH 0.5 w/c 7 day specimen 2

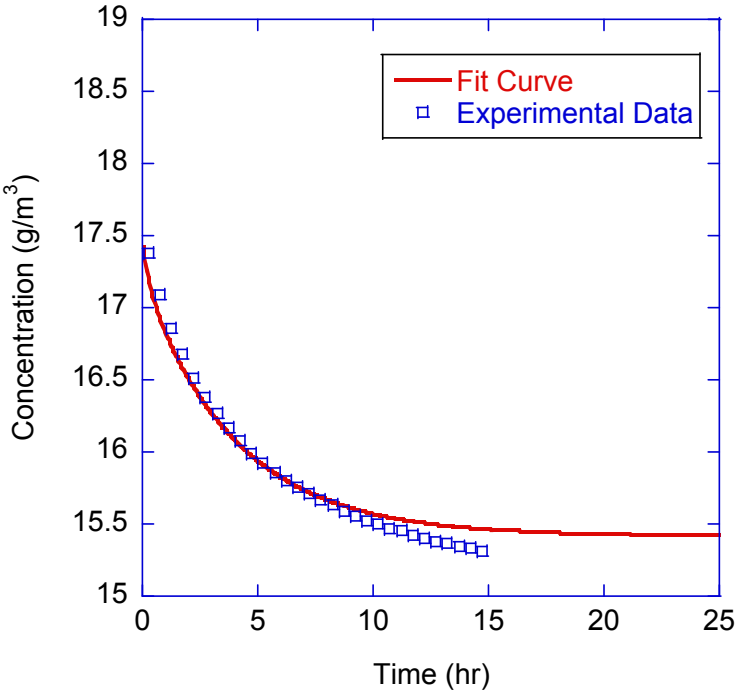

Figure 83: Fitting for diffusion coefficient, 85-75% RH 0.5 w/c 7 day specimen 2

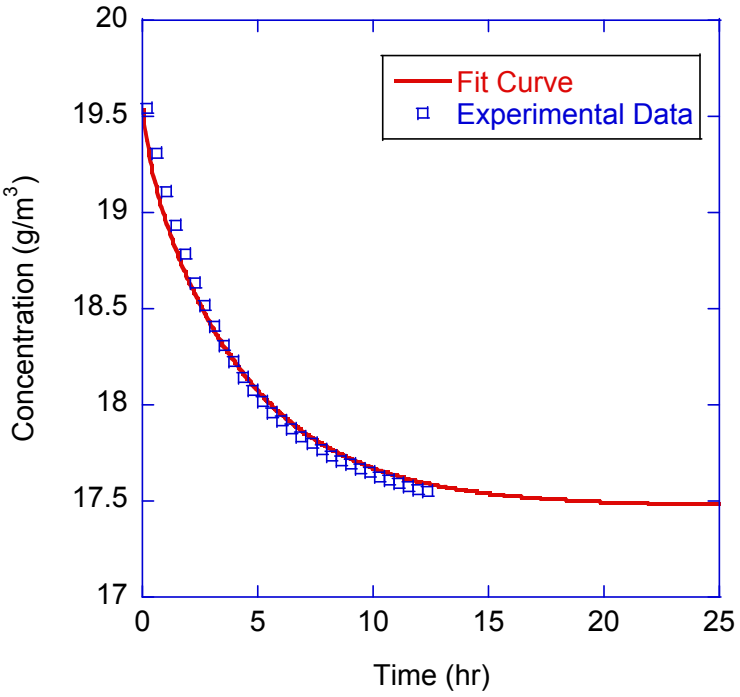

Figure 84: Fitting for diffusion coefficient, 95-85% RH 0.5 w/c 7 day specimen 2

APPENDIX B

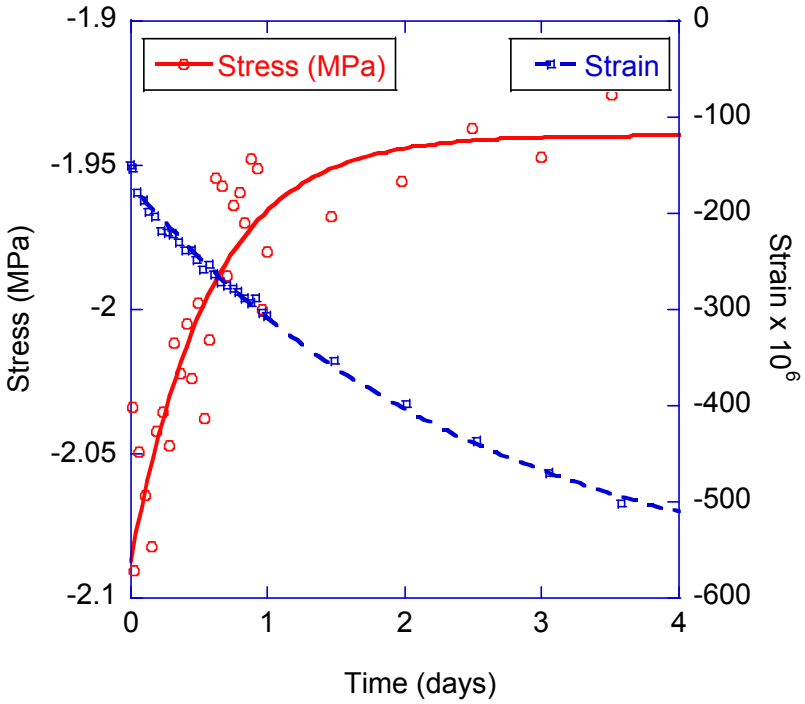

Figure 85: Creep test data for 0.4 w/c 3 day specimen

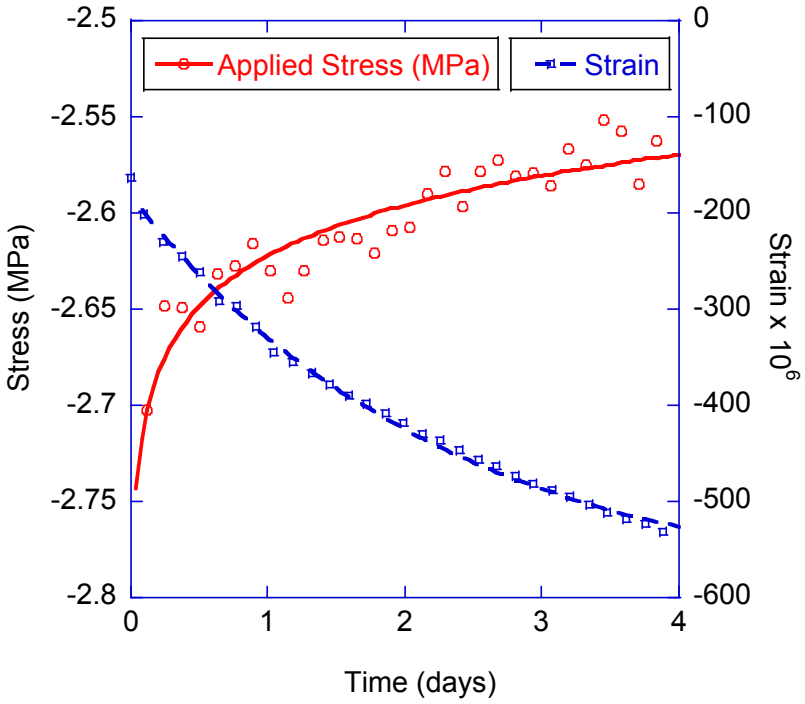

Figure 86: Creep test data for 0.4 w/c 7 day specimen

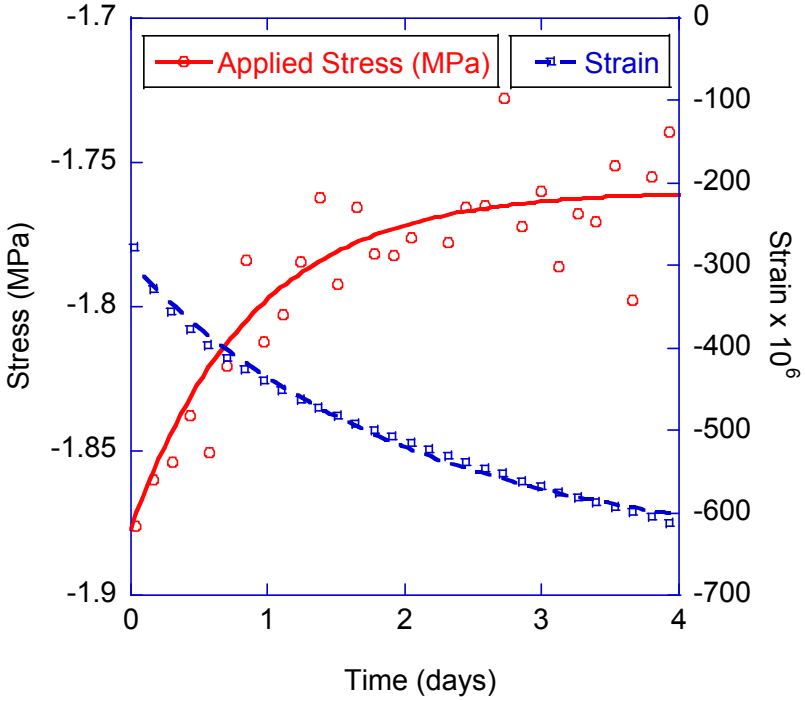

Figure 87: Creep test data for 0.5 w/c 3 day specimen

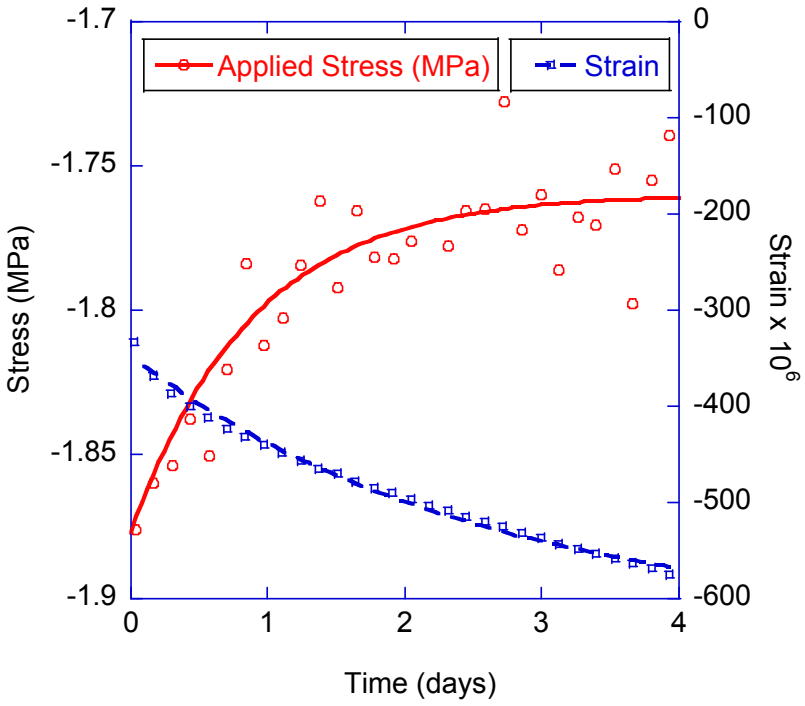

Figure 88: Creep test data for 0.5 w/c 7 day specimen

VITA

Chin Kong Leung received his Bachelor of Science degree in civil engineering from California State University, Chico in 2007. During his pursuit of his bachelor's degree he studied as an exchange student for five months at the Hamburg University of Technology. He entered the civil engineering materials program at Texas A&M University in September 2007. His research interests include damping and moisture transport of cementitious composites. He will be pursuing a Doctorate at Texas A&M University beginning May 2009.

Mr. Leung may be reached at Department of Civil Engineering, CE/TTI 501H, 3136 TAMU, College Station, TX 77843 or by email at cleung@tamu.edu